Resolution enhancement in a scanning optical microscope using array detection

Satya Siddhartha Goutam Buddha

Ph.D. 2020

IIT Guwahati

INDIAN INSTITUTE OF TECHNOLOGY GUWAHATI

DOCTORAL THESIS

Resolution enhancement in a scanning optical microscope using array detection

Satya Siddhartha Goutam Buddha

Roll No: 146121020

Thesis submitted in partial fulfilment of the requirements for the degree of Doctor of Philosophy of the Indian Institute of Technology Guwahati.

Supervisor: Prof. Bosanta R. Boruah

Optical Imaging Lab
Department of Physics
Indian Institute of Technology Guwahati
Guwahati (Assam), India, Pin- 781039

September 2020

Dedicated to my family

Declaration

Satya Siddhartha Goutam Buddha
Roll No: 146121020
Optical Imaging Lab
Department of Physics
Indian Institute of Technology Guwahati
Guwahati (Assam), India, Pin- 781039
Email: satya.buddha@iitg.ac.in

I hereby declare that the results embodied in this thesis is the result of theory and experiment carried out by me at the Department of Physics, Indian Institute of Technology Guwahati, Guwahati, India, under the supervision of **Prof. Bosanta R. Boruah**. This thesis has not been submitted to any university/ institute or elsewhere for the award of any degree, diploma or associateship.

Satya Siddhartha Goutam Buddha
September 2020

Certificate

Prof. Bosanta R. Boruah
Department of Physics
Indian Institute of Technology Guwahati
Guwahati (Assam), India, Pin- 781039
Email: brboruah@iitg.ac.in

This is to certify that the work contained in the thesis entitled **'Resolution enhancement in a scanning optical microscope using array detection'** by **Satya Siddhartha Goutam Buddha** (Roll No. 146121020), a student of Department of Physics, Indian Institute of Technology Guwahati, for the award of degree of Doctor of Philosophy, has been carried out under my supervision.

The present thesis or any part thereof has not been submitted elsewhere for award of any other degree, diploma or associateship.

Prof. Bosanta R. Boruah
September 2020

Acknowledgements

Foremost, I would like to express my sincere gratitude to my supervisor Prof. Bosanta Ranjan Boruah for provided me with insightful comments, meticulous guidance, constructive criticism, and ceaseless help throughout the entire period of my Ph.D. work. His constant guidance and exemplar advice made me work hard even after several failures while performing experiments.

I express my thanks to my doctoral committee members: Prof. Parvat K Giri, Dr. Gagan Kumar, and Dr. A. S. Achalkumar for reviewing my research progress every year and sharing their invaluable comments, suggestions, and feedback which helped me to improve my research work.

I convey my warm gratitude to the former and present HoDs of Physics, Prof. Saurabh Basu, Prof. Poulose Poulose, and Prof. Subhradip Ghosh for providing me the opportunity to utilize different resources of the department. I would also like to thank all the staff members of the department for their support and cooperation during official paperwork.

A warm and sincere thanks to our collaborator Prof. Paul French for giving me the opportunity to work and learn the super-resolution microscopy technique (STORM) at the Imperial College of London. I would also like to thank Dr. Frederik Gorlitz and Dr. Edwin Gracia for the help and support to implement the super-resolution microscopy setup in our laboratory. I also thank Dr. Bithiah Grace Jaganathan for the preparation of the biological samples in her laboratory in IIT Guwahati.

I would also like to thank all my fellow research mates, Dr. Md. Gaffar, Dr. Biswajit Pathak, Dr. Santanu Konwar, Dr. Ranjan Kalita, Nagendra Kumar, Karuna S. Malik, Akanshu Chauhan, Nedup Sherpa and Anupam Bharadwaj for the doubt clearing sessions, help during experiments and quality time (including the year-end picnic) that we had spent together.

A special thanks go to the SPIE IITG student chapter members for kept me involved in organizing various events in various schools and colleges. It helps me to develop event organizing skills, teamwork spirit and leadership quality along with my research career.

I also take this opportunity to sincerely acknowledge the financial support from the Ministry of Human Resource and Development (MHRD), Government of India.

I am indebted to all my friends especially the 2014 batch, juniors, and seniors at IIT Guwahati who made a comfortable stay in the campus and who were always so helpful in numerous ways. Special thanks to all the Odia friends in the campus who did not make me feel that I was far from home. I am grateful to the Art of Living and the Hare Krishna Movement for teaching me meditation and providing spiritual knowledge which helped me to maintain a healthy life and kept me free from all stressful situations. I would also like to thank my school friends, BSc friends, and MSc friend for being with me in my ups and downs of my life.

Last but not least, I am deeply indebted to my deceased father and grandfather for their great role in my life and their numerous sacrifices for me. I would like to owe my deepest gratitude to my family members and our relatives: my grandmother, my mother, and my elder sisters: Nani, Didi, Dei, Subha Nani, Iti Nani, and Mantu Bhai for their prayer for my happiness, success, and good health. Their patience and sacrifice will remain my inspiration throughout my life. Whatever I achieved today is only because of their constant support, love, affections, and faith. They always supported me in pursuing my dream.

Abstract

An optical microscope is an imaging tool that provides images of a specimen with finer details relative to the image provided by an unaided eye. Owing to the far field imaging capability the optical microscopes have become very important in diverse application areas. They are in particular useful for imaging of living biological samples which is not possible with other high resolution microscopes such as an electron microscope. Based on the illumination mechanism the optical microscopes are divided into two broad categories, namely, the widefield microscope and the point scanning microscope. In comparison with the widefield microscope, the point scanning microscope facilitates the use of laser as the illumination beam and implementation of various user defined beam profiles. The amount of finer details in the image that can be provided by an optical microscope is decided by the parameter called resolution, which has an upper limit due to the diffraction phenomenon. A point scanning microscope with a pinhole placed in front of the detector and positioned conjugate to the illumination spot in the sample plane is known as confocal microscope. The confocal microscope provides significantly better axial resolution and marginally better lateral resolution relative to a widefield microscope. However to achieve the best resolution performance the pinhole of the microscope should be as small as possible. Unfortunately as the pinhole size decreases the amount of signal reaching the detector also decreases resulting in a drop in the signal-to-noise ratio. On the other hand the use of an array detector instead of a point detector in a scanning optical microscope enables pixel reassignment in the detector plane during image formation, in an imaging scheme called image scanning microscopy. Image scanning microscopy is shown to provide superior lateral resolution relative to a confocal microscope without compromising on the signal level. Moreover the detector array available for each scan position enables implementation of state-of-the-art imaging schemes for the enhancement of both lateral and axial resolution. However the array detection microscope requires a stable and accurate scanning mechanism and the synchronization of the same with the array detector often slows down the imaging process. In addition to the point scanning microscope, resolution beyond the diffraction limit can also be achieved in the widefield

microscope working in the fluorescence mode. The imaging system called stochastic optical reconstruction microscope (STORM) implemented in a widefield microscope can provide super-resolved images of biological samples. In this thesis we develop two types of array detection microscopes, one using galvo mirror based scanning and the other using holographic beam scanning. We configure the beam scanning mechanisms and synchronize them with the array detector in such a way that the imaging can be achieved without compromising on the other performance parameters. We employ the two array detection microscopes to implement different imaging schemes to achieve enhancement in both lateral and axial resolutions. We also develop a STORM system and combine the same with our array detection microscope so as to be able to obtain both super-resolved imaging and reflected light imaging of the same part of the specimen.

Table of contents

List of figures

List of tables

Acronyms and Abbreviation

Greek Symbols

ι	Unit imaginary number ($\sim \sqrt{-1}$)
λ	Wavelength
π	$\simeq 3.14\ldots$
σ	Standard Deviation

Other Symbols

$\mathscr{F}$	Fourier Transform
$\mathscr{F}^{-1}$	Inverse Fourier Transform

Acronyms / Abbreviations

BS	Beam Splitter
CCD	Charge-Coupled Device
CMOS	Complementary Metal Oxide Semiconductor
DBS	Dichroic Beam Splitter
PMT	Photo Multiplier Tube
AOD	Acousto-Optic Deflector
CGH	Computer Generated Holography
DBC	Dichroic Beam Combiner

DBS	Dichroic Beam Splitter
EOD	Electro-Optic Deflector
FCA	Fiber Coupler Adapter
FLCoS	Ferroelectric Liquid Crystal on Silicon
FLCSLM	Ferro-electric Liquid Crystal Spatial Light Modulator
FWHM	Full Width at Half Maximum
IDE	Integrated Development Environment
ID	Iris Diaphragm
IPE	Integrated Programming Environment
LCoS	Liquid Crystal on Silicon
LCSLM	Liquid Crystal Spatial Light Modulator
MEMS	Micro-Electro-Mechanical Systems
NA	Numerical Aperture
NLCSLM	Nematic Liquid Crystal Spatial Light Modulator
OTF	Optical Transfer Function
PALM	Photoactivated Localization Microscopy
PBS	Phosphate-Buffered Saline
PC	Personal Computer
PMT	Photomultiplier Tube
PoBS	Polychromatic Beam Splitter
PSF	Point Spread Function
QE	Quantum Efficiency
RMSE	Root Mean Squared Error
RMS	Root Mean Square

SBR	Signal to Background Ratio
SIM	Structured Illumination Microscopy
SLM	Spatial Light Modulator
SMLM	Single Molecule Localization Microscopy
SNR	Signal-to-Noise Ratio
SPI	Serial Peripheral Interface
STED	Stimulated Emission Depletion Microscopy
STORM	Stochastic Optical Reconstruction Microscopy
SXGA	Super Extended Graphics Array
WUXGA	Widescreen Ultra Extended Graphics Array
WXGA	Wide Extended Graphics Array

CHAPTER 1

Introduction to the thesis work

1.1 Introduction

An optical microscope is an imaging tool that uses visible light illumination and a combination of lenses to obtain a high-resolution image of the object. Depending on the illumination mechanism, optical microscopes are divided into two broad categories, namely, widefield microscope [1–3] and point scanning microscope [4–8]. In the widefield microscope, usually an incoherent light source illuminates the specimen plane, and the entire specimen area is imaged simultaneously. Whereas in a point scanning microscope, each point of the specimen is illuminated one at a time and imaged in a sequential manner using beam scanner or a stage scanner. In the case of stage scanner the microscope stage is moved relative to the illumination spot and in the case of beam scanner the illumination spot is moved relative to the stage. At the end of the scanning, image of each point stored in the computer is combined to construct the final image of the scanned area. Owing to its far field imaging capability, the optical microscope has now become an essential tool in diverse areas such as life science [9], nanotechnology [10], biotechnology [11], pharmaceutical research [12] and so on. It is especially very useful to view living biological samples for medical diagnosis, which is not possible with other powerful microscopes such as the electron microscope.

Resolution [13, 14] is a very important parameter of a microscope which represents the capability of the imaging system to distinguish two point objects, placed close to each other, as two separate image points. When a point object is seen through a microscope, due to diffraction it no longer looks like a point rather it looks like a diffraction pattern having a finite width. Such an image of a point object is called point spread function (PSF). The minimum separation between two point objects in the specimen in the lateral direction, provided the microscope forms two distinguishable PSFs in the image plane, is called lateral resolution, while the same

for two point objects in the specimen volume separated in the axial direction is called axial resolution. The lateral resolution of the microscope is primarily responsible for deciding the amount of finer details in the image, whereas the axial resolution decides the depth of field or amount of background light entering the image corresponding to a certain plane in the specimen. Higher axial resolution can thus lead to a property called optical sectioning in an optical microscope.

Therefore it is the PSF of the microscope that determines its resolution limit and the same is considered as a fundamental parameter to characterize the imaging performance of the microscope. The PSF of an optical microscope, hence, is vital in the calibration of the microscope in terms of quantifying the resolution. Besides it is useful in the post-acquisition image deconvolution to further enhance the quality of the image acquired. Deconvolution is a mathematical transformation of the image which reduces the out of focus information or blur present in the image data with the help of the PSF of the imaging system [15].

Ernst Abbe suggested that the resolution of an optical imaging system cannot be more than the limit set by the diffraction phenomenon which is half of the illumination wavelength. However present day microscope users are finding many application areas where they need to go beyond the diffraction limit of resolution [16–18]. In last few decades a number of indirect approaches have been developed which have attempted to push the resolution beyond the diffraction limit. Below we discuss a few such prominent approaches.

Confocal microscope is a special type of point scanning microscope which eliminates the out-of-focus information present in the image using a pinhole placed on a plane conjugate to the object plane placed in front of the detector. The pinhole allows only the in-focus portion of the light from the specimen to reach the detector thus producing a high-resolution optically sectioned image of the specimen [6, 19]. However, the lateral resolution obtained from the confocal microscope is only marginally better than the conventional widefield microscope.

Although the use of array detector in a scanning optical microscope was proposed several decades back [20], only recently the tremendous potential of array detection towards resolution enhancement has been realised. In image scanning microscope (ISM), the point detector of a conventional confocal microscope is replaced by an array detector (i.e. a digital camera) consisting of a two dimensional (2D) array of pixels. The array detector records an image of the illumination beam for each scan position. At the end of the scanning, the microscope thus gathers a 4D array of image data for each pixel of the image. This provides the flexibility to perform a pixel reassignment scheme to construct a final image with enhanced lateral resolution [21, 22].

Resolution can be enhanced in a widefield microscope as well. One such example is structured illumination microscopy (SIM). Here the object is illuminated by a high spatial

frequency grid pattern distribution instead of a uniform distribution of light. The high frequency content of the object can be overlapped with the grid pattern to produce moiré pattern. By moving and rotating the grid pattern in different directions and taking the widefield images of the moiré fringes, a final image can be constructed which has a two fold lateral resolution enhancement as compared to a widefield microscope [23, 24].

Stimulated emission depletion (STED) microscopy is a technique that truly overcomes the diffraction limit in the fluorescence mode of optical microscopes by manipulating the effective emission volume in the illuminated region of the specimen. This is achieved by switching off the fluorescent molecules in the outer regions of the diffraction limited excitation volume via stimulated emission using an intense laser beam called STED beam. Fluorescence from only the narrow region around the optical axis is thus received by the detector to produce a super-resolution image of the specimen [25].

Stochastic optical reconstruction microscopy (STORM) is yet another super resolved imaging technique applicable for a widefield microscope which relies on the stochastic switching of individual fluorophores. The random stochastic switching of fluorophores allows to record temporal separation of individual molecules. Then each fluorophore molecule can be precisely located by finding their position coordinates from the Gaussian fitting of each fluorophore image. The positions of all the individual fluorophores from a large number of image frames are combined to produce the final super-resolution image [26].

In so far as applications are concerned scanning optical microscopes are particularly useful as they allow illumination with a specifically designed laser beam. The illumination beam can in fact have a user defined complex amplitude profile. However in order to achieve the optimal resolution the confocal pinhole needs ideally to have a zero diameter, which then results in no signal received by the detector. Fortunately the use of array detection in a scanning optical microscope has provided much more flexibility to implement non conventional detection. One such approach namely the ISM, discussed already, provides for higher resolution without comprising the signal level. Therefore ISM is gaining popularity in the imaging of biological samples [27, 28] where signal level is usually less. In fact the four dimensional image data provided by such a microscope opens up the possibility of several other resolution enhancement techniques. Nevertheless scanning microscopes using array detection still face a number of challenges such as imaging speed [28] which is limited by either the speed of the scanner or the frame rate of the camera, whichever is the lower. Precision and repeatability of the scanner, especially in case of a high speed operation, are another two important factors effecting performance of array detector based scanning optical microscope.

However, the array detection microscope still cannot provide true super-resolution images, which can be provided by a STED or a STORM microscope. On the other hand building a

STED microscope is a tedious task as it involves a very complex experimental arrangement. In contrast the STORM microscope provides lateral resolution very close to that of the STED microscope while involving a much simpler and cost effective experimental arrangement. Therefore several research groups are using STORM as an alternative for super-resolution imaging technique [29].

In this thesis, we are going to develop a scanning optical microscope with an array detector to achieve enhancement in lateral and axial resolutions in both the reflection and fluorescence mode of the microscope. We will use both a high speed CMOS camera and an ordinary camera, and both galvo mirror based and holographic beam scanning mechanisms, to achieve an optimal imaging speed without compromising on the other performance parameters. We will also develop a PSF estimation scheme to characterize the resolution enhancements achieved in the imaging systems. Usually, the STORM microscopes are not combined with beam scanning microscopes, as these are two different microscopes. However if the two microscopes are combined it will offer the possibility of exploiting the benefits from both the versions for the same specimen being imaged. In this thesis we will attempt to build a combined form of a STORM and an array detector based scanning optical microscope.

Below we provide a chapter wise overview of the entire thesis work.

1.2 Thesis overview:

- Chapter 1: This chapter provides a general introduction to the research problem and an overview of the thesis.
- Chapter 2: In this chapter we start with the principle of the optical microscope, in particular, the widefield and point scanning microscopes. The theory of image formation in the widefield and confocal microscope is outlined, followed by a discussion on optical resolution and the optical transfer function. We then discuss the present state of the art in regards to resolution enhancement techniques in optical microscopy and motivation behind the present thesis.
- Chapter 3: This chapter aims to describe the important techniques and components associated with the beam scanning microscopes developed in this thesis. We start with a discussion on the illumination beam shaping using the computer generated holography (CGH) technique. We explain how binary holograms can be implemented with a spatial light modulator to dynamically reconfigure the properties of a laser beam in real time. This is followed by the descriptions of the important hardware components required to

build the microscope. The chapter concludes with the illustration of the proof-of-principle experimental setup as an example of the proposed array detection microscope.

- Chapter 4: In this chapter, we introduce a PSF estimation scheme that can estimate the imaging PSF of an optical microscope irrespective of the imaging technique involved. The chapter begins with the stepwise description of the proposed scheme along with a flowchart diagram. We then employ the proposed scheme on a one dimensional (1D) numerically constructed target followed by a two dimensional (2D) numerically constructed target. We then experimentally demonstrate the proposed scheme in a widefield and a point scanning microscope.

- Chapter 5: The chapter presents the implementation of a beam scanning microscope with an array detector. We first develop an array detection microscope using galvo mirror based beam scanner and a high speed camera, and then another array detection microscope exploiting the holographic beam scanning mechanism and an ordinary low speed camera. We demonstrate implementation of image scanning microscopy for lateral resolution enhancement and image subtraction microscopy for axial resolution enhancement. We further introduce a novel intensity subtraction microscopy scheme for axial resolution enhancement. We present results from proof-of-principle experiments to show working of our imaging systems in both reflection and fluorescence modes.

- Chapter 6: In this chapter, we first describe the implementation of a STORM microscope to obtain super-resolution images of fluorescent specimens. We then combine the STORM with our array detection beam scanning microscope to enable super-resolved fluorescence imaging as well as reflected light imaging of the same part of the specimen.

- Chapter 7: In this chapter, we provide a summary of the research work carried out. We also provide a discussion on the possibility of future works in connection with the imaging systems developed in this thesis.

CHAPTER 2

Introduction to optical microscope

2.1 Introduction

An optical microscope has tremendous importance in areas cutting across disciplines such as life science, medical science, material science, nanotechnology and so on. The most significant advantage of the optical microscope is that it can image in the far field in a non-invasive way, facilitating imaging of life biological samples involving minimal sample preparation steps. This thesis work involves resolution enhancement in both the reflection mode and the fluorescence mode of an optical microscope, so in this chapter, we begin with a brief introduction to the optical microscopes, the widefield and the point scanning microscopes. We then discuss the theory of image formation and further develop it to introduce the concept of resolution. This is followed by a brief review of the recent developments regarding the enhancement of resolution in various optical microscopes. The chapter ends with a brief discussion on the motivation behind the thesis work.

2.1.1 Widefield microscope

Depending on the illumination type, optical microscopes are classified into two broad categories, such as widefield microscopes and point scanning microscopes [30, 1]. In the widefield microscope, the source illuminates an extended area of the sample, and the entire area is imaged simultaneously. While in a point scanning microscope, each point of the sample is illuminated and imaged separately, to later construct an electronic image of the sample. If the image is formed using the reflected light from the sample, then the microscope is said to be working in the reflection mode. If the image is formed using the fluorescence light emitted by the molecules in the sample, then the microscope is said to be working in the fluorescence mode.

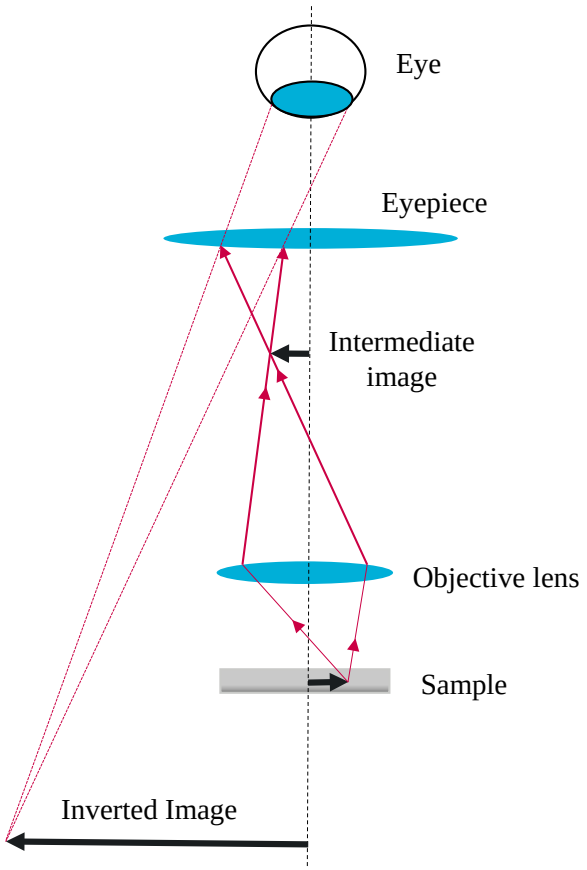

Figure 2.1: A schematic diagram of the conventional widefield microscope

Widefield microscopy is most suitable for 2D imaging of thin samples, however, it is not useful for acquiring images of samples having large depths because light from out of focus planes can blur the captured image.

A simplified schematic diagram of image formation in a standard optical microscope is shown in Fig. 2.1. The objective lens collects light from the sample and it forms an intermediate image. Yet another lens called eyepiece then forms the final image of the sample that can be viewed directly by the eye or can be recorded on a camera. However, modern microscopes use infinity-corrected objective lens. In such a system, another lens called a tube lens must be placed between the objective lens and eyepiece to form the intermediate image. In Fig. 2.1, the final image formed is a virtual one, however, the eyepiece lens can be repositioned to form a real image on a camera. In this microscope, the object is uniformly illuminated through the objective lens. The magnification achieved in the final image is dependent on the magnification provided by the objective lens and the same provided by the eyepiece.

2.1.2 Point scanning mocroscope

In a point scanning microscope, each point of the sample is illuminated and imaged one by one. This requires scanning of the sample with a relative movement between the illumination spot and the sample. The scanning can be achieved either with a galvo mirror based beam scanner or with a stage scanner attached to the sample plane. The signal from the sample for each scan position is stored in a computer, and at the end of the scanning process, the stored data is converted to an electronic image of the sample.

Confocal microscope

As stated earlier, in the widefield microscope, the image may contain unwanted light that comes from out of focus planes of the object. The contribution of the background light can result in reduced resolution and contrast in the image. M. Minsky invented a point scanning microscope in 1957, known as the confocal microscope, which can solve this problem by selectively blocking the light coming from out of focus planes of the object [31]. A confocal microscope is thus a special type of point scanning microscope that uses a pinhole placed in front of the detector to block the out of focus light coming from above and below the plane of focus.

The pinhole positioned conjugate to the illumination spot acts as a spatial filter to form a superior image of each point on the sample plane. The revolutionary idea of Minsky has resulted in the removal of blur from the image, enhancement in effective resolution, and improvement in the signal to noise ratio. With these advantages, the confocal microscope facilitates imaging deep inside the tissue in a non-invasive manner [32]. Minsky used a conventional filament lamp as the source, however, later lasers were introduced as illumination sources [33] as they can produce extremely bright light at very specific wavelengths. Another development is the use of highly sensitive photo-detectors (Photomultiplier tubes (PMTs)) to receive even very weak light from the sample.

The basic principle of the confocal microscope is depicted in Fig. 2.2. The illumination of only one point at a time on the focal plane is achieved by using light coming through a pinhole. The reflected light from the object is focused by the objective lens on another pinhole placed conjugate to the focal plane and in front of the detector. The pinhole allows all the light to pass through it if the light is coming from the focal plane (when the sample plane is in focus and illustrated by red solid rays). The out of focus light from the sample represented by gray dashed lines gets blocked by the pinhole. This property of the microscope leads to an enhancement in axial resolution, which is also referred to as optical sectioning. Similarly, the light coming

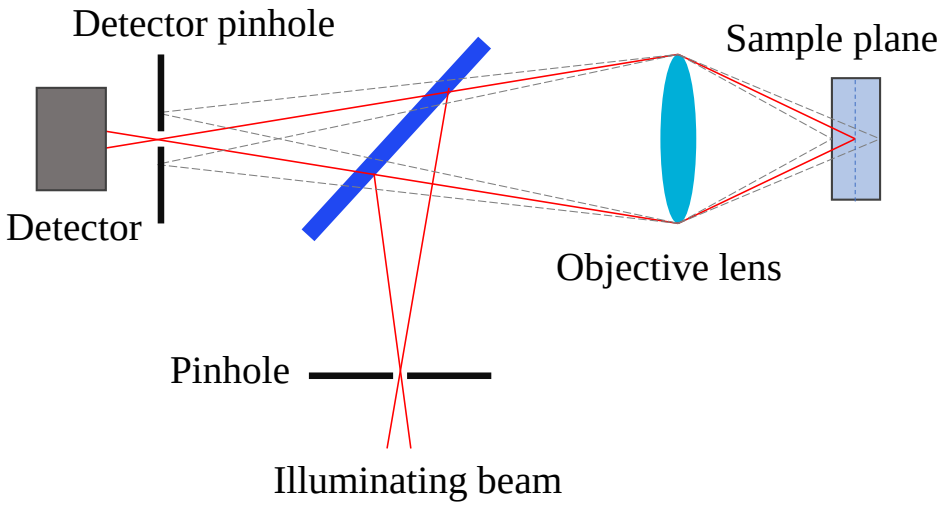

Figure 2.2: Basic principle of confocal microscope.

from the in-focus off-axis points is also blocked, which gives rise to a marginal improvement in the lateral resolution. The setup is shown in Fig. 2.2 uses stage scanning to form the image.

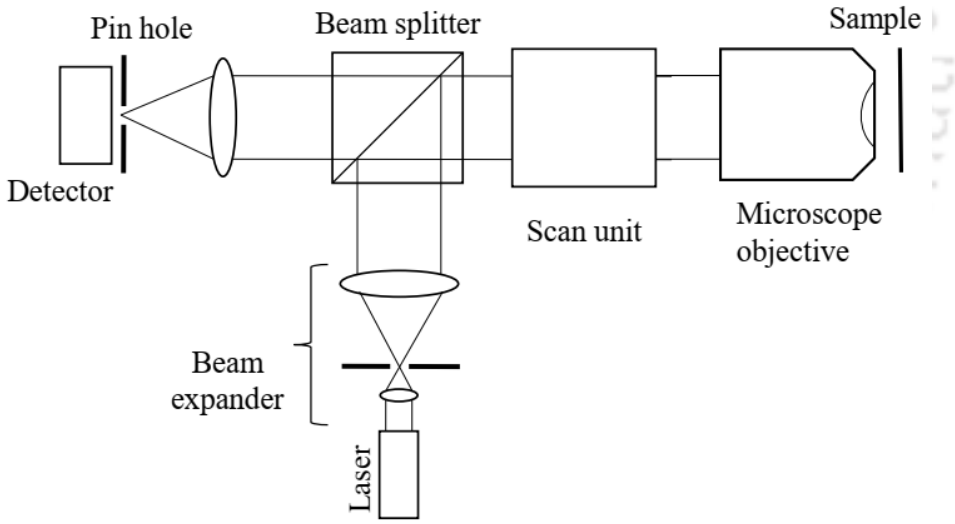

Figure 2.3: Schematic diagram of beam scanning confocal microscope in epi-illumination mode.

However, present day confocal microscopes mostly use beam scanners to construct the image. The schematic diagram of a conventional beam scanning confocal microscope is shown in Fig. 2.3. Light from a laser is expanded and collimated to be incident on a scan unit after reflection from a beam splitter. The scan unit is responsible for the rapid beam movement on the sample plane in a raster fashion. The reflected or emitted light collected by the objective is

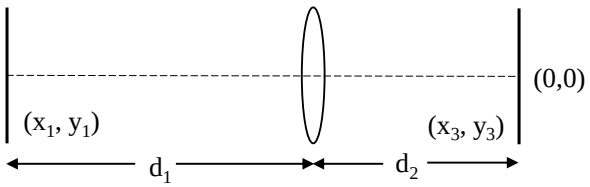

Figure 2.4: The image formation by a simple lens.

descanned by the same scan unit and proceeds towards the beam splitter. The beam splitter transmits part of the beam to be focused by a lens on a pinhole placed in front of the detector. For reflected light imaging, the beam splitter can be a 50/50 beam splitter, while for fluorescence imaging, the beam splitter has to be a dichroic beam splitter (DBS). The dichroic Beam splitter reflects the shorter wavelength light coming from the laser towards the sample, while longer wavelength fluorescent light coming from the sample is transmitted towards the detector.

2.2 Theory of image formation

We now discuss the theory behind image formation in an optical microscope. Depending on the illumination type, imaging can be of two kinds, such as coherent imaging and incoherent imaging. Here we first consider coherent imaging. We take the simplest form of an imaging system comprising a single lens, as shown in Fig. 2.4. The object is kept at a distance d_1 before the lens and the image is formed at a distance d_2 after the lens. (x_1, y_1) are the object plane coordinates and (x_3, y_3) are the image plane coordinates.

If the amplitude at the object plane is $U(x_1, y_1)$, then the amplitude in the image plane [4, 13], ignoring the constant terms, can be written as

$$U(x_3, y_3) = \iint_{-\infty}^{+\infty} U(x_1, y_1) h(x_3/M - x_1, y_3/M - y_1)\, dx_1\, dy_1 \tag{2.1}$$

Here M is the magnification equal to, $\frac{d_2}{d_1}$, and h is the impulse response of the imaging system or the amplitude point spread function (PSF). It can be shown [13] that the amplitude PSF is in fact the Fraunhofer diffraction pattern of the pupil function of the imaging lens. Therefore

$$h(x, y) = \iint_{-\infty}^{+\infty} P(x_2, y_2) \exp\left[\frac{2\pi i}{\lambda d_1}(x_2 x + y_2 y)\right] dx_2\, dy_2 \tag{2.2}$$

where P is the pupil function of the lens.

Equation 2.1, considering unit magnification between object plane and image plane, can also be written as

$$U(x_3, y_3) = U(x_1, y_1) \otimes h(x_3, y_3) \tag{2.3}$$

where $\otimes$ denotes the convolution operation.

For a lens of radius a, we can write its pupil function as

$$P(r) = \begin{cases} 1 & r \leq 1 \\ 0 & \text{otherwise} \end{cases} \tag{2.4}$$

where

$$r = r_2/a \tag{2.5}$$

and $r_2 = \sqrt{x_2^2 + y_2^2}$. Thus the amplitude PSF [13] can be written as

$$h(r_3) = 2\pi \int_0^1 J_0(2\pi r_3 r)\, r\, dr \tag{2.6}$$

where J_0 is the zero order Bessel function of first kind.

Therefore using the property of Bessel functions and ignoring some constant terms we can

$$h(v) = \frac{2J_1(v)}{v} \tag{2.7}$$

where J_1 is the first order Bessel function of first kind and v is the normalised optical coordinate expressed in terms of radial coordinate of the image plane as

$$v = \frac{2\pi}{\lambda} r_3 \sin\theta \tag{2.8}$$

In the expression of v, $\sin\theta$ is the numerical aperture (NA) of the imaging lens.

Now the intensity in the image plane can be written as

$$I(x_3, y_3) = |U(x_3, y_3) \otimes h(x_3, y_3)|^2 \tag{2.9}$$

However if the imaging is incoherent, which can happen when the illumination is incoherent or light from different locations of the sample plane is mutually coherent, the relation in Eq. 2.3 no longer holds. In such a situation Eq. 2.3 gets modified [13] as

$$I(x_3, y_3) = |U(x_3, y_3)|^2 \otimes |h(x_3, y_3)|^2 \tag{2.10}$$

The above expression applies to a widefield microscope working in the fluorescence mode, however, we have ignored the difference between the excitation and emission wavelengths due to the Stokes shift [34].

2.2.1 Two point resolution

The term $|h(x_3,y_3)|^2$ is defined as the intensity PSF and for a circular pupil its expression is $|\frac{2J_1(v)}{v}|^2$ known as the Airy pattern. Assuming that the object plane contains a unit amplitude point source at the location (x_s,y_s) we can write

$$|U(x_3,y_3)|^2 = \delta(x_3 - x_s, y_3 - y_s)$$

. Now we have $I(x_3,y_3) = |h(x_s,y_s)|^2$. Thus the intensity PSF is also represents the image of a point object. Therefore if the object plane contains multiple point objects then whether each pair of adjacent point objects are resolved in the image plane is decided by the width of the intensity PSF.

Rayleigh defined a resolution criterion which states that two points are considered to be just resolved when the distance between the two points, d, is such that the second point is situated over the first dark ring in the Airy pattern of the first point. Thus

$$d = \frac{1.22\lambda}{2NA} \tag{2.11}$$

2.2.2 Optical transfer function ($\mathscr{H}$)

For an incoherent imaging system we now have

$$Image = Object \otimes PSF \tag{2.12}$$

If we take the Fourier transform of the above equation and use the convolution theorem,

$$\mathscr{F}[Image] = \mathscr{F}[Object] \times \mathscr{F}[PSF] \tag{2.13}$$

The second term in Eq. 2.13 is expressed as

$$\mathscr{F}[PSF](k_x,k_y) = \iint_{-\infty}^{+\infty} |h(x,y)|^2 \exp[-i(k_x x + k_y y)]\, dx\, dy \tag{2.14}$$

is known as the optical transfer function (OTF), where (k_x, k_y) are the spatial frequency coordinates. The normalized form of the optical transfer function is written as

$$\mathscr{H}(k_x,k_y) = \frac{\iint_{-\infty}^{+\infty} |h(x,y)|^2 \exp[-i(k_x x + k_y y)]\, dx\, dy}{\iint_{-\infty}^{+\infty} |h(x,y)|^2\, dx\, dy} \tag{2.15}$$

Therefore, the OTF is a complex weighting factor in the Fourier space, which can be used to model the process of image formation by multiplying it with the Fourier transform of the object. The image of the object due to the PSF is realized in real space by simply taking an inverse Fourier transform of the product. Thus the achievable resolution in an imaging system is also determined by the shape of the OTF.

The OTF of a standard widefield microscope with circular, aberration-free pupils is can written as [4]

$$\mathscr{H}(k) = \begin{cases} \frac{2}{\pi}\left[\cos^{-1}\left(\frac{k}{2k_0}\right) - \frac{k}{2k_0}\sqrt{\left(1-\left(\frac{k}{2k_0}\right)^2\right)}\right] & \text{if } k \le 2k_0 \\ 0 & \text{otherwise} \end{cases} \tag{2.16}$$

where $k = \sqrt{k_x^2 + k_y^2}$ and $k_0 = \frac{a}{\lambda\, d_2}$. Therefore the resolution limit of such a microscope is given by the condition $k = 2k_0$. According to this condition two points separated by d in the object plane are just resolved if

$$d = \frac{0.5\lambda}{NA} \tag{2.17}$$

This criterion is known as Abbe resolution criterion. However it is to be noted that the expressions above correspond to an ideal imaging system only.

2.2.3 Point scanning microscope

To understand the image formation in a point scanning microscope, we consider the setup shown in Fig. 2.5 working in the transmission mode. Light from a point source located in the plane (x_1, y_1) is focused onto the sample plane (x_3, y_3) using an objective lens. The complex amplitude of the target kept in the sample plane is given as $t(x_3, y_3)$ which is then multiplied by the amplitude PSF $h_1(x_3, y_3)$ due to the objective lens. Therefore considering that the sample plane is on a stage with scan positions as (x_s, y_s), the complex amplitude just after the sample plane is $h(x_3, y_3)t(x_3 - x_s, x_3 - y_s)$. If $h_2(x_5, y_5)$ is the amplitude PSF due to the condenser lens, then the complex amplitude in the image plane can be written as

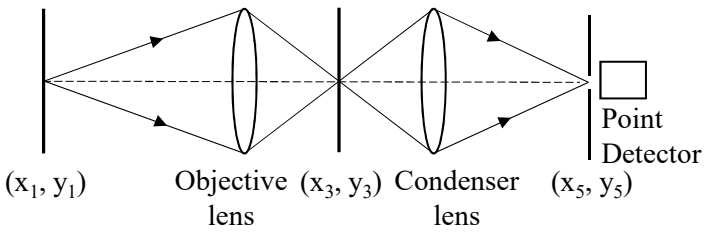

Figure 2.5: The image formation of a conventional scanning confocal microscope.

$$U(x_5,y_5) = \iint h_1(x_3,y_3)t(x_3-x_s,y_3-y_s)h_2(x_5-x_3,y_5-y_3)\,dx_3\,dy_3 \tag{2.18}$$

However if there is a point detector located on-axis then the expression gets modified as

$$U(0,0) = \iint h_1(x_3,y_3)t(x_3-x_s,y_3-y_s)h_2(-x_3,-y_3)\,dx_3\,dy_3 \tag{2.19}$$

Assuming that h_2 is even (which is true for a circular pupil with a uniform illumination profile) we can write

$$U(x_s,y_s) = (h_1(x_5,y_5)\,h_2(x_5,y_5)) \otimes t(x_5,y_5) \tag{2.20}$$

Thus in the case of point scanning microscope with a point detector considering coherent imaging, the resultant amplitude PSF to obtain the image is the product of the amplitude PSFs of the condenser and the objective lens. In the case of incoherent imaging and in the epi-illumination mode, the intensity in the image plane can be written as

$$I(x_s,y_s) = |h(x_5,y_5)|^4 \otimes |t(x_5,y_5)|^2 \tag{2.21}$$

Thus the intensity PSF in such a case is given as $|h|^4$ where h is the intensity PSF due to the objective lens which is also acting as the condenser lens.

The variation of the intensity PSF of a widefield microscope in the axial direction is given by[35, 14]

$$|h(u)|^2 = \left(\frac{sin\ u/4}{u/4}\right)^2 \tag{2.22}$$

where $u = \frac{2\pi(N.A)^2 z}{n\lambda}$ is the normalised optical coordinate corresponding to the axial position z.

Therefore for a confocal microscope, assuming incoherent imaging, the intensity PSF in the ideal case is described in the transverse direction as

$$h_{conf}(v) = |h(v)|^4 = \left(\frac{2J_1(v)}{v}\right)^4 \tag{2.23}$$

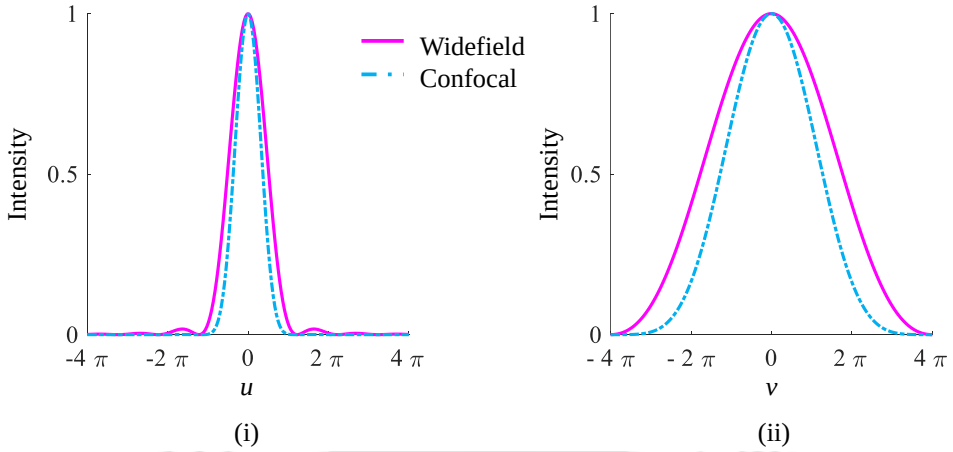

Figure 2.6: Self normalized plots of the intensity PSFs for the widefield microscope and the confocal microscope, (i) in lateral direction (ii) in axial direction.

and in the axial direction as

$$h_{conf}(u) = |h(v)|^4 = \left(\frac{sin\ u/4}{u/4}\right)^4 \tag{2.24}$$

2.3 Resolution enhancement techniques in optical microscopy

From our discussion in the above section, we have found that the resolution of an ideal widefield microscope can at best be the Abbe resolution limit. Since this limit is set due to the finite width of the intensity point spread function, which is the outcome of diffraction from the pupil of the focusing lens, it is also referred to as the diffraction limit. In order to resolve separations smaller than this resolution limit, one has to break the diffraction barrier. The electron microscope can provide finer details with a much higher resolution [36] than an ideal optical microscope. However, such imaging techniques are not suitable for all kinds of samples, especially for biological samples [37]. Nevertheless, there exist phenomena taking place at the sub-wavelength scale [38–41] in various areas which can better be studied with an optical microscope. In the last several decades, there have been a number of developments to improve the resolution of optical microscope beyond that is achievable in a conventional widefield microscope. Below we will briefly discuss some of such important developments.

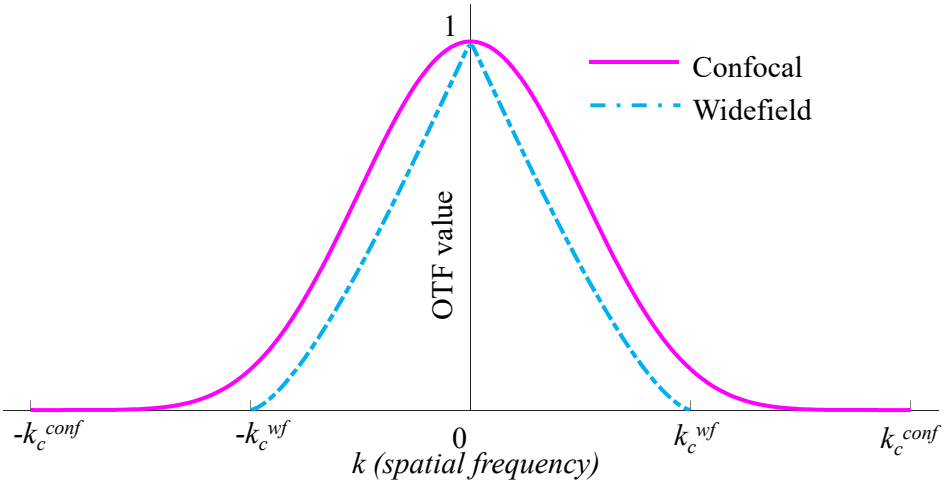

Figure 2.7: Comparison of widefield and confocal OTFs.

2.3.1 Confocal microscope

Arguably the most successful resolution enhancement technique in optical microscopy is the confocal microscopy technique compared to the widefield microscopy technique within the diffraction limit. Figure 2.6 shows plots of the intensity PSFs of a widefield microscope and a confocal microscope. The lateral resolution of an optical microscope is decided by the width of the intensity PSF in the transverse direction. Figure 2.6 (i) shows that the intensity PSF in the transverse direction for the confocal microscope is narrower than the same for the widefield microscope. This leads to an enhancement in the lateral resolution by a factor of 1.32 in the confocal microscope. On the other hand, there is a significant enhancement in the axial resolution in the confocal microscope as indicated by the plots of intensity PSF in the axial direction, as shown in Fig. 2.6 (ii). The enhancement in lateral resolution in the confocal microscope relative to the widefield microscope is also indicated in the plots of OTF for the two microscopes, as seen in Fig. 2.7. Therefore the confocal microscopy technique significantly enhances the axial resolution while marginally enhancing the lateral resolution.

2.3.2 Confocal microscopy with array detectors

Sheppard et al. proposed about three decades back that the point detector in the confocal microscope can be replaced by an array detector. The array detector can be a digital camera or a multi channel photomultiplier tube. The use of the array detector in a confocal microscope can enhance both the lateral as well as axial resolutions [42]. Another novel idea was to use the data captured by the array detector to do a pixel reassignment [20] in order to break the diffraction barrier of resolution. However, this idea of pixel reassignment has become popular only recently

after the demonstration about a decade back [21, 22]. This microscopy technique nowadays is known as image scanning microscopy (ISM). Likewise, the point scanning microscope in ISM also the illumination spot scans the sample area. In contrast, to the point scanning microscope here, the light from the sample plane for each scan position is stored in a two dimensional array. Let $I(\mathbf{r},\mathbf{s})$ represent the image data by the array detector at the location $\mathbf{s}$ corresponding to the scan position $\mathbf{r}$. At the end of the scanning, this image data is used to construct an effective image after the pixel realignment using the below equation [21].

$$I_{eff}(\mathbf{r},\mathbf{s}) = \int \mathbf{I}(\mathbf{r} - \frac{\mathbf{s}}{\mathbf{2}},\mathbf{s})\mathbf{ds} \tag{2.25}$$

By employing the image scanning microscope, the lateral resolution can be increased about twice than the conventional confocal microscope along with a 4 fold increase in the contrast [43]. Due to its capability to provide higher resolution images without any loss in the signal-to-noise ratio, ISM is increasingly finding applications involving low light, such as in biological science and medical science [27, 44–46].

2.3.3 Stimulated emission depletion microscopy

In a conventional laser scanning confocal microscope, the resolution achievable depends on the size of illumination volume, i.e., the intensity PSF, as discussed earlier. If the spatial extent of the intensity PSF decreases, then the resolution is increased. Decreasing the spatial extent of the PSF by designing the illumination beam or by controlling the properties of the illumination beam is called as point spread engineering. Use of point spread function engineering in a confocal microscope can marginally enhance its resolution. However, such an enhancement in resolution is still not sufficient to be comparable with the resolution of an electron microscope. Stimulated emission depletion (STED) microscopy technique significantly enhances the resolution of a confocal microscope working in the fluorescence mode. This technique uses two beams, one is the normal excitation beam, and the other is the STED beam, which is a specially designed beam with a doughnut-shaped illumination spot [25].

To understand the principle of the STED microscope, we consider the Jablonski diagram, as shown in Fig. 2.8 (i). The excitation beam incident on the fluorescence molecule raises the molecule from the ground state to the excited state. At the excited state, the molecule undergoes a vibrational relaxation, hence loses some energy and drops to the ground state leading to fluorescence emission. However, before the fluorescence emission takes place if the molecule is interacted by a photon of appropriate wavelength, then the molecule undergoes stimulated emission. Such a molecule will be unavailable for the fluorescence emission.

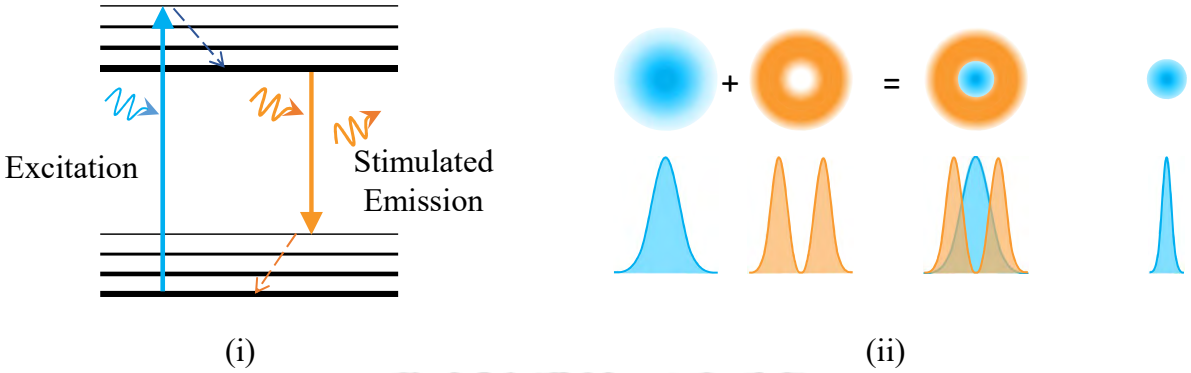

(i) (ii)

Figure 2.8: (i) Jablonski diagram showing stimulated emission. (ii)Illustration depicting the basic principle of STED microscope.

Figure 2.8 (ii) shows a schematic of the excitation beam and the doughnut shaped STED beam. Due to the stimulated emission process, the excitation volume in the region of overlap gets depleted. This reduces the effective volume of the excitation PSF. The expression for the resolution of the STED microscope can be written as [47]

$$\Delta r = \frac{\lambda}{\left(2\,NA\sqrt{1+I/I_s}\right)} \tag{2.26}$$

Where I is the intensity of the STED beam and I_s is the saturation intensity. Saturation intensity is defined as the STED intensity at which the probability of stimulated emission becomes equal to the spontaneous decay rate. The lateral resolution of STED microscope can be extended up to 20 *nm* [48–50].

2.3.4 Structured illumination microscopy

So far, we have seen resolution enhancement in scanning optical microscopes only. Resolution enhancement, especially the lateral resolution enhancement, has been achieved in widefield microscopes as well.

Structured illumination is a widefield microscopy technique in which the sample is illuminated by a grid pattern [51] and is overlaid to form an interference pattern on the sample. The concept of structured illumination microscopy can be understood through the moiré effect, i.e., when two fine grid patterns superimpose, a beat pattern called moiré fringe appears [52, 24].

The basic principle of the structured illumination microscope is depicted in Fig. 2.9. The object contains unknown high-frequency details. When a known illumination pattern is superimposed with the unknown pattern of the object, it gives rise to low-frequency moiré fringes. The unknown object details can be extracted by analyzing moiré fringes, which being

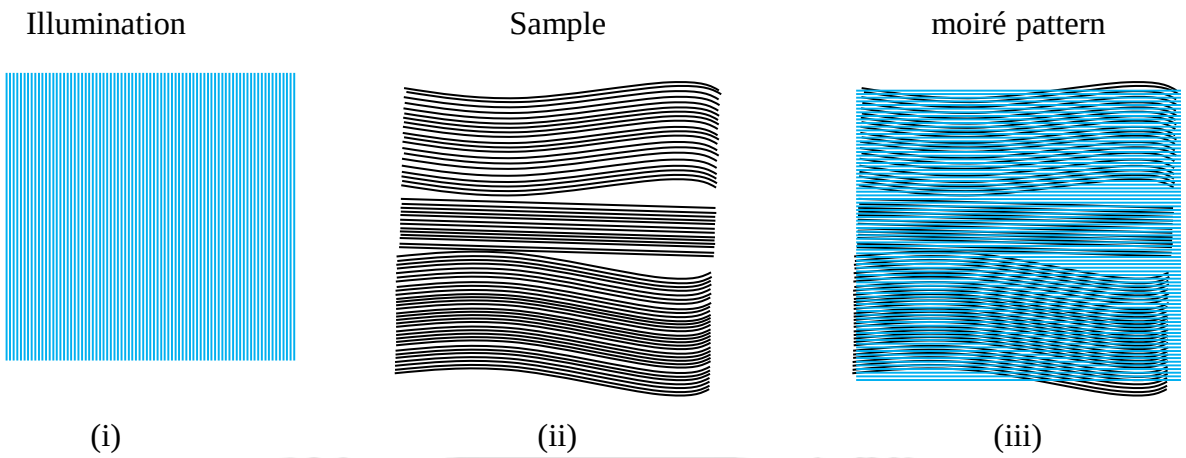

Figure 2.9: Illustration of basic principle of structured illumination microscopy comprising (i) structured illumination pattern, (ii) sample contaning high spatial frequency content and (iii) resultant moir*é* fringes of low frequency.

low frequency are captured by the imaging device. The grid pattern is rotated in several steps, and each step image of the sample is recorded. The subsequent processing with a specialized algorithm leads to the extraction of high-frequency information data to produce a reconstructed image with higher resolution. This technique is capable of doubling the lateral resolution related to a conventional widefield microscope [24].

2.3.5 Single molecule localization microscopy

Optical super-resolution comparable to that achievable with the STED microscope is also possible in a widefield microscope. Below we discuss such a microscopic technique.

The ideal image of a point object such as a fluorescent molecule in a sample has Airy pattern shape. Therefore the fluorescence image of a few well separated molecules will appear as shown in Fig. 2.10 (i). In such a situation, it is easy to locate the centroid of each molecule by doing a Gaussian fitting of the corresponding images. However, problem arises due to the overlap of the image corresponding to one molecule with the nearby molecule. If the majority fluorescence emitters are pushed to the dark state while allowing a small fraction of molecules to emit the fluorescence, the probability of finding two emitting molecules placed close to each other will be less. To construct the image of the entire sample by using the localization data, it will require a number of localization rounds. Each localization round consists of recording sparsely distributed fluorescence molecules, precise centroid localization of each molecule, and computer rendering. Figure 2.10 shows two such localization rounds. A super-resolution image can be achieved by repeating the process until all the molecular locations are recorded [53]. This imaging technique is called the single-molecule localization microscopy (SMLM).

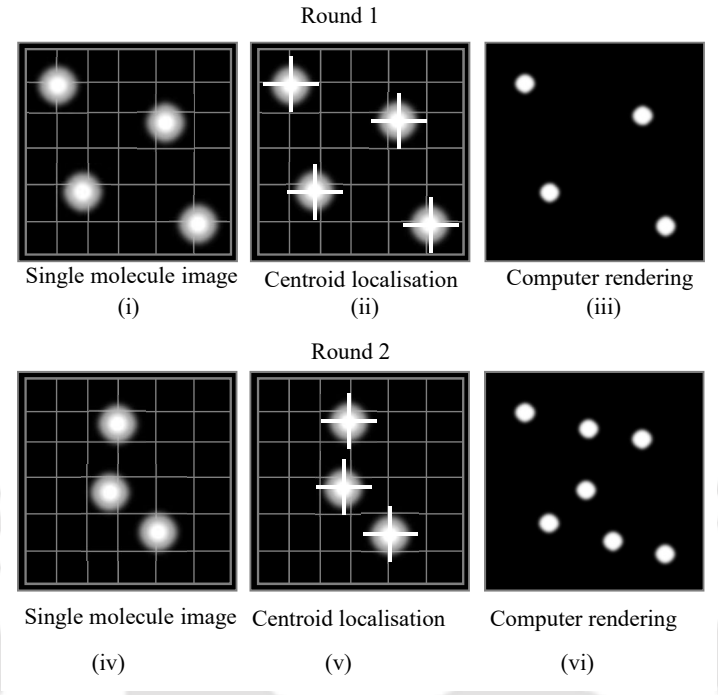

Figure 2.10: Basic principle of single molecule localization microscopy comprising (i) switching of single molecule, (ii) centroid determination of Gaussian photon distribution and (iii) cumulative computer rendering of the molecular localizations.

The SMLM method provides a theoretically unlimited localization accuracy of the individual molecule. However, in practice, the localization accuracy depends on the number of photons being emitted by each molecule [54]. One can write

$$\Delta x = \frac{\lambda}{2NA\sqrt{m}} \tag{2.27}$$

Where Δx denotes the localization accuracy of each localized molecules, and λ represents the excitation wavelength, NA is the numerical aperture, and m is the number of photon emitted from one fluorescent molecule.

The SMLM can be divided into two broad categories, namely photoactivation localization microscopy (PALM) and stochastic optical reconstruction microscopy (STORM). Both PALM and STORM have the same acquisition technique but with a different *on-off* strategy of fluorescent molecules. In PALM, various fluorescent protein is used to localize the molecules, whereas, in STORM, an organic dye is used to label on the sample, which blinks when illuminated with a high power laser source [17].

2.4 Motivation for the proposed work

Point scanning microscope, such as the confocal microscope has a number of advantages compared to other types of optical microscopes. In addition to a significantly enhanced axial resolution, the microscope facilitates the use of different types of lasers as the illumination beam. The illumination beam can have engineered amplitude and phase profiles [55–57] designed to enhance the imaging capabilities of the microscope. Besides, the microscope can use different vector beams such as the radially polarized beam [58, 59] as the illumination beam to extract additional information such as the molecular orientations in the sample. However, to provide the best resolution performance, the pinhole used in front of the detector should have a zero radius. Therefore any attempt to enhance the resolution by reducing the size of the pinhole will lead to a reduction in the signal-to-noise ratio [60–62]. Fortunately, with the use of an array detector in the scanning microscope, it is possible to achieve resolution enhancement without compromising the signal-to-noise ratio as in the image scanning microscopy technique. However use of the array detector such as a digital camera poses a significant problem in terms of the imaging speed of the microscope [28, 46]. In order to enhance the imaging speed in an image scanning microscope, other methods such as the use of multiple illumination beams instead of a single illumination beam, have been explored [63, 64]. Imaging by a scanning optical microscope with an array detector working in the enhanced resolution range also requires a scanner that has very good precision and stability, since, for each scan position, the detector needs to capture a stable illumination beam. Due to this reason, many image scanning microscopes use a piezoelectric stage scanner to perform the scanning [28, 65]. However, piezoelectric scanner has a slow response time that also affects the imaging speed of the microscope. It is also to be noted that the use of pixel reassignment in the image scanning microscope, even though enhances the lateral resolution, it can not achieve the enhanced axial resolution that is possible in a confocal microscope [22, 21].

In this thesis, we develop a scanning optical microscope with an array detector using two types of cameras, one is a fast camera, and the other is an ordinary camera. The illumination beam is designed using a liquid crystal spatial light modulator based holography technique. We use holographic beam scanning and the ordinary camera to implement an image scanning microscope. The holographic beam scanning provides a precise way of scanning the beam, and our scheme enables a reasonable imaging speed even with an ordinary camera. The fast camera is used in combination with a galvanometer mirror scanner scanning the illumination beam. We custom design the scanner driver so that the imaging can take place without compromising much on the imaging speed and the precision of the scanner. We also employ the image data

for each scan position to implement an image subtraction microscopic technique that enhances the axial resolution in the final image.

In an earlier section, we discussed that the resolution performance of an optical microscope is best assessed in terms of its point spread function. The present point spread function estimation schemes are mostly platform dependent, so they work in a particular type of microscope only. In this thesis, we propose a point spread function estimation scheme that can work on any type of optical microscopes.

The STED microscope discussed previously provides an excellent resolution comparable with the resolution of an electron microscope. However this microscope involves a complex experimental arrangement. On the other hand the STORM microscope can be built using less expensive components and the arrangement is much more simpler. In this thesis we implement a STORM microscope and combine it with an array detection microscope. The proposed arrangement enables super-resolution fluorescence imaging and high resolution reflected light imaging of the same sample.

2.5 Summary

In this chapter, we have introduced the optical microscope and various important optical microscopy techniques. We have discussed the theory of image formation and developed the same to define the resolution limit in the optical microscopes. We have done a review of the recent developments towards enhancing the resolution in an optical microscope. We end the chapter with a discussion on some of the existing issues connected with the various resolution enhancement techniques and how this thesis proposes to address some of these issues.

CHAPTER 3

Development of a scanning optical microscope with a user-defined illumination beam

3.1 Introduction

In this chapter, we describe the implementation of a scanning optical microscope that has a user defined illumination beam. The chapter begins with a description of the computer generated holography (CGH) technique using a liquid crystal spatial light modulator (LCSLM) device. The illumination beam for the microscope is designed by writing binary holograms onto the LCSLM panel. We then provide a detailed description of the essential components of the scanning optical microscope, such as the illumination beam, scanning unit, and the detection unit. We incorporate both mechanical and non-mechanical beam scanning units. In the mechanical scanning unit, beam scanning is performed by mechanical movement of mirrors, and in the non-mechanical scanning unit, the beam scanning is performed holographically. Finally, we provide the experimental arrangement of the entire microscope assembly, which will be used as a proof-of-principle setup for the later experiments.

3.2 Beam shaping using computer-generated holography

The illumination beam plays a crucial role in an optical microscope as it decides the effective resolution of the imaging system. In a conventional scanning microscope, the wavefront of the illumination beam at the back focal plane of the objective lens should ideally be plane

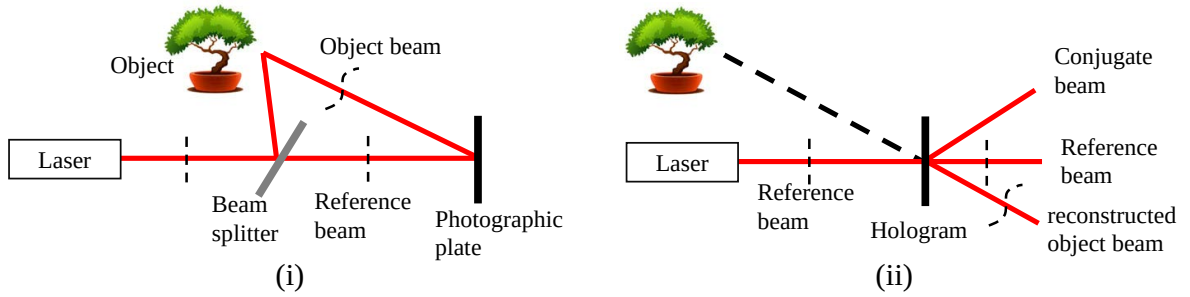

Figure 3.1: A typical arrangement for (i) recording of hologram and (ii) reconstruction of the object beam.

or unaberrated. The lateral resolution and the optical sectioning property of the microscope can be affected by the presence of aberrations induced by the sample or by the optics forming the illumination beam. An aberrated illumination beam also leads to a loss of signal-to-noise ratio of the final image. Active control over the phase profile of the illumination beam enables mitigation of aberration effects on the imaging performance of the microscope. In this thesis, we incorporate the computer generated holography technique to realize an user defined wavefront of the illumination beam.

3.2.1 Holography

Holography is a technique of recording and later reconstructing a wavefront using a photosensitive plate, which after the recording process, is called the hologram. The hologram records the wavefront information in terms of the intensity distribution in an interference pattern. The basic principle of holography is illustrated in Fig. 3.1. Coherent light from a laser is split into two parts by a beam splitter, one part of the beam is directed towards the object, which gets reflected by the object as the object beam, and the other beam travels towards the photographic plate as the reference beam. The reflected or the scattered light from the object, comprising the object beam, carries the information of the object in its phase profile, interferes with the reference beam to form an interference pattern on the photographic plate, as shown in Fig. 3.1 (i). The interference fringes after, being recorded by the photographic plate, become the hologram. Therefore the hologram has a transmittance function proportional to the intensity distribution in the interference pattern. When the reference beam illuminates the hologram, the object beam wavefront is reconstructed in one of the diffracted orders from the hologram. The hologram reconstruction process is shown in Fig. 3.1 (ii). If one looks in a direction opposite to the reconstructed object beam, then a virtual image of the object is seen at the place of the object even if the object is actually not present.

The computer generated holography (CGH) uses the same principle as classical holography discussed above. However, in CGH, the construction of the hologram is carried out numerically by calculating the interference pattern between a plane reference wavefront and the mathematical representation of the desired object beam. The numerically obtained interference pattern is then used to synthesize a physical hologram. The reconstruction process is performed when a collimated laser beam illuminates the hologram to realize the desired object beam [66]. Thus with the help of the CGH technique, it is possible to produce an arbitrary or user defined object beam without even having the real object.

3.2.2 Computer-generated holography

The hologram construction process in the CGH involves two steps, namely the numerical computation of the interference pattern and writing the interference pattern onto a phase mask or a light modulating device. Depending on the amplitude transmittance properties, the hologram synthesized can be of various types, such as sinusoidal and binary. A hologram is called sinusoidal if the transmittance function in the hologram for each fringe has a sinusoidal spatial variation, and is called binary if the amplitude transmittance function has a binary variation. In this thesis, we have mainly employed the binary hologram based CGH technique to generate the user defined illumination beam. Below we discuss the construction of the binary hologram to generate a certain user defined object beam.

Let us consider an object beam with phase $\phi(x,y)$, where (x,y) are the coordinates in the hologram plane that interferes with the reference beam within a unit circular area defined by $\sqrt{x^2+y^2} \leq 1$. In addition to the phase ϕ, the object beam also has tilts described by $\tau(x,y) = m_x x + m_y y$, where m_x and m_y represent tilts along x and y, respectively. Thus the complex amplitude of the object beam assuming uniform unit amplitude can be written as

$$A(x,y) = e^{i\Phi(x,y)} \tag{3.1}$$

Where $\Phi(x,y) = \phi(x,y) + \tau(x,y)$ is the overall phase function of the object beam. The amplitude transmittance function of the binary hologram can be written as [57]

$$t_b(x,y) = \begin{cases} 1 & \text{if } \cos\Phi(x,y) \geq 0 \\ 0 & \text{otherwise} \end{cases} \tag{3.2}$$

When the reference beam illuminates the binary hologram, it gives rise to several diffraction orders, whose origin can be understood by Fourier series analysis of the transmittance function of the binary hologram. It may be seen that the line profile of the binary hologram transmittance function is a square wave with a 50% duty cycle. Using the Fourier series expansion, the square

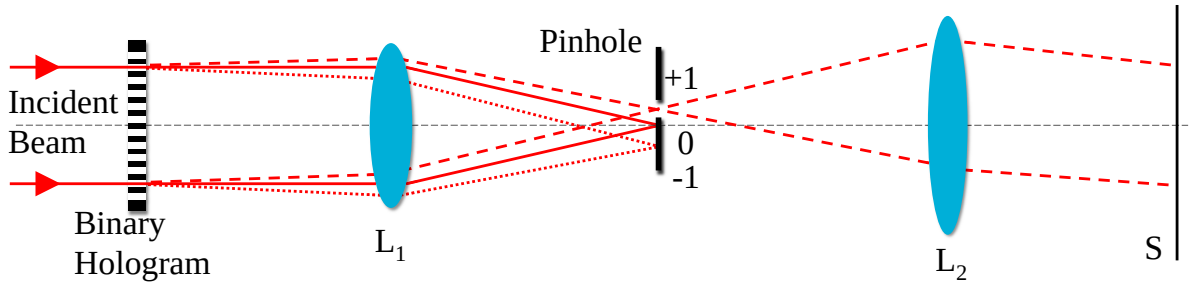

Figure 3.2: Implementation of binary hologram to generate used-defined object beam.

wave can be expressed as the summation of sine function and by applying the Euler's formula we can write the Fourier series expansion as

$$t_b(x,y) = \frac{1}{2} + \frac{1}{\pi}\left[e^{i\Phi} + e^{-i\Phi} - \frac{1}{3}\left(e^{3i\Phi} + e^{-3i\Phi}\right) + \frac{1}{5}\left(e^{5i\Phi} + e^{-5i\Phi}\right) + \ldots\right] \tag{3.3}$$

If we place the binary hologram at the back focal plane of a lens, then the diffraction pattern at the front focal plane will be the Fourier transform of the binary hologram transmittance function, given by

$$T_b(f_x, f_y) = \int\int t_b(x,y)\, e^{\frac{-2\pi i(xf_x + yf_y)}{\lambda f_1}}\, dx\, dy \tag{3.4}$$

Here (f_x, f_y) are the front focal plane coordinates, λ is the wavelength of light, and f_1 is the focal length of the lens. $(k_x = f_x/\lambda f_1, k_y = f_y/\lambda f_1)$ are the coordinates describing the Fourier plane. The first term of the equation 3.3 corresponds to the undiffracted zero order beam while the second and third terms correspond to the ± 1 order diffracted beams carrying phase $\pm\phi$, each with power $\frac{1}{\pi^2}$ of the net incident power. The two beams travel at relative angles $\pm\tau$ with respect to the zero order beam. Additionally there are several higher diffraction orders such as $\pm 3, \pm 5, \pm 7, \ldots$ with relative powers $1/9\pi^2$, $1/25\pi^2$, $1/49\pi^2$, $\ldots$ carrying phase $\pm 3\phi$, $\pm 5\phi$, $\pm 7\phi, \ldots$ and travelling at relative angles $\pm 3\tau$, $\pm 5\tau$, $\pm 7\tau, \ldots$, respectively. Since the $+1$ order beam has the same phase profile as that of the object beam, therefore, the same beam can be isolated to obtain an illumination beam with user defined phase $\phi(x,y)$. Figure 3.2 illustrates the generation of the illumination beam by implementing a binary hologram. A collimated laser beam acting as the reference beam is incident on the binary hologram constructed using the CGH technique. By choosing appropriate values of the tilts along x and y directions, it is possible to isolate the $+1$ order from the other orders using a combination of lens L_1 and pinhole. The beam is then re-collimated by the lens L_2 to realize the desired phase profile on the screen S, which is optically conjugate to the hologram plane. The back focal plane of the

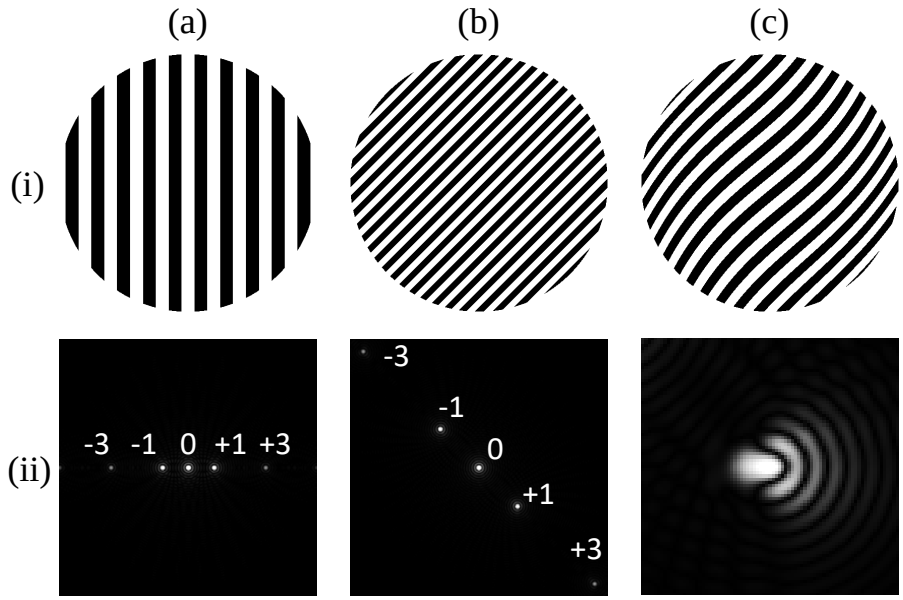

Figure 3.3: Binary hologram with (i)(a) $m_x = 10\pi$, $m_y = 0$, (b) $m_x = 15\pi$, $m_y = 15\pi$, (c) $m_x = 10\pi$, $m_y = 10\pi$ and $Z_7 = 1$. The corresponding Fourier planes obtained numerically by MATLAB are shown in (ii)(a→c). To be noted that (ii) (c) shows a magnified view of the +1 order spot.

microscope objective lens can be positioned at S or conjugate to S to realize the illumination beam of the microscope with user defined phase profile.

To be noted that $\phi(x,y)$ represents pure phase variation of the object beam and excludes the tilts. If $\phi(x,y) = 0$, then the binary hologram resembles a square wave diffraction grating. In this thesis, we use the phase $\phi(x,y)$ to represent the monochromatic aberrations expressed as a linear combination of Zernike polynomials. Here we use single index Zernike circular polynomials [67]. We assume $\phi(x,y) = \sum_j a_j Z_j$, where a_j is the RMS (root mean square) amplitude in radian of the j^{th} Zernike mode. Some of the single index Zernike polynomials that correspond to some common aberration modes are shown in Appendix A [68].

Figure 3.3 shows numerically constructed binary holograms with different tilts and aberrations to realize the user defined $+1$ order diffraction pattern on the Fourier plane. Thus by implementing the binary hologram computed using the CGH technique, a user defined object beam can be generated and further be used as the illumination beam of the microscope. The illumination beam can also be made aberration free by incorporating an appropriate linear combination of the Zernike polynomials for improvement in the imaging performance of the microscope. However, it still requires a means to synthesize the hologram to implement the computed hologram patterns. In this thesis, we use a liquid crystal spatial light modulator

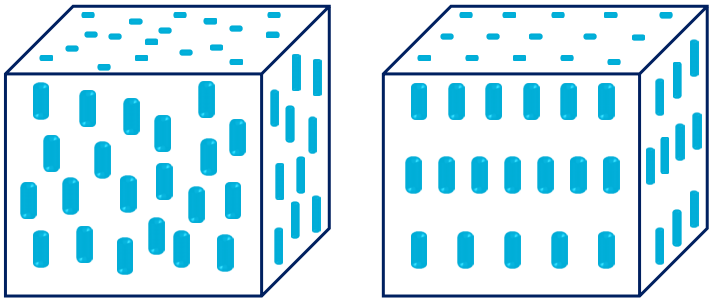

(i) (ii)

Figure 3.4: Distribution of liquid crystal molecules in (i) nematic (ii) smectic phases.

(LCSLM) to synthesize binary holograms. LCSLM devices with a computer interface facilitate reconfigurable and real time implementation of binary holograms.

3.2.3 Liquid crystal spatial light modulator

A spatial light modulator (SLM) is a device used for modulating the phase, amplitude, polarization, or the propagation direction of the incident light beam [69]. SLMs are primarily of two types, namely, optically addressed and electronically addressed SLMs [70, 71]. Optically addressed SLM uses incoherent light for controlling the modulation, whereas electronically addressed SLM uses electrical signal for controlling the modulation. Again electrically addressed SLMs can be of several types, such as liquid crystal, magneto-optic [72], deformable mirror [73], and multiple quantum well [74]. As stated previously, in this thesis work we use the liquid crystal spatial light modulator (LCSLM) for modulating the incident laser beam.

The LCSLM device comprises a two dimensional array of liquid crystal cells or pixels. Each pixel of the LCSLM contains liquid crystal molecules placed between two glass sheets. These liquid crystal molecules are the main constituents of the LCSLM pixel having physical properties that are intermediate between conventional isotropic liquid and crystalline solid. They exhibit mechanical properties of liquids such as high fluidity, formation, and coalescence of droplets. However, they also exhibit anisotropy in their optical, mechanical, electrical, and magnetic properties, as observed in crystalline solid [75, 76]. The liquid crystal is classified into several types and the three main ones being such as, thermotropic, isotropic, and polymeric, among which thermotropic liquid crystals have been studied extensively due to the wide range of applications, including in LCSLM. The physical properties of thermotropic liquid crystals depend on the ambient temperature, and the material exists in three phases, namely, nematic, smectic, and cholesteric. It is mostly the nematic and smectic phases that are used in the pixels of the LCSLM.

The liquid crystal molecules are elongated in shape with a long axis called the director. In the nematic phase, the molecules are positioned randomly all over the volume with a common orientation of the director axes. In the smectic phase the liquid crystal molecules along with a common orientation of the director axes, are also positioned in different layers. Figure 3.4 shows the molecular orientation in a cross section of the liquid crystals of the nematic and smectic phase. LCSLM devices made of nematic liquid crystal pixels are called nematic LCSLM (NLCSLM) and made of a special type of smectic liquid crystal (i.e., smectic-C*) are called ferroelectric LCSLM (FLCSLM).

Nematic liquid crystal spatial light modulator

In a nematic liquid crystal pixel, the liquid crystal molecules are kept in a cell, with two alignment layers in opposite directions, each layer having scratch marks in a mutually perpendicular direction with respect to the other. Nematic liquid crystal molecules tend to remain aligned with their nearby molecules, and those near the alignment layers align along the scratch marks. Thus overall, the molecules form a 90° twist, as shown in Fig. 3.5 (i) from one alignment layer to the other alignment layer. Therefore if linearly polarized light propagates through such a nematic liquid crystal cell with the polarization parallel to the scratch mark of the front layer, the incident light experiences a polarization change of 90° as the beam comes out from the cell. If an analyzer is placed at the exit face with its axis parallel to the scratch mark in the front layer, the incident beam will be blocked. However, when an AC electric field is applied across the liquid crystal cell via two transparent electrodes, the induced dipole moments of the molecules force the long axes to align parallel to the direction of the applied electric field, as shown in Fig. 3.5 (ii). As a result, the incident light beam will not experience any polarization rotation and is hence completely transmitted by the analyzer. Therefore each pixel of the NLCSLM can be made transparent or opaque for the incident polarized light by applying an appropriate external electric field across the pixel [77].

In this thesis work, we use two NLCSLMs, namely “LC- R 720 SLM” and “LC- R 1080 SLM” from HOLOEYE Photonics AG, Germany. Both the LCSLMs are reflective type based on liquid crystal on silicon (LCoS) display technology. The “LC- R 720 SLM” has a pixel resolution of WXGA (1280 H $\times$ 768 V) and a pixel pitch of 20 μm spanning over an active area of 25.6 $mm \times 15.4\ mm$. It has an image display frame rate of up to 180 Hz. The “LC- R 720 SLM” has a pixel resolution of WUXGA (1920 H $\times$ 1080 V) with a pixel pitch of 8.1 μm spanning over an active area of 16.39 $mm \times 10.56\ mm$. It has an image display frame rate of up to 60 Hz. Both the NLCSLMs can display 8 bit images from the computer graphics card via a DVI interface [78, 79], such that 8 bit value of an image pixel defines the magnitude of the

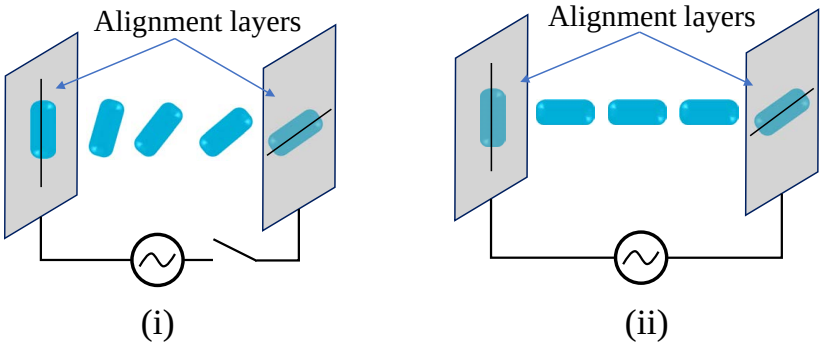

Figure 3.5: Molecular orientation of twisted nematic liquid crystals (i) in absence of applied AC electric field, and (ii) in presence of applied AC electric field.

AC field applied across the respective LCSLM pixel. If the 8 bit image comprises two values, 0 and 255 only, the same can represent binary holograms to be realized with the NLCSLMs.

Ferroelectric liquid crystal spatial light modulator

As stated already, the FLCSLM consists of cells filled with liquid crystal molecules in chiral smectic phase (smectic-C*). In the case of the smectic-C type phase, the molecules have a permanent dipole moment, and the director axis of the molecules is oriented at an angle (say θ) with the layer normal. The permanent dipole moments of the molecules make them interact strongly with the applied electric field. The inclination angle of the director can be changed from θ to $-\theta$ by altering the polarity of a DC electric field applied across the liquid crystal cell, as shown in Fig. 3.6 (i) and (ii). Therefore the molecules are bistable with two stable states based on the polarity of the applied electric field. The light incident with polarization parallel to the molecular dipole experiences a higher refractive index relative to light with perpendicular polarization. The bistability property of the ferroelectric liquid crystal molecules enables the FLCSLM to respond faster to the field variation as compared to the NLCSLM. The typical response time of the FLCSLM cell is of the order of 1 μs, whereas, in the case of NLCSLM cell, it is of the order of 1 ms. The FLCSLM cell is designed in such a way that its thickness along the beam propagation direction introduces a phase difference of π between the extraordinary and ordinary components of the incident beam, such that the cell behaves like a switchable half wave plate.

In this thesis, we use a reflective FLCSLM from FORTH DIMENSION DISPLAY, United Kingdom, (model SXGA - R2). The device has a pixel resolution of SXGA (1280 H $\times$ 1024 V) with a pixel pitch of 13.62 μm spanning over an active area of 17.43 mm $\times$ 13.95 mm. The LC panel of the FLCSLM can display the individual bit planes of an incoming 24 bit image. The manufacturer of the FLCSLM provides a driver board that can be programmed

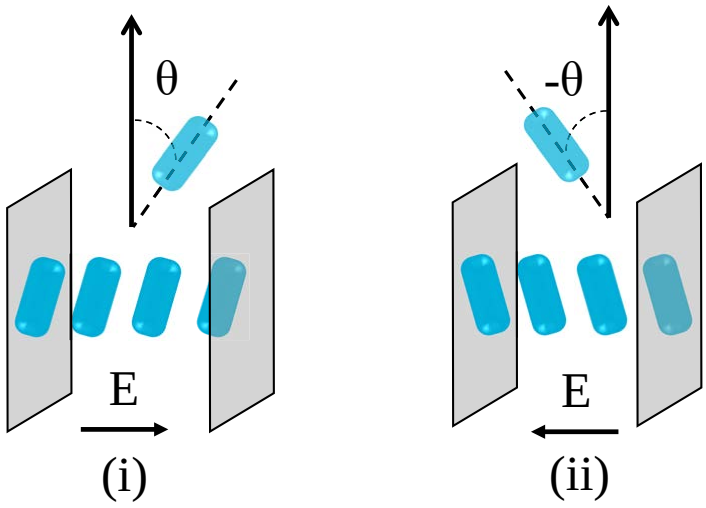

Figure 3.6: Bistability property of ferroelectric liquid crystal molecules in presence of applied DC electric field directed from (i) left to right and (ii) right to left.

with different display addressing sequence files such as 24-bit sequence file and 3-bit sequence file. The sequence file is a piece of code that helps the driver board in deciding the order and duration of display of various bit planes. In the case of the 24-bit sequence file, the FLCSLM sequentially displays each of the 24 constituent bit planes of the 24 bit color image for an equal duration of time, while in the case of the 3-bit sequence file, the FLCSLM displays 3 bit planes representative of each of the three primary colors of the input color image. The device allows a color image refresh rate of 60 Hz via a DVI interface. Thus when the 24-bit sequence file is used, the FLCSLM facilitates the writing of binary holograms at a rate of 1440 Hz [80, 81].

3.3 Beam scanning in scanning optical microscopes

As discussed in the previous chapter, the imaging in a scanning optical microscope is achieved by scanning a diffraction-limited focal spot on the sample plane. Light from each point of the sample plane produces a corresponding image such that light from all the scan positions collectively provides for an electronic image of the sample plane. The scanning means of the illumination beam can be classified into two broad types, namely mechanical and non-mechanical scanning. Mechanical methods include galvanometer based scanning unit [82], piezoelectric actuator [83], micro-electro-mechanical system (MEMS) scanner [84, 85] and so on. Acousto-optic deflector (AOD) [86], electro-optic deflector (EOD) [87], spatial light modulator (SLM) [88], etc. come under the non-mechanical type beam scanning methods. In conventional scanning microscopes, the beam scanning is usually performed by employing a pair of high precession galvanometer based scanning mirrors. The scan mirror is attached to

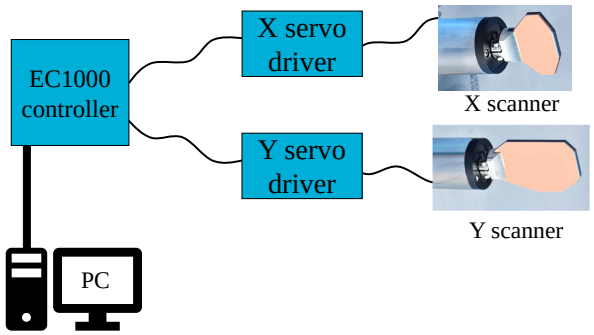

Figure 3.7: Schematic diagram of the configuration of the galvanometer based scanning system comprising the EC1000 control board, two MicroMax 671 servo drivers (one for X positioning and other for Y positioning) and a pair of 6321H scanners.

the motor shaft of a moving magnet galvanometer based actuator. Recently developed laser scanning microscopes are capable of acquiring 512 $\times$ 512 pixels per image at an image frame rate 200 fps (frames per second) [89].

The piezoelectric actuator produces very fine yet precise displacement and is used to adjust lens, mirror, microscope stage, and other components. The MEMS scanner is used for laser beam scanning, and they provide a scanning speed of several tens of kHz. AOD, on the other hand, is a non-mechanical beam scanning technique which uses high frequency sound wave in an acousto-optic medium to form a phase diffraction grating. The beam scanning is performed by changing the angle of the diffracted beam by offsetting the frequency of the sound wave. EODs are made of electro-optic crystals such that they exhibit the Pockels effect. They use a quadrupole electric field to produce a change in the refractive index resulting in a shift in the beam propagation direction. Both AOD and EOD devices can provide high speed laser beam scanning. SLM based beam scanning is another type of non-mechanical beam scanning method. The SLM panel acts as a polarization grating, binary grating or, Fresnel zone plate [90], resulting in the light beam diffracted at a specific angle. Adjusting the spatial frequency of the grating or the zone plate, the diffraction angle of the beam can be changed. In comparison with most of the other scanning methods, galvo mirror based scanning method provides better light efficiency, which is important when the microscope works in the epi-illumination mode.

In this thesis work, we have used both the galvo mirror based beam scanning and LCSLM base holographic beam scanning.

3.3.1 Configuration of Galvanometer based scanning unit

Galvanometer based scanners have become very popular for beam scanning in optical microscopes as they offer flexibility in speed, efficiency, and accuracy. There are three major

components of the galvanometer based scanning unit, namely, the positioning actuator, position detector, and the servo control unit [91]. The galvanometer actuator is the motorized mirror, which works due to the interaction between a magnet and a current carrying coils. The actuator can be configured by three types of magnet and coil combinations, such as moving iron, moving coil, and moving magnet. The most prevalent version is the moving magnet actuator that consists of a static coil and a moving magnet rotor. Such configuration provides the best mechanical resonance, high torque, short response time, and high positioning precision. The angular position of the mirror can be detected by a position sensor, which is a small circuit board located at the back of the scanner. The output signal of this sensor is a differential current signal that is fed back to the servo control unit. The servo control unit compares the current output from the position sensor with the command signal and drives the mirror to its desired position in an attempt to make the error zero.

In this thesis, we incorporate a galvanometer mirror assembly that consists of a Camtech EC1000 controller, a MicroMax Series 671 analog servo driver, and a pair of 6321H galvanometer based scan mirrors. The Fig 3.7 shows the configuration of the EC1000 controller with the Micromax 671 servo driver and 6231H scanner.

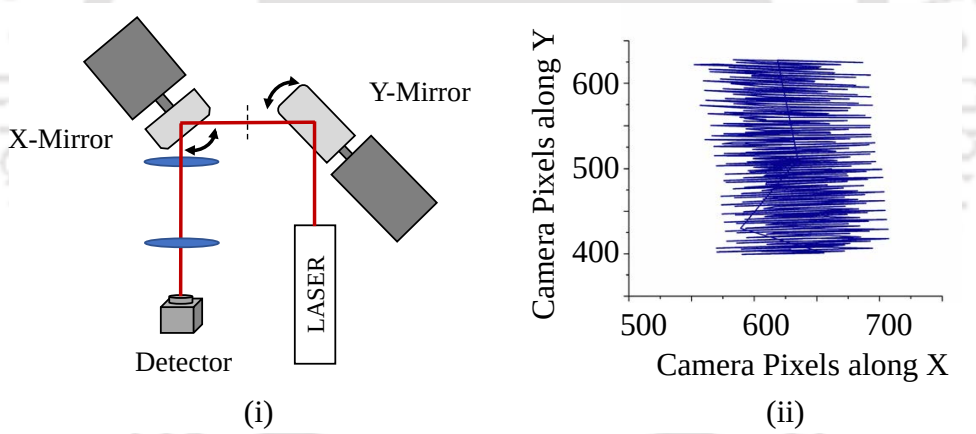

Figure 3.8: (i) A simple arrangement of the two scan mirrors with two scan mirrors placed close to each other, and (ii) the resulting beam movement at the detector plane.

The EC1000 is a standalone control board that provides advanced hardware and software control to drive the laser scanning system. It provides a 16-bit galvanometer position command resolution via a TCP/IP communication over an ethernet cable. The MicroMax Series 671 analog servo driver has a class 1 configuration, which uses integrated position error to settle to the highest level of positioning accuracy with the least angular error [92]. The 6231H is a moving-magnet actuator with a high torque constant and 8 μradians repeatability. The position detector has a linearity of 99.9% and a zero drift of 15 μradians/°C [93]. For scanning a specific area of the sample, scan-commands are sent to the EC1000 controller for appropriate

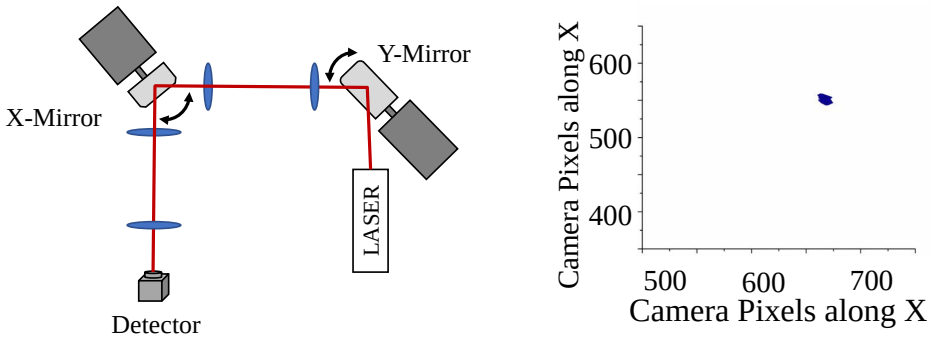

(i) (ii)

Figure 3.9: (i) Incorporation of a $4f$ relay between the two mirror, and corresponding (ii) beam movement at the detector plane.

movement of the scan mirrors. However, to have better control over the movement and stability of the scan mirrors, we also utilize the analog voltage outputs available from a PCI expression card. The card provides two voltage outputs synchronized with an external clock, which can be directly connected to the two servo drivers. We have developed a LabVIEW based program to send the scan-commands to the controller via an Ethernet communication protocol or directly to the two servo drivers.

Positioning of the two scan mirrors

It is to be noted that for the best imaging performance of a scanning microscope, the entrance pupil plane of the objective lens is to made conjugate with the scan mirrors. In the absence of this requirement, there will be a transverse movement of the beam at the entrance pupil as the illumination beam is scanned. The simplest way to achieve this approximately is to position the two mirror heads close to each other. The entrance pupil plane of the objective lens is made conjugate to a plane mid way between the two scan heads. However, even in such a case, there exists some transverse movement of the scanned beam at the entrance pupil. To demonstrate the same, we perform an experiment where the two scan heads are kept very close to each other, and a CMOS camera is placed conjugate to the mid way between the two scan heads, using $4f$ relay lenses, as shown in Fig. 3.8 (i). A laser beam is incident on the Y-mirror followed by the X-mirror and then on the camera. The camera thus records the fluctuations of the beam in the conjugate plane as the two mirrors oscillate. Figure. 3.8 (ii) shows the fluctuations of the laser beam, which should not be present for the best imaging performance in a scanning optical microscope.

We have then placed another $4f$ relay between the two scan heads and made both the X-mirror and Y-mirror optically conjugate with the camera plane as shown in Fig.3.9 (i). The

fluctuation of the laser beam at the camera plane, as the mirrors oscillate, is shown in Fig. 3.9 (ii). It is thus seen that the introduction of a $4f$ relay lens between the two mirrors provides better beam stability at the conjugate plane, which in the case of a scanning microscope can be the entrance pupil of the objective lens.

3.3.2 Holographic beam scanning

As we have discussed in the previous section that the binary hologram constructed numerically and displayed using a programmable LCSLM can realize a user defined illumination beam. Since LCSLMs facilitate real time reconfigurability of the displayed patterns, binary holograms written on LCSLMs can also achieve beam scanning. Beam scanning by implementing the CGH technique was in fact introduced in 1976 [94]. Binary holograms written on LCSLM have been found to be providing very accurate beam positioning and steering [95, 96]. In this thesis, we also employ binary holographic beam scanning using the LCSLM to scan a rectangular area over the sample plane [97]. The CGH technique facilitates not only scanning over a rectangular area of the sample but also describing the wavefront of the illumination beam. If the illumination beam contains aberrations induced by the sample or by the beamforming optics, the same can be removed by incorporating an appropriate correction phase expressed as a linear combination of Zernike modes.

From the section 3.2.2, we see that the overall phase of the illumination beam $\Phi(x,y)$ contains the tilt $\tau(x,y) = m_x x + m_y y$ responsible for the deflection angle of the beam and the phase term $\phi(x,y)$, which can represent the linear combination of Zernike modes to be incorporated as the correction phase. Therefore by writing a sequence of holograms onto the LCSLM with a precise variation of the tilt function $\tau(x,y)$, the illumination beam can be moved to as many scan positions, each depending on the values of (m_x, m_y), as the number of binary holograms displayed.

For scanning the sample plane in an optical microscope, the entrance pupil of the objective lens is to be made conjugate with the LCSLM plane. By employing the binary holographic scanning based on the LCSLM, we achieve high accuracy beam steering at the cost of the scanning speed relative to the galvanometer based scanning unit. By using the FLCSLM with the 24-bit sequence file and 85Hz video rate, the beam scanning speed can be increased up to more than 2000 scan positions per second. The same speed using the NLCSLM is around 60 scan positions per second.

3.4 Experimental implementation of the microscope

In order to set up the scanning optical microscope assembly, several major components are needed, such as laser, beam forming optics, beam scanning unit, detector, data acquisition card, sample stage, objective lens, and so on. Below we briefly describe the primary components used in our microscope assembly, inclusive of the components developed in-house.

3.4.1 The laser

Modern scanning optical microscopes use the laser as the illumination source as it emits an extremely bright, coherent, highly collimated, and monochromatic light beam. Additionally, the laser chosen in a scanning optical microscope should have a good spatial mode profile, a narrow spectral bandwidth, and good power stability. The TEM_{00} mode of laser, which has a quasi-planar wavefront with a Gaussian intensity profile perpendicular to the direction of propagation of the beam and minimum beam divergence, is ideal for this purpose.

The specifications of the lasers used in this thesis are given in table 3.1.

Manufacturer	Melles Griot	Spectra-Physics
Model no.	05-LHR-991	Excelsior-532-200-CDRH
Technology	He-Ne	DPSS
Wavelength	632.8 *nm*	532 *nm*
Spatial mode	$> 90\%$ TEM_{00}	TEM_{00}
CW output power	> 10 *mW*	200 *mW*
Beam quality (M^2)	<1.05	<1.1
Beam diameter at $\frac{1}{e^2}$ points	0.65 *mm* $\pm$ 5%	0.32 $\pm$ 0.02 *mm*
Beam divergence	1.24 *mrad* $\pm$ 5%	<2.5 *mrad*

Table 3.1: Specification of the lasers used.

3.4.2 Microscope objective

Microscope objective is one of the most important components of the microscope assembly in determining the quality of images that the microscope is capable of producing. It is a complex multi-lens assembly that focuses light to a narrow spot on the sample plane. The same lens also collects the reflected or emitted light from the object, for microscopes working in the epi-illumination mode. The multi-lens assembly constituting the objective is designed using high precision computer aided design (CAD) tools and advanced rare element glass formulations of uniform composition and quality having highly specific refractive indices, to minimize the aberrations present in the illumination spot. Modern microscope objectives are corrected for most of the common aberrations such as coma, astigmatism, field curvature, spherical and chromatic aberration.

Manufacturer Model no.	Magnif--ication	Working distance	*NA*	Immersion media	Correction level
UPLFLN 10X2	10 ×	10 *mm*	0.3	Air/Dry	Semi- apochromat
PLN 20X	20 ×	1.2 *mm*	0.4	Air/Dry	Achromat
LUCPLFLN 40X	40 ×	2.7-4 *mm*	0.6	Air/Dry	Semi- apochromat
UPLSAPO 60XW	60 ×	0.28 *mm*	1.2	Water	Super- apochromat
UPLSAPO 100XO	100 ×	0.13 *mm*	1.4	Oil	Super- apochromat

Table 3.2: Specification of the objective lenses.

The most common objectives are the achromatic objectives, corrected for chromatic aberration at red and blue colors, and the spherical aberration at the green. Plan achromat objectives are corrected for the same aberrations as the achromatic objectives and also for field curvature. Fluorite objectives are corrected for chromatic aberrations at red and blue and for the spherical aberration at 2 or 3 colors. They have a higher *NA* than achromats. The next type of objective, called apochromatic objective, has the highest level of correction for chromatic and spherical aberrations. Apochromats are usually corrected for chromatic aberration at 3-4 colors and for the spherical aberration at 2-3 colors. Super apochromatic objectives have the same chromatic and spherical aberration corrections as in apochromats with a higher transmission for the

range visible to near-infrared [98]. The specifications of the objective lenses used to perform experiments in this thesis are given in table 3.2.

3.4.3 Array detection Unit

The proposed scanning optical microscope in this thesis uses array detectors. The array detectors can either be a charge coupled device (CCD) or a complementary metal oxide semiconductor (CMOS) device.

Manufacturer Model no.	Basler A631f	Basler A504k	FLIR GS3-U3-23S6M	Hamamatsu C11440-22C
Sensor type	CCD	CMOS	CMOS	SCMOS
Resolution	1392×1040	1280×1024	1920×1200	2048×2048
Pixel size	4.65 μm	12 μm	5.86 μm	6.5 μm
Frame rate	18 fps	500 fps	163 fps	100 fps
Interface	IEEE 1394 bus	Camera Link	USB 3.1	Camera link

Table 3.3: Specification of array detectors.

Both CCD and CMOS are semiconductor devices capable of converting the incident light falling on an array of pixels into electrons but with different readout processes of electrons. In the case of CCD, electrons from all the pixels are read row by row in a sequential manner followed by an amplification. In contrast, in CMOS, the embedded electronics in each pixel allows amplification and digitalization on a pixel to pixel basis, which enables faster readout than that of CCD. As the pixel in the CMOS sensor contains the readout electronics, the sensor area is smaller than the pixel area, while in CCD, the sensor area is larger. Thus one can choose the CCD for high spatial resolution applications and the CMOS for high speed acquisitions. The typical QE of the CCD and CMOS sensor is about 40-50%. In the case of electron multiplied CCD (EMCCD) and scientific CMOS (SCMOS), the QE can be as high as 80%.

The specification of the array detectors used in this thesis [99–102] are given in table 3.3 .

3.4.4 Synchronization unit

For image acquisition in the scanning microscope, all the major components, such as the galvanometer based scan unit, LCSLM assembly, and detection unit, work in a synchronized manner. To facilitate the same, in this work, we develop a synchronization unit using a peripheral interface controller (PIC) based circuit board, which communicates with various units to realize synchronized operation.

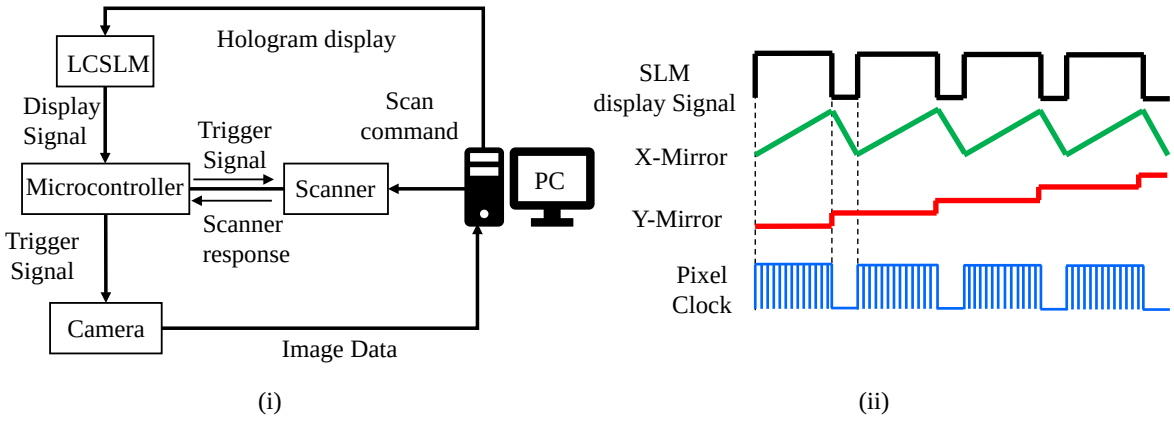

Figure 3.10: The schematic representation of the (i) synchronization unit and (ii) synchronized signals obtained from the PIC micro controller using the display signal of the SLM for the galvanometer based scanner unit.

We employ a PIC18F2550 microcontroller manufactured by Microchip, which has 28 input/output pins that perform various functions. Both the NLCSLM and the FLCSLM provide TTL signals, which indicate the display timings of binary hologram sequences sent to the respective LCSLM. Such a TTL signal from the LCSLM is fed to the microcontroller board as an external interrupt input. The microcontroller is instructed to produce synchronization signals to trigger the scanning unit and the detection unit accordingly. The schematic diagram of the synchronization unit, along with all components, is shown in 3.10 (i). Figure 3.10 (ii) shows a schematic of the command inputs for the X and Y scanners along with TTL signals from the LCSLM and trigger signals for the detector in one specific configuration of the experimental setup.

3.4.5 Beam scanning optical microscope

Here we describe a proof-of-principle scanning optical microscope arrangement, as shown in Fig. 3.11 that can use either the galvo mirror based or the holographic scanning unit. A laser beam is expanded and collimated using two lenses L_1 and L_2, and the collimated laser beam is

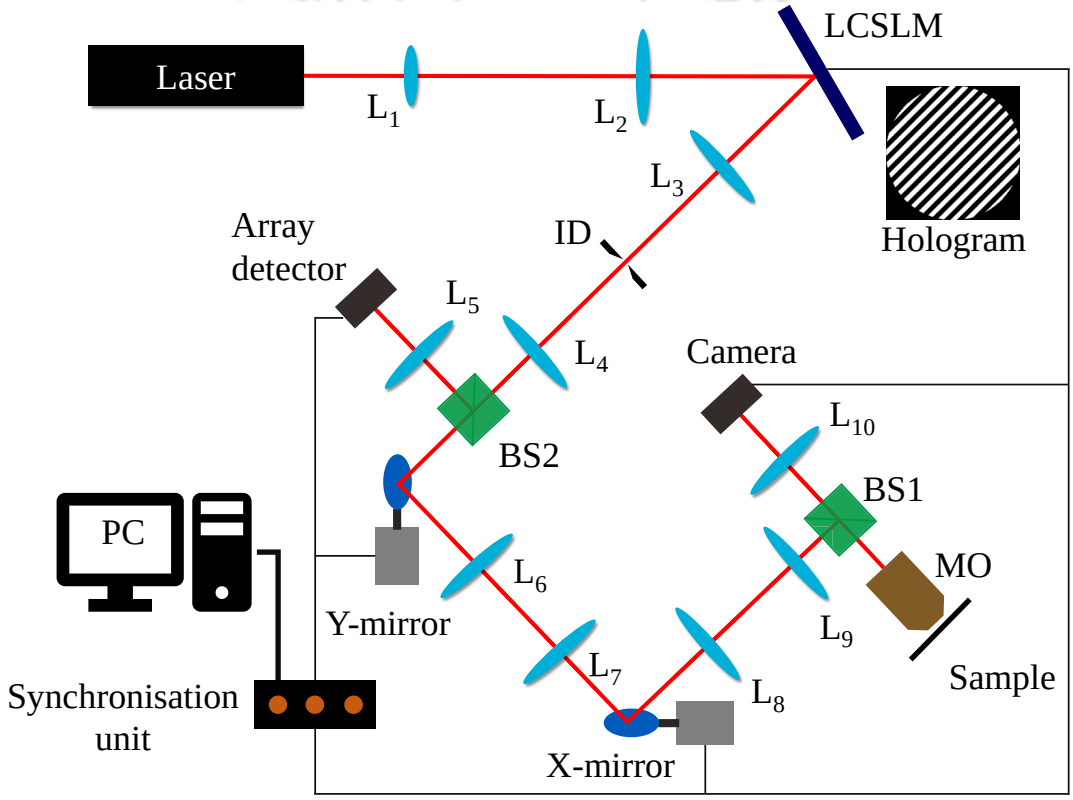

Figure 3.11: Schematic of a typical experimental setup of the array detection microscope.

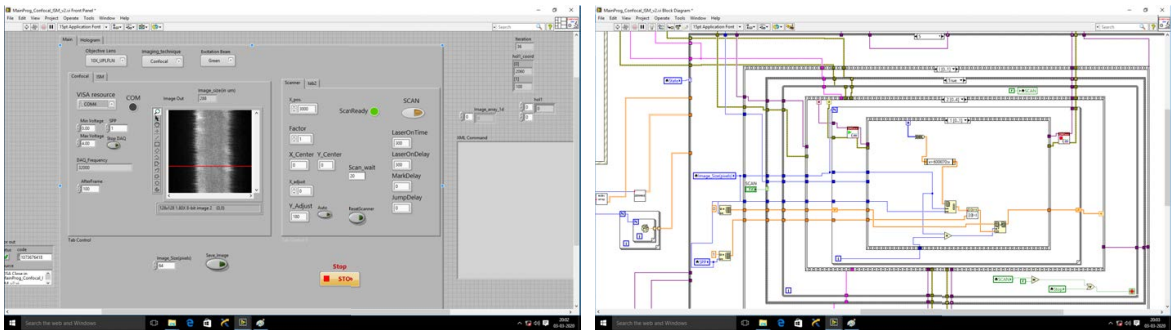

(i) (ii)

Figure 3.12: Snapshot of (i) front panel and (ii) block diagram of the LabVIEW programming interface.

allowed to incident on the LCSLM. Binary holograms computed using a LabVIEW program on a computer are sent to the LCSLM display panel. The LabVIEW program has a graphical user interface (GUI) for controlling the active components constituting the microscope assembly. A snapshot of the front panel and the block diagram of the LabVIEW program is shown in Fig. 3.12 (i) and (ii), respectively. The diffracted beams from the LCSLM are focused by a lens L_3, and the $+1$ order beam is isolated by an iris diaphragm (ID). The $+1$ order beam then travels towards the beam scanning unit comprising X and Y scan mirrors.

The combinations of lenses L_3-L_4, L_6- L_7, and L_8-L_9 form three 4f relay systems to render the hologram plane conjugate with the back focal plane of the objective lens. The arrangement thus ensures that as the X-Y mirrors rotate, the focused beam describes a rectangular area on the sample plane. A part of the reflected or emitted light from the sample is transmitted by the beam splitter BS1 to retrace its path through the scanning unit. It is then reflected by BS2 and focused onto the camera using the lens L_5. As the mirror scan, the detector arrays are stored in the PC to later construct an electronic image of the sample at the end of the scanning process. In the above the arrangement the +1 order diffracted beam has a fixed orientation. In order to activate the holographic scanning, the two scan mirrors are kept at a fixed orientation, while the LCSLM displays a sequence of binary holograms, each with a different orientation of the +1 order beam. A part of the light from the sample is reflected by BS1 to be focused onto the camera using the lens L_{10} to constitute the detection part for this arrangement. For each position of the illumination beam on the sample plane, there is a corresponding image of the illumination beam on the camera plane. A programmably selected rectangular area on the camera around the illumination spot acts as the detector window. The detector window moves as the beam starts scanning the signal-to-noise. The net signal from the detector windows is stored in the PC to render the final image.

The above two configurations of the scanning optical microscope are presented as examples only. Scanning optical microscope can also be built with any one of the scanning schemes. In fact, in the later chapters, we will implement slightly different designs of the microscope setup.

3.5 Summary

In this chapter, we have discussed the basic principle of classical holography and computer generated holography. We have discussed how binary holograms can generate a beam with user defined phase profile. Properties of liquid crystal spatial light modulator and how they can implement binary hologram have been elaborated. Light beams whose phase profiles are designed using binary holograms can be used as the illumination beam of scanning optical microscopes. We have then discussed implementing a proof-of-principle scanning optical microscope that uses the galvanometer based or holographic beam scanning scheme.

CHAPTER 4

Estimation of the point spread function

4.1 Introduction

The point spread function (PSF) of an imaging system, also referred to as the imaging PSF in this thesis, is the most essential parameter to describe the resolution of the system. This parameter is helpful while employing several post-acquisition image processing techniques. In this chapter, we propose a PSF estimation scheme to estimate the imaging PSF of an imaging system, which is applicable irrespective of the imaging geometry of the system. The chapter begins with a stepwise description of the proposed scheme, along with a flowchart diagram. We first implement the proposed scheme on a one dimensional (1D) numerically constructed target and then on a two dimensional (2D) numerically constructed target. We then experimentally demonstrate the proposed scheme in a widefield microscope and then in a point scanning microscope.

4.2 The proposed scheme

To understand the proposed scheme, we consider an incoherent imaging system which has $p(u,v)$ as its PSF. Thus the intensity distribution in the image plane due to an object, with $t(u,v)$ as the intensity distribution in the object plane, is expressed as the convolution of $t(u,v)$ and the PSF [13]. Therefore we can write $I_i(u,v) = k\, p(u,v) \otimes t(u,v)$, where $\otimes$ represents the convolution operator, k is a constant and (u,v) represent the coordinates of both the object and image planes assuming unit magnification. Employing Fourier transform on both sides and ignoring the constant k, we can write the equation as

$$I_i(u,v) = \mathscr{F}^{-1}[\mathscr{F}\{p(u,v)\} \times \mathscr{F}\{t(u,v)\}] \tag{4.1}$$

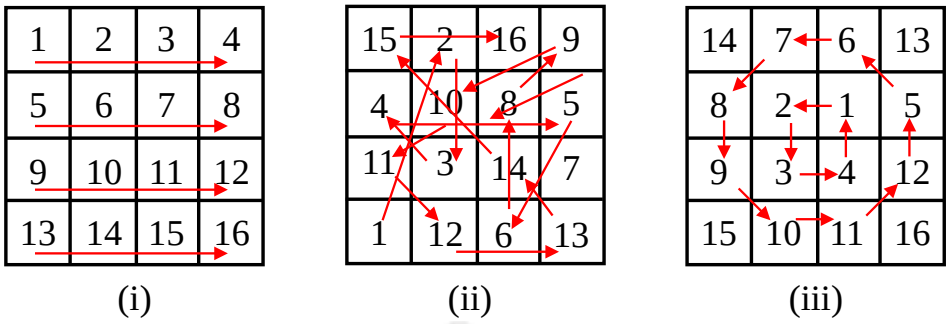

Figure 4.1: Schematic diagrams of the (i) raster, (ii) random and (iii) spiral pixel selection sequences.

In the above $\mathscr{F}$ and $\mathscr{F}^{-1}$ represent the two dimensional Fourier transform and inverse Fourier transform, respectively. Our PSF estimation scheme is based on stochastic minimization of least square errors. The prerequisite of our scheme is a target either with known geometrical-optics prediction of the image (denoted as I_{gop}) formed by the imaging system or the same that can be numerically constructed from the acquired image. In our experiment we in fact take a standard resolution test chart (USAF 1951 Resolution target, manufactured by Thorlabs) as the target [103–105]. The estimation process starts with a Dirac delta function as the initial (i.e., guess) PSF, defined as an array of zeros with a central pixel of value one. The scheme then searches for the realistic PSF by stochastically modifying each pixel of the PSF array sequentially. We introduce an error function, which is defined by the least square error between the image of the target by the imaging system and the convolution of I_{gop} with the modified PSF array. The error function can be expressed as

$$\sum \varepsilon_p^2 = \sum \left(t_i(u,v) - t_p(u,v)\right)^2 \tag{4.2}$$

where $t_i(u,v)$ is the image of the target formed by the microscope or, the imaging system and $t_p(u,v)$ is the image formed via convolution of the PSF p and the I_{gop} of the target (i.e. $t(u,v)$). Modification of the pixel value is retained only if the PSF array with the modified pixel value reduces the magnitude of the error function. Such modification of the pixel values continues until all the pixels in the PSF array are considered, thereby completing the first iteration process. The final estimated imaging PSF of the imaging system is defined as the PSF array after a number of iterations sufficient to lower the value of $\sum \varepsilon_p^2$ below a predetermined threshold. In a given iteration, the pixels of the PSF array can be selected in different sequences, such as raster, random, spiral selection of pixels. In the raster selection of pixels, the pixels are chosen horizontally from left to right and then top to bottom, as shown in Fig. 4.1(i). In random selection, the pixels are chosen in a random sequence and in the spiral selection, as shown in

Fig. 4.1(ii), the pixels are selected spirally outwards starting from the center of the PSF array, as shown in Fig. 4.1(iii).

The step by step process of estimating the imaging PSF array using our proposed scheme is described below.

1. Take the image $t_i(u,v)$ formed from the microscope or the imaging system and normalize it using $t_i = \frac{t_i - Min(t_i)}{Max(t_i) - Min(t_i)}$.
2. Define the guess PSF array p as a Dirac delta function.
3. Obtain the image $t_p(u,v)$ by taking convolution of the PSF p and the I_{gop} of the target $t(u,v)$.
4. Compute the least square error using equation. 4.2.
5. Select a pixel of p at the location (u,v) using one of the pixel selection sequences such as spiral selection as depicted in Fig. 4.1. Replace $p(u,v)$ by a uniform random number between 0 and 1. Obtain a new least square error $\sum \varepsilon_p^{2'}$ using steps (3) and (4).
6. If $\sum \varepsilon_p^{2'} \not< \sum \varepsilon_p^2$, the pixel value of p at (u,v) is replaced by its previous value, however if $\sum \varepsilon_p^{2'} < \varepsilon_p^2$, the new pixel value of p is retained and $\sum \varepsilon_p^2$ is replaced by $\sum \varepsilon_p^{2'}$.
7. Steps (5) and (6) are repeated till all the pixels of p are covered following the given pixel selection sequence.
8. Steps (5), (6) and (7) are repeated over a number of iterations till $\sum \varepsilon_p^2$ minimizes to an acceptable level. The p at the end of the required number of iterations is taken as the estimated imaging PSF of the imaging system.

The PSF estimation steps above are also illustrated in a flowchart in Fig. 4.2. The final estimated imaging PSF array can be Fourier filtered to remove the unwanted high spatial frequency contents. In the above, we mentioned three pixel selection sequences. We have observed that, in the spiral pixel selection sequence, the least square error ($\sum \varepsilon_p^2$) converges faster as compared to the other two sequences. In all the pixel selection sequences, the value of $\sum \varepsilon_p^2$ drops rapidly during the first few iterations, as seen in Fig. 4.3. However, since the spiral pixel selection sequence gives more priority to the pixels closer to the Dirac delta function (i.e., the guess PSF), the corresponding $\sum \varepsilon_p^2$ reaches the minimum after the least number of iterations. Therefore in this work, we adopt the spiral pixel selection sequence to estimate the imaging PSF array.

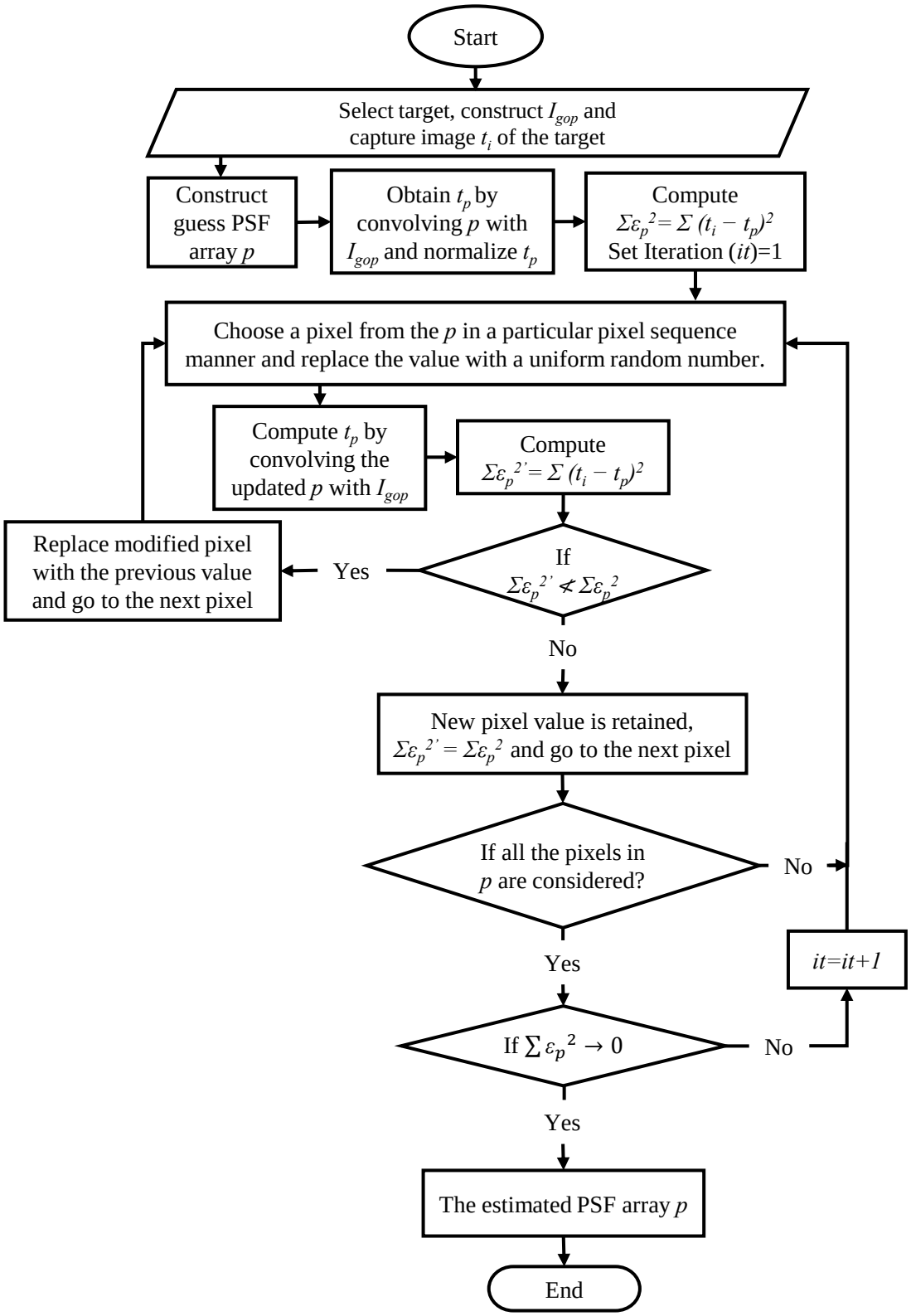

Figure 4.2: Flowchart of the proposed PSF estimation scheme.

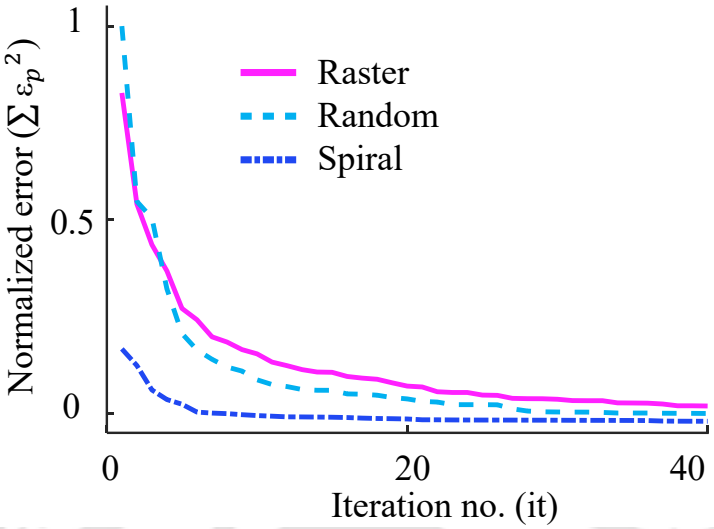

Figure 4.3: Plot of normalized error ($\sum \varepsilon_p^2$) and the iteration number (it) illustrating the convergence of three pixel selection sequences.

4.3 Numerical implementation

In order to demonstrate the correctness of our proposed PSF estimation scheme we first validate the scheme numerically on a one dimensional (1D) target and a two dimensional (2D) target.

4.3.1 One dimensional object

We numerically construct a 1D target defined over 256 pixels, as shown in Fig. 4.4(i). The target is convolved with two PSFs, referred to as PSF_1 and PSF_2, where PSF_1 has a full width at half maximum (FWHM) of 14 pixels and PSF_2 has a FWHM of 10 pixels. The plots of the convolved target are also seen in Fig. 4.4(i). We then transform the convolved target to a binary function by using the threshold value of 0.5, which is taken as the I_{gop} of the target. We obtain the power spectra of both the target and the constructed I_{gop} and the precise overlap between the two spectra, as seen in Fig. 4.4(ii), establishes the correctness of the I_{gop} thus constructed. We then employ the proposed scheme on the convolved targets to estimate the respective imaging PSFs using 900 iterations. To validate the proposed PSF estimation scheme, we have taken the root mean square error (RMSE) of both the PSF1 and PSF2 with their respective estimated PSFs. The RMSE is found to be 0.004 and 0.003 for PSF1 and PSF2, respectively. Plots of the two PSFs employed and the corresponding estimated imaging PSFs, as seen in Figs. 4.4(iii) and (iv), demonstrate that the proposed PSF estimation scheme works well for 1D targets.

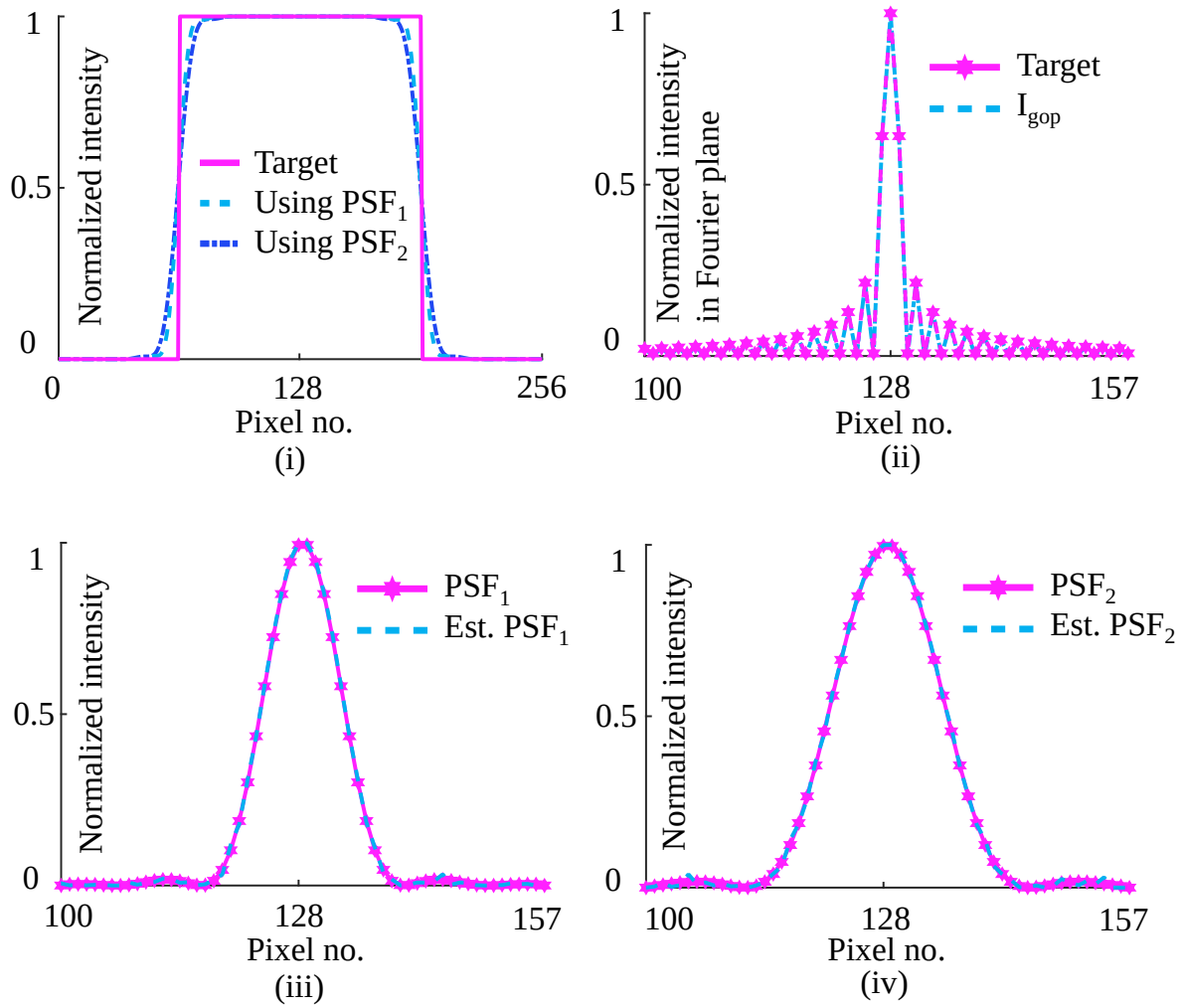

Figure 4.4: Normalized intensity plot of (i) one dimensional target and convolution of the target with PSF_1 and PSF_2. (ii) The power spectra of the target and the constructed I_{gop}. (iii) PSF_1 with the estimated imaging PSF, and (iv) PSF_2 with the estimated imaging PSF.

We further observe that the accuracy in the estimated PSFs is dependent on the number of iterations over which the proposed scheme is employed, and the estimated imaging PSF matches more and more with the applied PSF as the iteration number increases.

4.3.2 Two dimensional object

We then employ the proposed scheme on 2D targets to estimate the respective imaging PSF arrays. We consider two types of 2D objects, one complex object, as seen in Fig. 4.5(i) and one simple object comprising binary pixel values as seen in Fig. 4.5(ii). A numerically obtained

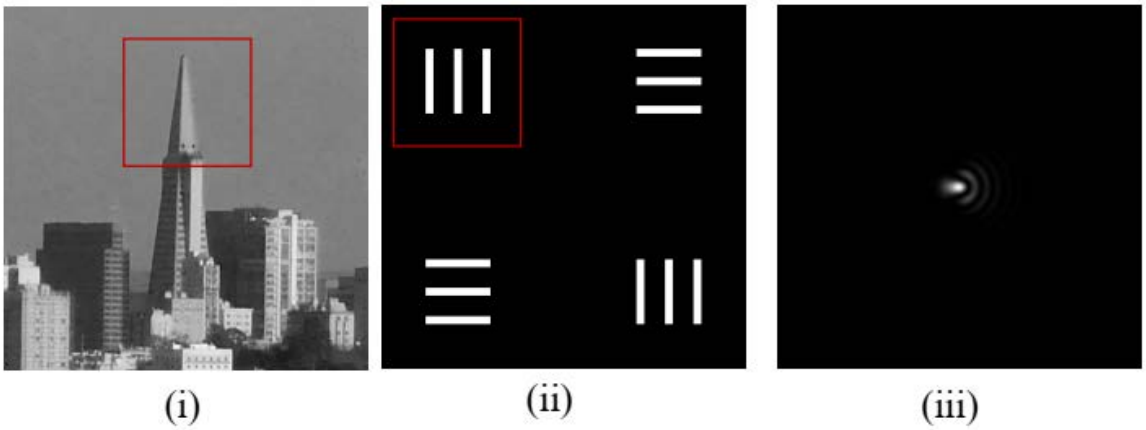

Figure 4.5: (i) A complex object and (ii) a simple object, each described over 512 × 512 pixels. (iii) Numerically obtained PSF used to form the convolved images.

PSF, as seen in Fig. 4.5(iii), is convolved with both the targets to produce the corresponding convolved images, seen in Figs. 4.6(i) and (ii).

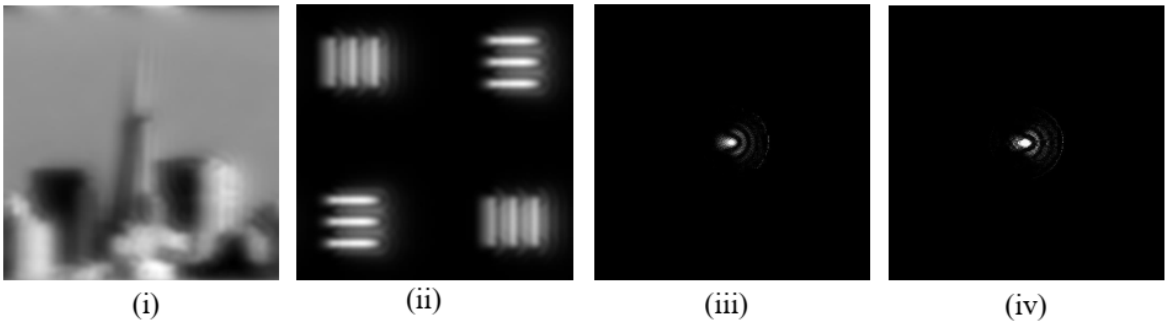

Figure 4.6: Convolved images (i) and (ii) of the targets seen in Figs. 4.5 (i) and (ii), respectively. (iii) and (iv) are the imaging PSF arrays estimated from the convolved images (i) and (ii) respectively. Here we used 100 iterations for estimating the imaging PSF for both the objects.

Construction of I_{gop}

A simple target can be a lithographically fabricated binary target, such as the object in Fig. 4.5 (ii). The corresponding I_{gop} can be constructed by thresholding its electron microscope image. In the absence of the electron microscope image of the target, the I_{gop} can be constructed by thresholding the best available image of the target. We have noticed in the case of the one dimensional target that a thresholded image can be a very precise representation of the I_{gop}. However, in the case of a complex target, the construction of the I_{gop} will be a challenge.

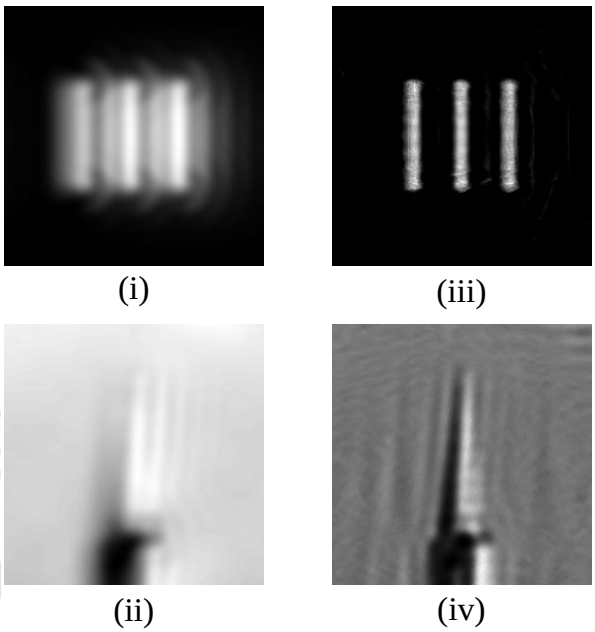

Figure 4.7: (iii) The reconstructed images corresponding to deconvolution between the image in (i) and the PSF in Fig. 4.6 (iii). (iv) The reconstructed images corresponding to deconvolution between the image in (ii) and the PSF in Fig. 4.6 (iii). The image deconvolution used Richardson-Lucy algorithm over 70 number of iterations.

Here, we consider the objects seen in Fig. 4.5 (i) and (ii) as the I_{gop}. The imaging PSF estimated from the image in Fig. 4.6(i) and (ii) are seen in Fig. 4.6(iii) and (iv) respectively. We notice that the imaging PSF estimated using the complex object provides a better resemblance with the applied PSF than using the simple object.

Deconvolution using the estimated imaging PSF

We take the estimated imaging PSF corresponding to the simple object, whose I_{gop} can be constructed easily relative to the complex object to deconvolve both the images in Figs. 4.6 (i) and (ii). Figures 4.7 (i) and (ii) show the magnified portions of Fig. 4.6 (i) and (ii) enclosed by solid red boxes as seen in Fig. 4.5 (i) and (ii). The corresponding reconstructed images after Richardson-Lucy deconvolution seen in Figs. 4.7 (iii) and (iv) demonstrate that the use of the estimated imaging PSF from the simple object not only removes blur from the image of the simple object but also from the image of the complex object. Therefore, the imaging PSF estimated from the simple object can also represent the imaging PSF for the complex object, provided both the objects are imaged with the same illumination PSF.

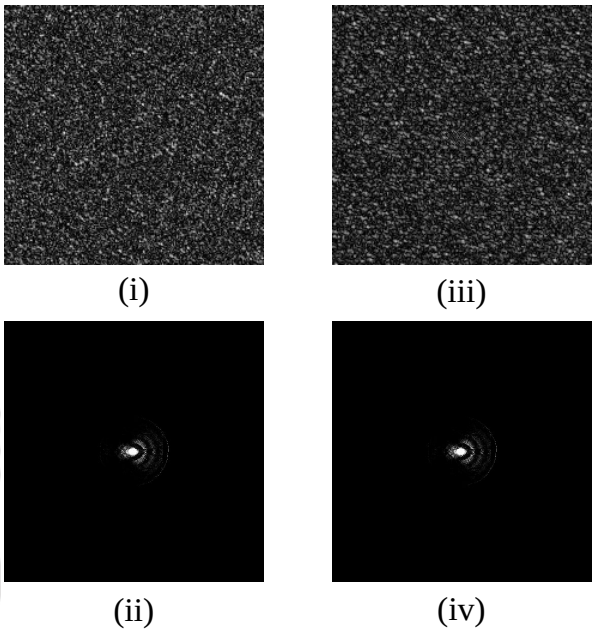

Figure 4.8: (i) and (iii) The estimated imaging PSFs in presence of Poisson noise with PSNR = 33 dB and 55 dB respectively. (ii) and (iv) The estimated imaging PSFs using our proposed PSF estimation scheme in presence of Poisson noise with PSNR = 33 dB and 55 dB respectively.

PSF estimation method	Pseudo inverse filter	Proposed PSF estimation method
RMSE	4.0384	2.5637
RMSE	4.0394	2.5905

Table 4.1: Root mean square error of PSFs obtained by pseudo-inverse filter and our proposed scheme with respect to the applied PSF.

Performance in the presence of noise

We then assess the performance of our PSF estimation scheme in the presence of noise. We add Poisson noise to the image in Fig. 4.6(ii) so that the peak signal-to-noise ratio (PSNR) drops to 55 dB and 33 dB. We first estimate the imaging PSF using the pseudo-inverse filter [106] on the noisy image. Figures 4.8(i) and(iii) show that the pseudo-inverse filter fails to estimate the imaging PSFs in the presence of the Poisson noises equivalent to PSNR 33 dB and 55 dB, respectively. However, our proposed scheme estimate the imaging PSFs in both cases of PSNR 33 dB and 55 dB, with the same accuracy as in the noiseless case, as seen in Figs.

4.8 (ii) and (iv), respectively. We have also calculated the RMSE of the PSFs obtained by both pseudo-inverse filter and our proposed PSF estimation method and is given in table 4.1. From the table 4.1, it is clear that the PSF estimation scheme performs well than pseudo-inverse filter technique to estimate the PSF.

4.4 Experimental implementation

After the validating the correctness of the proposed scheme on numerically constructed targets, we then demonstrate the proposed PSF estimation scheme on experimental images obtained from a widefield microscope and a laser scanning confocal microscope.

4.4.1 Widefield microscope

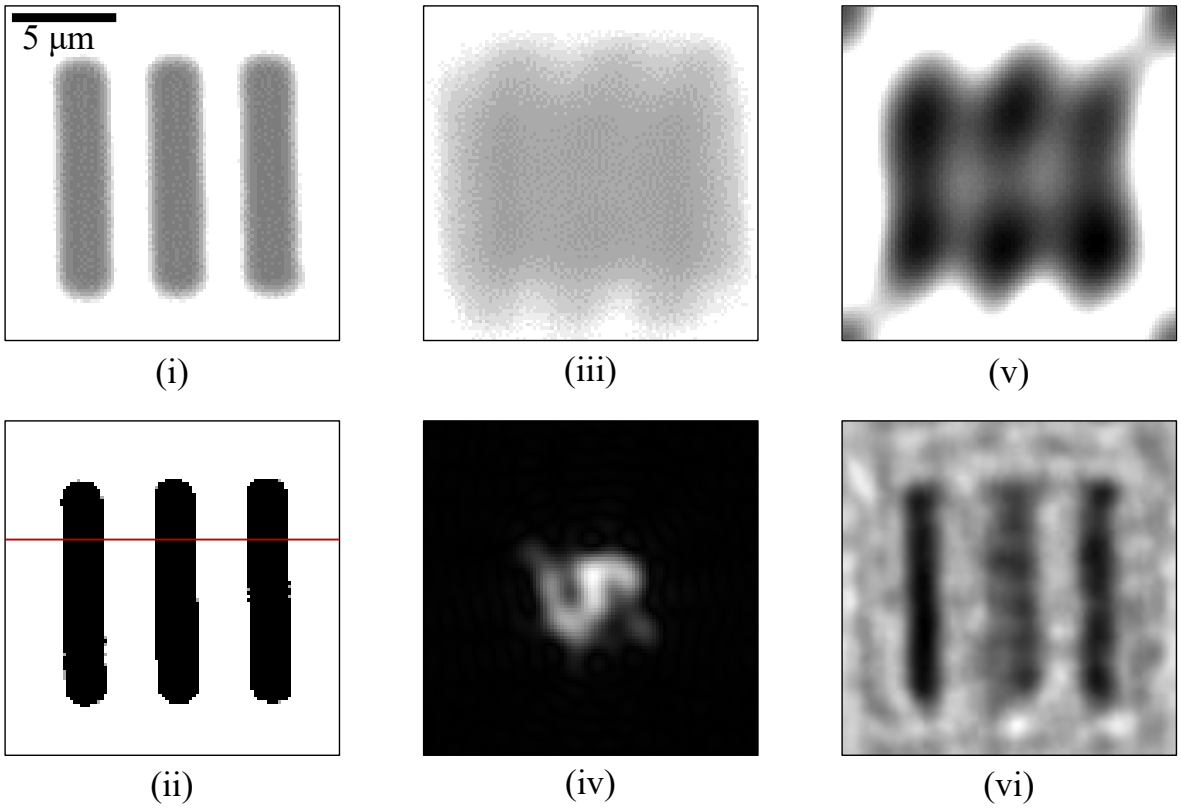

Figure 4.9: (i) Widefield image of a portion of USAF 1951 resolution test target, (ii) constructed I_{gop}, (iii) defocused image after 15 μm axial movement, (iv) estimated imaging PSF using our proposed scheme, (v) restored image using blind deconvolution over 70 iterations, (vi) restored image after Richardson-Lucy deconvolution over 70 iterations using the estimated imaging PSF.

Here we use an inverted microscope (IX51 manufactured by Olympus) for acquiring widefield images of the USAF resolution target. We image a portion of the USAF test target with a 40 $\times$ objective lens (NA=0.6). An incoherent broadband source with a peak wavelength of about 540 nm illuminates the target. A well focused image of the USAF target comprising 98 $\times$ 98 pixels over an area of 16 μm $\times$ 16 μm acquired by the widefield microscope is shown in Fig. 4.9(i). We threshold the normalized image using a threshold value of 0.5 to construct the I_{gop}, seen in Fig. 4.9(ii). We then move the microscope stage axially by about 15 μm using a piezo-electric stage to defocus the imaging system, and the defocused image of the target is shown in Fig. 4.9(iii). The imaging PSF is estimated from the defocused image using our

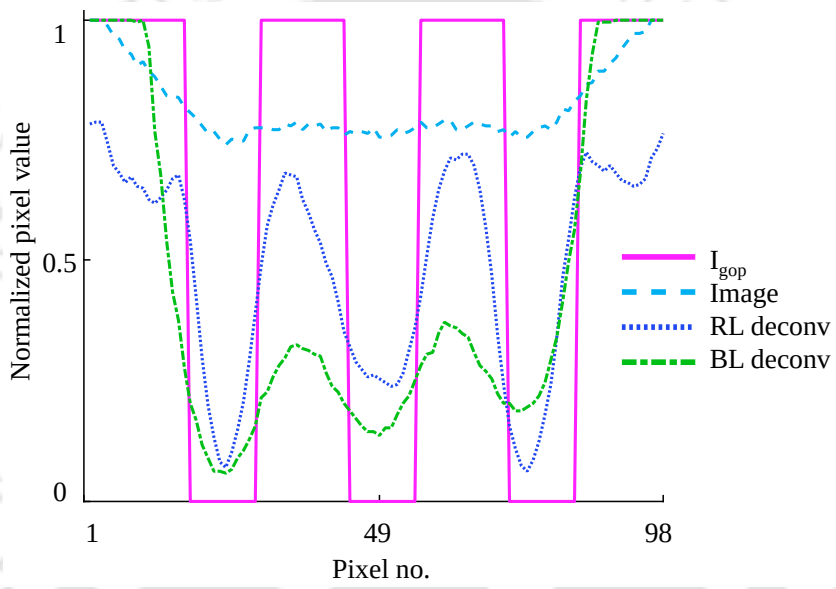

Figure 4.10: Line plots along the red solid line shown in Fig. 4.9(ii) for the images in Fig. 4.9(i), (ii), (iii), (v) and (vi).

proposed scheme over 60 iterations, and the estimated imaging PSF is seen in Fig. 4.9(iv). We then perform deconvolution on the defocused image to restore the original image. We use the estimated imaging PSF, as in Fig. 4.9(iv), in the Richardson-Lucy deconvolution of the defocused image, and the reconstructed image after 70 iterations is shown in Fig. 4.9(vi). We also employ blind deconvolution on the same defocused image over the same number of iterations, and the reconstructed image thus obtained is shown in Fig. 4.9(v). For easy comparison of the reconstructed images obtained from different deconvolution algorithms, we take line plots along the solid red line in Fig. 4.9(ii), for the I_{gop}, the experimental image, and the respective deconvolved images. The plot in Fig. 4.10 clearly shows the superior restoration of contrast in the deconvolved image using the estimated imaging PSF.

4.4.2 Laser scanning confocal microscope

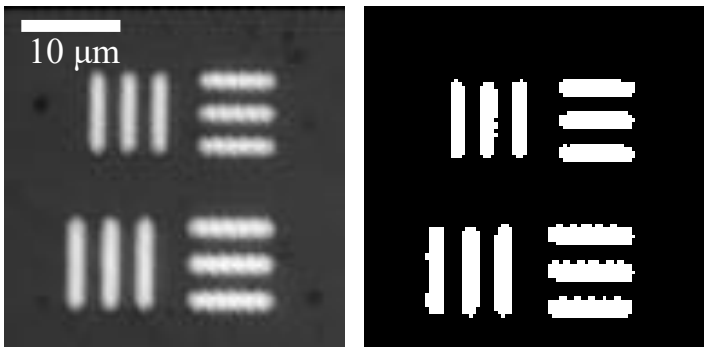

Figure 4.11: (i) Experimental confocal image of a USAF target comprising 94×94 pixels over an area of 35 μm × 35 μm,(ii) the constructed I_{gop}.

We then demonstrate the proposed PSF estimation scheme in a laser scanning confocal microscope. The confocal microscope is based on a holographic beam scanning unit as described in chapter 3 and thus be referred to as the holographic scanning confocal microscope [97, 107]. We image a portion of the USAF test target having an area of about 40 μm × 40 μm described over 94 × 94 pixels. The microscope is operated in the reflection mode with a 10 × objective lens having effective NA= 0.22. The image of the target with a well corrected beam is shown in Fig. 4.11(i). The I_{gop} of the target is constructed by thresholding the acquired image and is shown in FIg. 4.11(ii). We then holographically introduce aberrations into the illumination beam phase profile to make the beam aberrated. The aberration modes represented by single indexed Zernike modes Z_7, Z_8, Z_9, and Z_{10} [67] are incorporated into the illumination beam. Numerically constructed illumination PSFs in the presence of Z_7, Z_8, Z_9, and Z_{10} in the illumination beam are shown in Fig. 4.12(ii). The experimental images of the target using the illumination beam aberrate with various modes are shown in Fig. 4.12(i).

The imaging PSF arrays are estimated by employing the proposed scheme on the images in Fig. 4.12(i) with Fig. 4.11(ii) as the I_{gop}. The estimated imaging PSFs are shown in Fig. 4.12(iii). These imaging PSFs are then employed for image deconvolution using the Richardson-Lucy algorithm. The reconstructed images after 50 iterations are shown in Fig. 4.12(iv). We also perform blind deconvolution on the same experimental images shown in Fig. 4.12(i) and reconstructed images after 50 iterations are seen in Fig. 4.12(v). We notice that using the estimated imaging PSF in the deconvolution process facilitates the removal of the effect of aberrations more efficiently than the blind deconvolution process. To further clarify the same, we draw line plots along the solid red line in Fig. 4.12(a)(i) for the I_{gop}, experimental

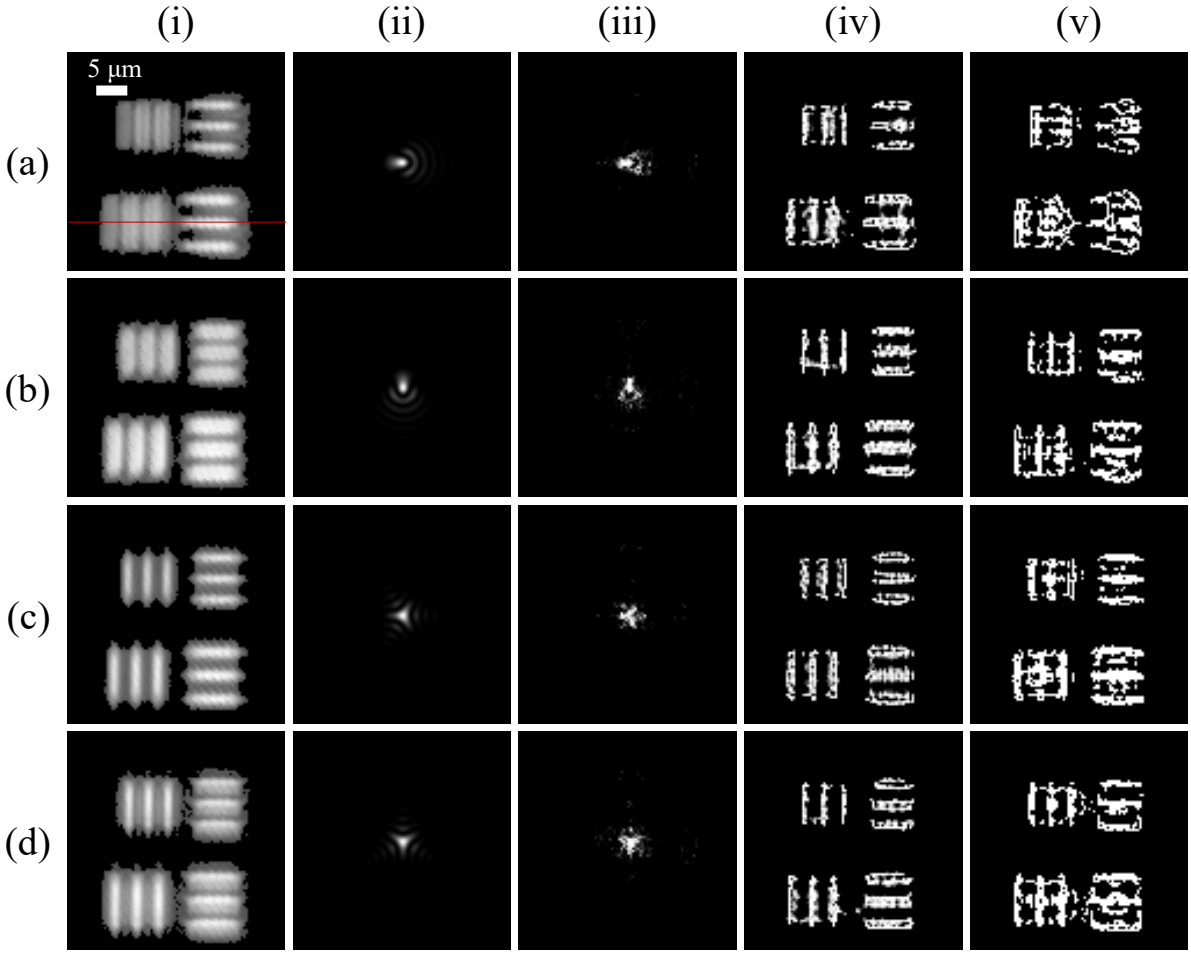

Figure 4.12: (i) The experimental confocal image of the target using (a) Z_7, (b) Z_8, (c) Z_9 and (d) Z_{10} aberrated illumination beam, (ii) numerically obtained illumination beam using (a) Z_7, (b) Z_8, (c) Z_9 and (d) Z_{10} aberration modes, (iii) the estimated imaging PSF corresponding to (a) Z_7, (b) Z_8, (c) Z_9 and (d) Z_{10} aberrated images, (iv) the reconstructed images after Richardson-Lucy deconvolution (RL) corresponding to (a) Z_7, (b) Z_8, (c) Z_9 and (d) Z_{10} aberrated images and (v) the reconstructed images after blind deconvolution (BL) corresponding to (a) Z_7, (b) Z_8, (c) Z_9 and (d) Z_{10} aberrated images.

image, and the respective deconvolved images. The plots are shown in Fig. 4.13 provides a clear demonstration that the contrast in reconstructed images are better after the Richardson-Lucy deconvolution than after the blind deconvolution. The results from the two experiments clearly show that our PSF estimation scheme works in different optical microscopes irrespective of the imaging geometry. The imaging PSF is estimated using a simple binary target, however, once estimated, the same can be used for different complex targets provided the illumination PSF remains the same.

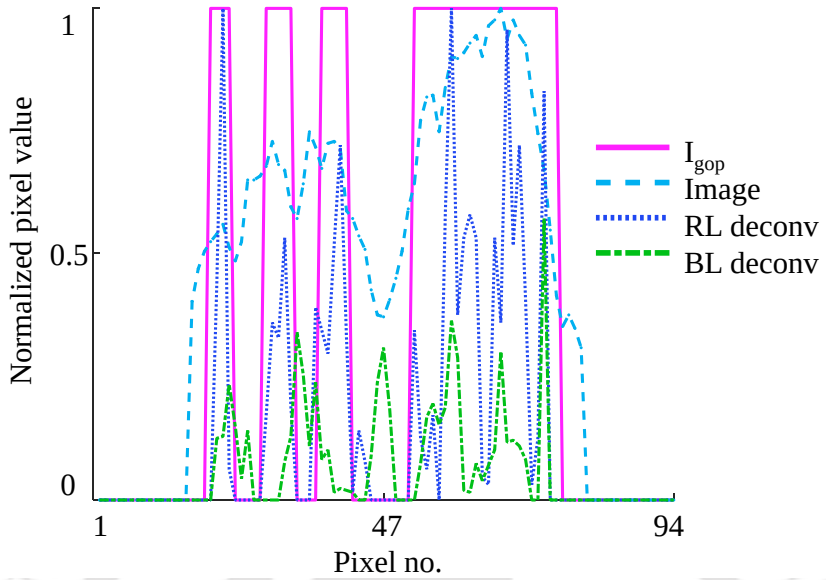

Figure 4.13: Line plots along the red solid line shown in Fig. 4.12(a)(i) for the images in Fig. 4.12(a)(i), (iv), (v) and Fig. 4.11(ii).

4.5 Summary

In this chapter, we have introduced a PSF estimation scheme based on minimizing the least square error between the image of a target, whose geometrical-optics predicted image, I_{gop} can be constructed, and the image obtained by convolving the I_{gop} with a stochastically constructed imaging PSF. We have demonstrated the working of the proposed scheme first on numerically constructed targets. We have also experimentally demonstrated the working of the proposed scheme in widefield and confocal microscopes involving different numerical apertures.

CHAPTER 5

Implementation of resolution enhancement schemes using the array detection microscope

5.1 Introduction

This chapter presents the implementation of resolution enhancement schemes in a beam scanning microscope using the array detection. Here, in addition to the confocal microscope with variable pinhole diameter, we demonstrate the implementation of image scanning microscopy and image subtraction microscopy exploiting the array detection using both mechanical and non-mechanical beam scanning mechanisms. We present results from a set of proof-of-principle experiments to show the relative enhancement in resolution. We also propose a novel intensity subtraction microscopy technique and compare the results with the image subtraction microscopy technique. The chapter ends with a quantitative estimation of the lateral resolution enhancements in term of the respective imaging PSF estimated by our PSF estimation scheme.

5.2 Brief description of the experimental arrangements

The array detection microscopes are divided into two broad categories based on the beam scanning mechanism used. One category of systems is mechanical scanning, which uses a galvo mirror based beam scanning while the other is a non-mechanical scanning category that

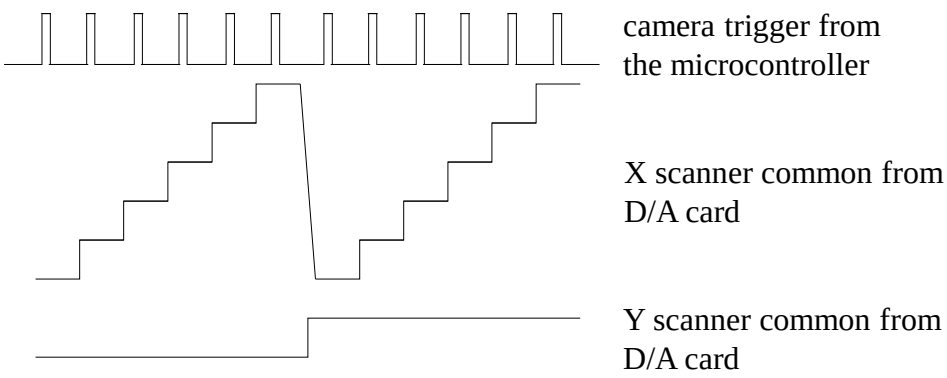

Figure 5.1: Schematic showing the relative timing of the camera trigger and the command signals for the X and Y scanners.

uses holographic beam scanning. In the below sections we provide a brief description of each category of systems.

5.2.1 Galvo mirror based scanning system

The experimental arrangement for implementing the scanning microscope with an array detector is more or less same as the setup shown in Fig. 3.11 of chapter 3. A binary hologram is written onto the LCSLM device to generate the illumination beam using the $+1$ order diffracted beam. The beam scanning over $N \times N$ pixels of the sample plane is performed by two galvo scan mirrors connected to one another by a 4f relay unit. The light from the sample plane is collected by the same objective lens, which focuses the illumination beam onto the sample plane, and after de-scanning, the beam is transmitted by the beam splitter $BS2$. The lens L_5 focuses the light from the sample plane onto the array detector. Here we take the high speed CMOS camera (Basler A504k) as the array detector. The synchronized operation of the camera, galvo scanner, and the LCSLM device is realized with the help of the synchronization unit via the generation of appropriate drive signals. The user has control over all the active units of the experimental setup via a graphical user interface in the PC written using the LabVIEW programming environment. For each scan position, a detector window of size, say, $n \times n$, is defined in the camera image surrounding the illumination spot, and the same is stored in the PC for the reconstruction of the image later.

In order to avoid the jittering of the scan mirrors, we use the digital to analog card (D/A) card attached to the PC to generate command signals for the two scan mirrors, as seen in Fig. 5.1. It shows how the X mirror, for instance, is moved to six scan positions for a given position of the Y mirror. For each position of the X scan mirror, sufficient time is allotted for the mirror to stabilize before a trigger is generated for the camera. The camera trigger signal is generated

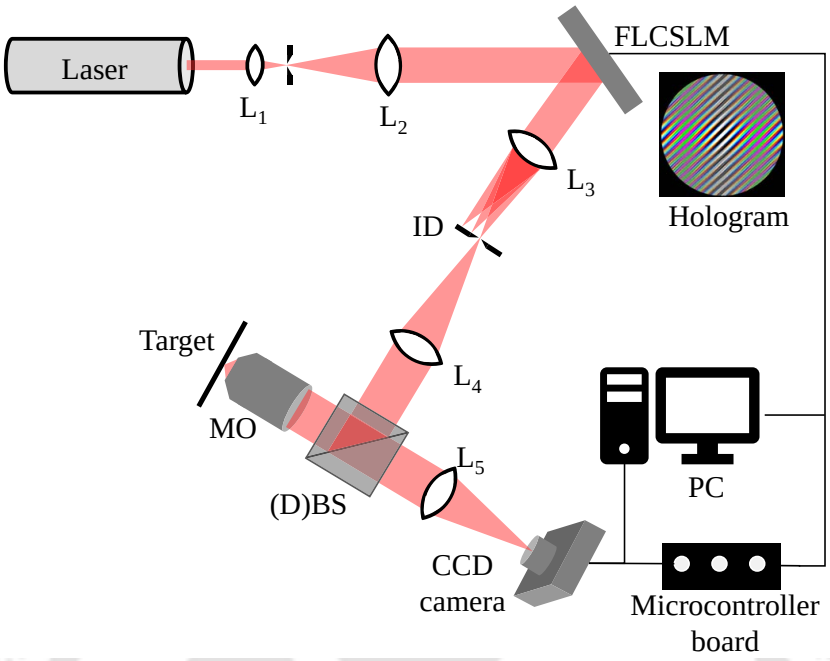

Figure 5.2: Schematic of the experimental setup to implement array detection in a holographic scanning microscope.

using the microcontroller based synchronization unit. The same unit also sends a trigger signal to the D/A card for the synchronized operation of the two scan mirrors. A stable illumination beam is captured using 200 active rows of the Basler camera, allowing the acquisition of at least 2000 detector arrays per second.

5.2.2 Holographic based scanning system

In the holographic scanning based system, a dynamically re-configurable binary hologram is used to achieve the beam scanning. The principle and algorithm for the construction of the binary holograms have already been discussed in section 3.2.2. In Fig. 5.2, a schematic diagram of the array detection microscope using the holographic beam scanning is presented [108]. A laser beam is expanded and collimated using lenses L_1 and L_2. The collimated beam is incident on the FLCSLM, where binary holograms are displayed using standard video signal at a refresh rate of 60 colored (24 bit) images per second. The $+1$ order diffracted beam is isolated from other diffracted orders with the help of L_3 and the Iris diaphragm ID. The beam is then reflected by the (dichroic) beam splitter, (D)BS, after passing through the lens L_4 and focused by the microscope objective lens L_5. The (D)BS, the objective lens, and the sample plane stage are the parts of the inverted microscope stage. The light from the sample plane is received by the same objective lens and is then transmitted by the beam splitter to be focused onto a

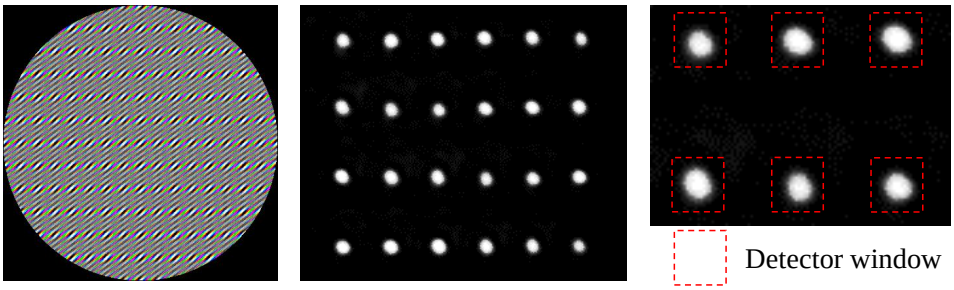

Figure 5.3: An example of (i) a 24-bit color image for the holographic scanning,(ii) the resulting 24 illumination spots captured in a single camera frame, and (iii) describing the detector window surrounding each such focal spot to obtain the detector array.

CCD camera. The FLCSLM is set to display 24 constituent bit planes of each 24-bit color image, each bit plane for a duration of about 700 μs, in a time sequential manner. Therefore by displaying a sequence of binary holograms, the illumination spot can be sent precisely to 1440 different locations on the sample plane in one second. In order to capture each of these scan positions in independent frames of the camera, the camera has to have a frame rate of at least 1440 Hz. However, due to the slow frame rate of our camera, we decided to capture all the 24 scan positions corresponding to one color image in one single frame of the camera. This requires that all the 24 scan positions are well separated so that there is no overlap between the adjacent focal spots present in a single camera frame. As the camera is operating at a frame rate of 15 Hz, we write only 15 different color images onto the FLCSLM in one second. The synchronized operation of the camera and the FLCSLM display is realized with the help of our in-house developed microcontroller-based synchronization unit. Thus even with an ordinary slow camera, it takes only about 45 seconds to scan over 128×128 pixels of the sample plane and to capture the detector array for each scan position.

Figure 5.3(i) shows a representative 24-bit color image that gives rise to 24 well dispersed illumination spots, as shown in Fig. 5.3(ii), which are captured in a single image frame of the camera. The 24 illumination spots are arranged in a square area, so the separations between two adjacent spots along the horizontal and vertical direction are different. Then 24 detector windows surrounding each of the illumination spots as shown in Fig. 5.3(iii), are described. The 2D array of data in each detector window constitutes the detector array for the microscope. It is extracted from the camera image to be stored in the PC for each scan position. After completion of the scanning process of the entire sample plane, the PC saves a four dimensional (4D) array data set, which can be further used for post-acquisition processing. Considering that the scanning is over $N \times N$ pixels and the detector window contains $n \times n$ pixels, the 4D array

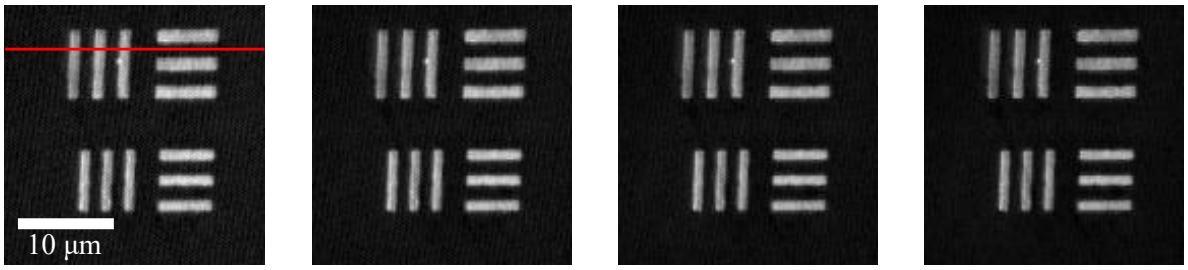

(i) (ii) (iii) (iv)

Figure 5.4: Reflected light confocal images of the USAF 1951 target over an area of 27 μm$\times$27 μm using objective 60X (water immersion, 1.2 NA) in the galvo mirror based scanning system. Images are obtained using pinhole dimensions (i) 2 Airy unit, (ii) 1.5 Airy unit, (iii) 1 Airy unit and (iv) 0.5 Airy unit.

has a dimension of $N \times N \times n \times n$, so that every scan position corresponds to a detector array of size $n \times n$.

5.3 Implementation of confocal imaging with variable pinhole size

For both the holographic scanning based and galvo scanning based array detection microscopes, it is possible to describe a digital pinhole in the detected plane with a radius bearing from zero to n number of pixels [109]. We can therefore implement confocal microscopy with variable pinhole size using the 4D array. For each pinhole size, a confocal image is constructed by integrating all the pixel values within the pinhole described in the detector array. Confocal imaging with variable pinhole size can be implemented for reflection and the fluorescence modes. However, as a demonstration of the proposed scheme below represent results using the reflected light [110].

5.3.1 Results from the galvo mirror based scanning system

We perform scanning over 128×128 pixels and describe a detector window of size of 200×200 pixels in the camera image for each scan position. We constructed confocal images using pinhole sizes varying from 2 Airy unit (AU) to 0.5 AU. Figure 5.4 shows the images of a USAF 1951 resolution test target with the 60$\times$ water immersion objective lens over an area of about 27 μm $\times$ 27 μm. Figures 5.4 (i$\rightarrow$ iv) show the reconstructed confocal images with pinhole radii equal to 2 Airy unit, 1.5 Airy unit, 1 Airy unit, and 0.5 Airy unit, respectively. In order to visualize the variation in image quality as the pinhole size changes, we plot the intensity in the

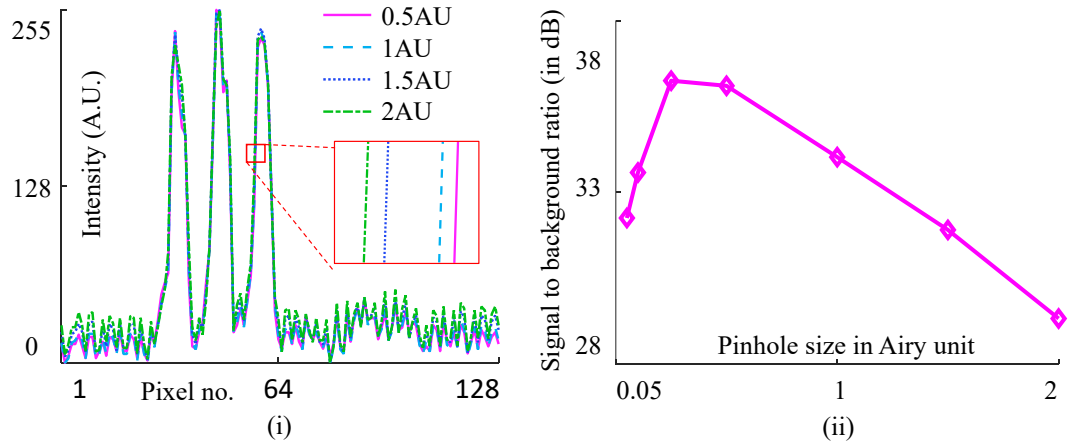

Figure 5.5: (i) Line plot over all the images along the solid red lines in Fig. 5.4(i) showing the edge response and (ii) the plot of SNR as a function of pinhole diameter.

reconstructed images along a line, as shown in Fig. 5.4(i). It is observed from the plot seen in Fig. 5.5 (i) that with the reduction in the pinhole size, the edge of the line pattern in the target becomes sharper. Moreover, a decrease in the pinhole size reduces the amount of background noise present in the final image. We have calculated the signal to background ratio (SBR) of the final image by using the definition [111]

$$SBR = 20log_{10}\frac{I_{max} - I_{min}}{(\frac{1}{n}\sum_{i=1}^{n}(I_i - \bar{I})^2)^{1/2}} \tag{5.1}$$

Here I_{max} is the maximum intensity in the image, I_{min} is the minimum intensity in the image, and $\bar{I}$ is the mean of all the pixels representing the background, with n as the number of such pixels in the image. The SBR of the final image with different pinhole dimensions is calculated and is shown as a plot in Fig. 5.5 (ii). It is noticed that SBR initially increases as the pinhole size decreases. Enhancement in SBR with the reduction in pinhole diameter for larger pinholes can be attributed to the reduction in the background noise and unwanted reflections or speckles. However, if the pinhole diameter is further decreased, then the SBR too starts decreasing due to the smaller amount of signal forming the image. Thus the proposed system facilitates tuning the imaging parameters to arrive at a confocal image that has the right resolution and SBR from the same set of detector array data.

5.3.2 Results from the holographic based scanning system

Here again, we scan the USAF test target over 120×120 pixels with each scan position corresponding to a detector array size of 40×40 pixels. From the 4D data, we reconstruct confocal images using pinhole size varying from 2 Airy unit (AU) to 0.5 AU. Figures 5.6 (i→ iv) show

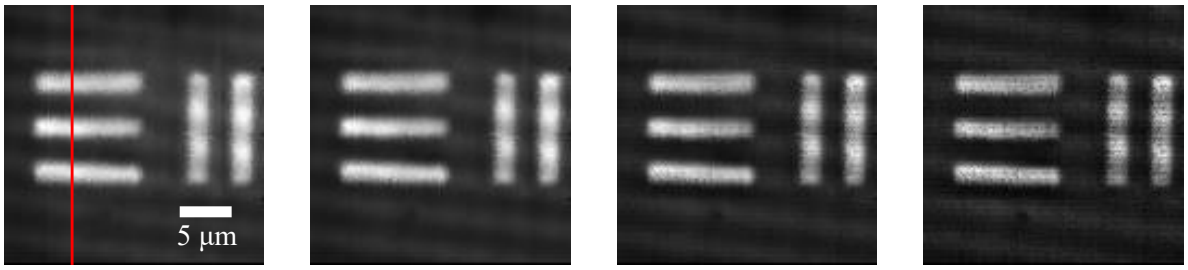

Figure 5.6: Reflected light confocal images of the USAF 1951 target over an area of 25 μm×25 μm using objective 40X (0.4 NA, air) in the holographic scanning based system. Images are obtained using pinhole dimensions (i) 2 Airy unit, (ii) 1.5 Airy unit, (iii) 1 Airy unit and (iv) 0.5 Airy unit.

the reconstructed confocal images with pinhole radii equal to 2 Airy unit, 1.5 Airy unit, 1 Airy unit, and 0.5 Airy unit, respectively. Improvement in the images in terms of background noise can be seen in the line plot shown in Fig. 5.7 (i), where we plot the intensity in the images along the line shown in Fig. 5.6 (i). We have also calculated the SBR of the reconstructed

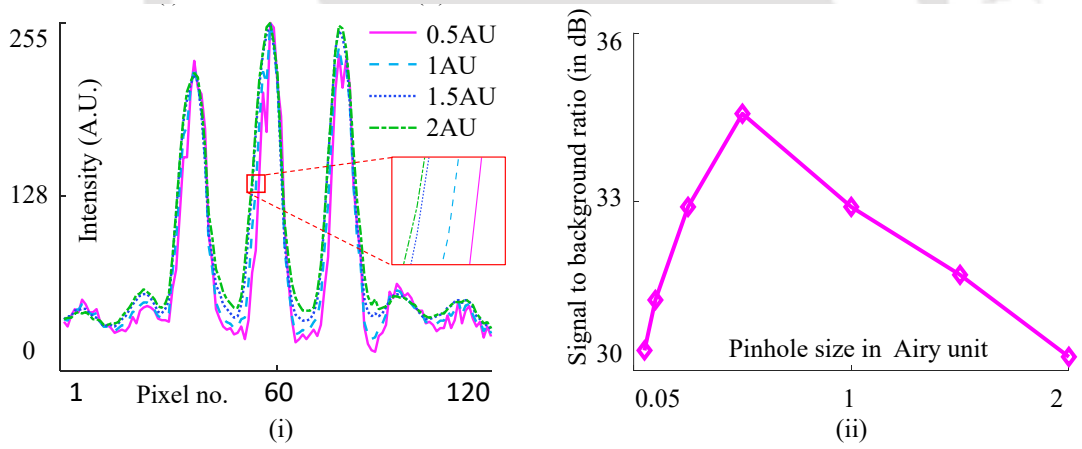

Figure 5.7: (i) Line plot profiles over all the images along the solid red lines in Fig. 5.6(i) showing the edge response. (ii) Effect of the different pinhole dimensions on the SBR of the image.

image by using the Eq. 5.1, and a plot is shown in Fig. 5.7 (ii). We notice that, likewise the galvo mirror based scanning system here also the SBR increases initially as the radius of the pinhole decreases owing to the reduction in the amount of light reaching the detector due to unwanted reflections and then it starts decreasing.

It is to be noted here that for both the systems, the size of the pinholes in terms of the Airy unit may not be precisely defined due to the error in estimating the size of the ideal Airy pattern

in the respective detector planes. This has led to some variation in the values of pinhole sizes giving the maximum SBR as well as deviation from the expected size of the pinholes.

5.4 Implementation of image scanning microscopy (ISM)

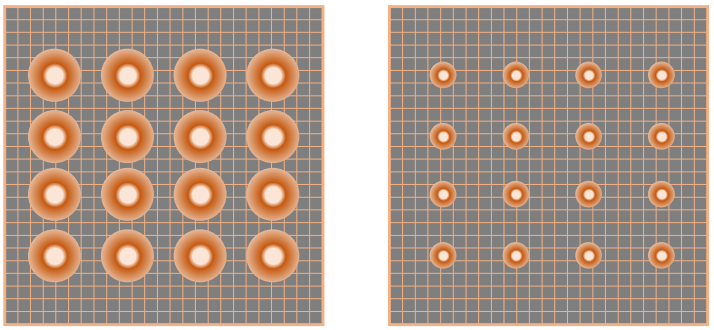

Figure 5.8: ISM image processing which comprises scaling down of the detector array and put the array to the same position.

As discussed already in section 2.3.2, image scanning microscopy (ISM) [20, 21] provides the easiest way to enhance the lateral resolution and at the same time not compromising on the signal to noise ratio in the image. With the availability of the detector array for each scan position, it is possible to implement image scanning microscope using our two versions of the array detection microscopes. The image scanning microscopy can be implemented both in the reflection mode as well as in the fluorescence mode, even though the advantages of image scanning microscopy becomes more evident in the fluorescence mode due to the smaller signal available from the sample plane in a fluorescence imaging system.

To implement the ISM, we first multiply each detection window by a circular mask often to be a size equal to the 1 AU. Then the detector array, as in the detector window, is scaled down by a factor 1/2, assuming that the pixel to pixel separation in the detector window is equal to the separation between two scan positions in the final reconstructed image. Since the detector window is in the digital form, the scaling down by a factor of 1/2 can be achieved by a 2×2 binning of the corresponding 2D array. The contracted detector array is then placed in a 2D array of size N×N, representing an equal number of scan positions, with the center of the detector array coinciding with the pixel corresponding to the respective scan position. Figure 5.8 depicts the pixel reassignment in an ISM system. The detector records an array containing the illuminated region for the given scan position at each scan position, as shown in Fig. 5.8 (i). Afterward, this is followed by scaling down of all the detection array by a factor of 1/2. The final 2D image of the sample is obtained by placing all such scaled downed detection array

placed at their original position as illustrated in Fig. 5.8 (ii). For example, the detection PSF with a diameter of 4 pixels has been reduced to a PSF with a diameter equal to 2 pixels by performing a 2×2 binning. However, the center to center separation between two adjacent PSFs remains unaltered. The final 2D array is thus updated after the repositioning of the detector array corresponding to each scan position. Below we present the results demonstrating the implementation of the image scanning microscope both in the reflection mode and in the fluorescence mode.

5.4.1 Results from galvo mirror based scanning system

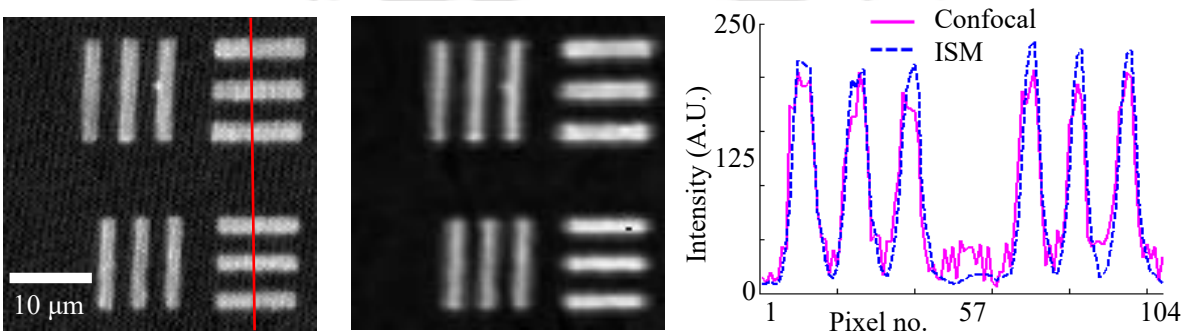

Figure 5.9: (i) Confocal image and (ii) the respective ISM image reconstructed using the galvo mirror based array detection microscope working in the reflection mode. (iii) Line plots over the two images along the line shown in (i) to indicate apparent increase in resolution and SNR.

Figure 5.9 (i) shows the confocal image of a portion of the USAF 1951 target captured by the galvo mirror based scanning system working in the reflection mode. The data corresponds to 128×128 scan positions with each scan position corresponding to a 200×200 detector array. The respective reconstructed ISM image is seen in Fig. 5.9 (ii). The line plots over the two images, as seen in Fig. 5.9 (iii) show the enhancement in the contrast and the reduction in noise in the ISM image relative to the confocal image.

5.4.2 Results from the holographic based scanning system

Figure 5.10 (i) shows the confocal image of another portion of the USAF 1951 target captured by the holographic scanning based system working in the reflection mode. The data corresponds to 120×120 scan positions with each scan position corresponding to a 40×40 detector array. The respective reconstructed ISM image is seen in Fig. 5.10 (ii). Likewise, the galvo mirror based scanning system, here also the line plots over the confocal and ISM images as seen in Fig.

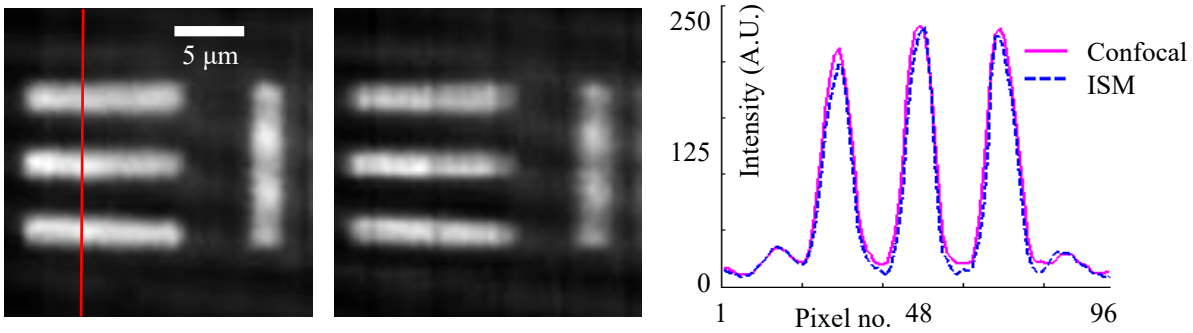

Figure 5.10: (i) Confocal image and (ii) the respective ISM image reconstructed using the holographic scanning based array detection microscope working in the reflection mode. (iii) Line plots over the two images along the line shown in (i) to indicate apparent increase in resolution and SNR.

5.10 (iii) show the enhancement in the contrast and the reduction in noise in the ISM image relative to the confocal image.

Image scanning microscopy in the fluorescence mode using the holographic based scanning system

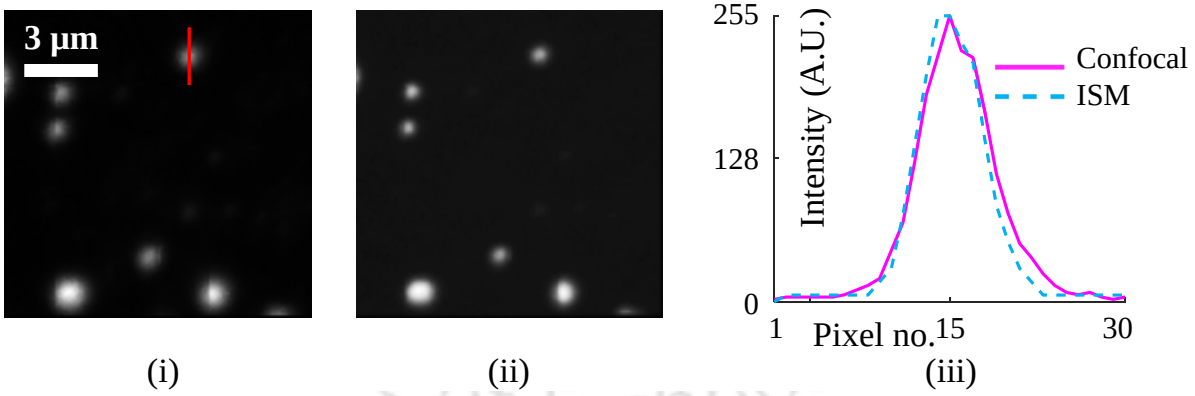

Figure 5.11: (i) Confocal and (ii) the corresponding ISM image obtained using the holographic scanning based array detection microscope working in the fluorescence mode. (iii) Line plot along the solid red line in (i), showing the enhancement in lateral resolution in the ISM image relative to the confocal image.

We also demonstrate the implementation of image scanning microscope in the fluorescence mode using the 4D data captured with the holographic based scanning system. The schematic of the experimental arrangement of the scanning optical microscope in the fluorescence mode is the same as the one working in reflection mode (Fig. 5.2) with a dichroic beam splitter in

conjunction with a long-pass emission filter replacing the beam splitter placed between the camera and the sample plane. Here we use a dichroic beam splitter with a cutoff wavelength at around 640 nm, which reflects the excitation laser at 633 nm towards the sample plane. The combination of the beam splitter and the emission filter transmits light from the sample plane with a wavelength greater than the cutoff wavelength.

Fluorescent bead sample preparation: Fluorescent beads are available in different sizes ranging from 10 nm to 15 μm with different excitation and emission spectra. Here we use 200 nm diameter FluoSpheres beads (Carboxylate-Modified Microspheres, Make: Thermo Fisher Scientific) having peak excitation/ emission wavelengths 625/645 nm. The sample preparation steps of the fluorescent bead is given below

1. The bead solution is diluted by mixing 10μL of concentrated bead solution with 90μL of distilled water for a 1:100 dilution factor.
2. The solution is further diluted by a factor of 1:10^4 by mixing 10μL of the solution with 90μL of distilled water.
3. The bead solution is sonicated for 5 minutes to avoid inhomogeneous bead distribution on the coverslip due to aggregation.
4. A coverslip and a microscope slide are cleaned by ethanol.
5. 10μL of bead suspension is then applied on the coverslip and allow it to dry on air.
6. The coverslip is mounted on a microscope slide and sealed with nail polish.

We then perform the acquisition of detector arrays using fluorescence light from the sample plane with a 100 $\times$, 1.4 NA oil immersion objective lens. Figure 5.11 (i) shows the reconstructed confocal image and Fig.5.11 (ii) shows the corresponding ISM image. To be noted that in the fluorescence mode, the scaling down factor increases by a small amount due to the Stokes shift. Figure 5.11 (iii) shows the line plots of normalized pixel values along the solid red line on the bead. It is observed that there is a marginal enhancement in the resolution in the case of ISM.

5.5 Implementation of image subtraction microscopy

As we discussed previously in chapter 3, the image scanning microscopy primarily enhances the lateral resolution. Fortunately, the 4D data obtained from the array detection microscope which can represent a confocal microscope with different pinhole sizes can also be employed

to implement image subtraction microscopy. The image subtraction microscopy is a recent microscopy technique that can enhance the axial resolution of the image [112]. The technique involves the subtraction of two confocal images obtained using two pinholes of different sizes. One confocal image of the sample plane is constructed using a circular pinhole of diameter equal to one Airy unit, and yet another image of the same sample place is constructed using another pinhole with a much larger radius. The final image with the enhanced axial resolution is constructed by subtracting the background information from the first image. The background information, on the other hand, is obtained by subtracting the second image from the first image. One of the issues of the subtraction method is the appearance of the pixels with negative intensity values. When such pixels with negative values appear, the normal method is to make all such pixels zero. However, making all the negative value zero leads to loss of information. To avoid such loss of information and appearance of pixel of negative value there has to be a subtraction coefficient.

The expression of the final image can be written as

$$I_{sub} = I_1 - \alpha(I_2 - I_1) \tag{5.2}$$

Here I_1 is the confocal image formed using a pinhole of diameter equal to the Airy disc, and I_2 is the image formed using a very large pinhole that allows all the light from the sample plane. α is the subtraction parameter whose value is chosen in such a way to avoid the emergence of any negative pixel values in I_{sub}.

In our array detection microscope we can easily implement such a scheme using our detector array without the need to use two physical pinholes in the detector plane. Below we present results to demonstrate the implementation of image subtraction microscopy using both the versions of the array detection microscopes.

5.5.1 Results from the galvo mirror based and holographic based scanning systems

We employ the 4D data set of our array detection microscopes to implement array detection microscopy. We first obtain the confocal image I_1 by integrating the pixels inside a circle of radius 1AU for each detector array and obtain the image I_2 by integrating all the pixels in the detector array. Figure 5.12 (i) shows the image subtraction microscopy image of the USAF test target obtained using $\alpha = 1$ on the 4D data from the galvo mirror based scanning system working in the reflection mode. Figure 5.12 (ii) shows the image subtraction microscopy image of a part of the USAF test target obtained using $\alpha = 0.39$ on the 4D data from the holographic scanning based system working in the reflection mode. We then construct the image subtraction

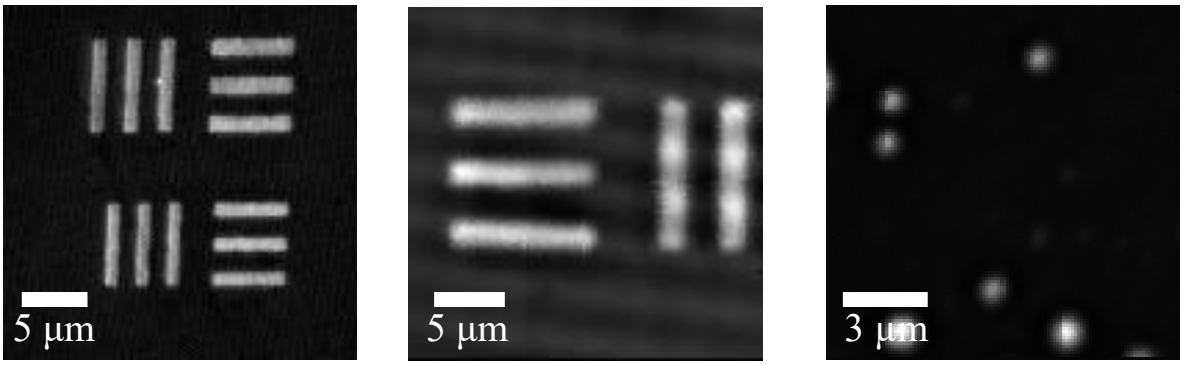

Figure 5.12: Images obtained using the image subtraction microscopy technique implemented with the (i) galvo mirror based scanning system working in the reflection mode, (ii) holographic based scanning system working in the reflection mode and (iii) holographic scanning based system working in the fluorescence mode.

microscopy image using $\alpha = 0.217$ on the 4D data from the holographic scanning based system working in the fluorescence mode and the same is shown in Fig. 5.12 (iii).

We estimate the contrast in each of the images shown in Fig. 5.12 and compare the same with the respective confocal images. We define the contrast as

$$C_i = \frac{I_{max} - I_{min}}{I_{max} + I_{min}} \tag{5.3}$$

Here I_{max} and I_{min} are the maximum and minimum pixel values, respectively, in the image. The contrast in the case of Fig. 5.12 (i) has improved to 0.2456, while the contrast in the case of the respective confocal image is 0.2118. Similarly, the contrast in the case of Fig. 5.12 (ii) has improved to 1, while the contrast in the case of the respective confocal image is 0.3484.

The contrast in the image subtraction microscopy image in the fluorescence mode is estimated to be 0.9549, which for the respective confocal image is 0.7080.

The enhancement of contrast in the three cases above indicates a reduction in the background light and thus, an enhancement in the axial resolution.

5.6 Introduction to novel intensity subtraction microscopy

In the image subtraction microscopy, choosing the value of the factor α plays a crucial role in deciding the image quality. A bigger value of α can provide superior results in some parts of the image, however, with more possibility of producing negative pixels in other parts of the image. To avoid the negative pixels, the factor α should be carefully chosen to balance between

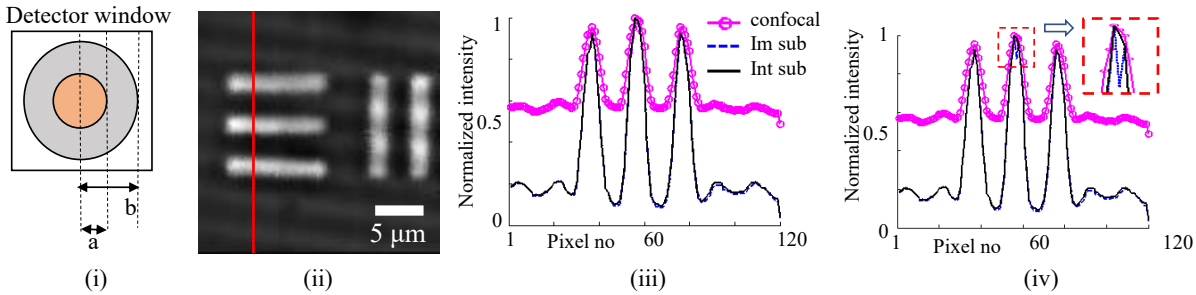

Figure 5.13: (i) Schematic of the detector window (i.e. detector array) showing two concentric circles of radii a and b to implement the proposed intensity subtraction microscopy (i.e. Int sub), (ii) Image of the USAF test target using the proposed scheme on the data recorded using the holographic scanning based system working in the reflection mode. (iii) Line plots along the red line is shown in (ii) for the confocal image, image subtraction microscopy (i.e. Im sub) image and Int sub image of the same target. (iv) Same lines plots as (iii) after a bright pixel is introduced in the detector array corresponding row index 56 and column index 20. Inset shows the magnified view of part of the plot highlighting the artifact that may arise in the Im sub image.

contrast enhancement and appearance of negative pixels. Here we propose a novel intensity subtraction microscopy where the role of the factor α is removed.

In the proposed scheme, we first construct a confocal image using a pinhole with the smallest possible radius, which is often taken as the Airy disc radius. In the reconstructed confocal image, we then look for the pixel, which has the smallest yet a non-zero value. We take the detector array corresponding to that pixel and define two concentric circles of radii a and b as shown in Fig. 5.13 (i). We keep the radius a fixed, again preferably equal to the Airy disc radius, while we consider b to be a variable. The value of b is then increased starting from a, and for each value of b the difference between the net pixel values within the circle of radius a and within the annular region between radii a and b are estimated. We then arrive at the value of b, say b_z, which makes this difference zero. In our proposed scheme, the effective value of each reconstructed image pixel is defined as

$$p_{eff} = p_a - p_{b_z} \tag{5.4}$$

Here p_a and p_{b_z} are the integrated pixel values inside the inner circle and the annular region, respectively, for a given scan position.

5.6.1 Results

We employ the 4D image data obtained from the holographic scanning based systems working in the reflection mode to implement the novel intensity subtraction microscopy. The corresponding

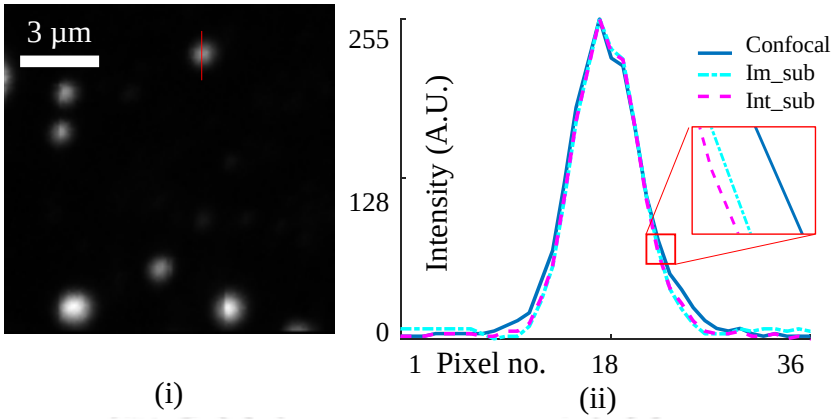

Figure 5.14: (i)Image of the 200nm bead using the proposed scheme on the data recorded using the holographic scanning based system working in the fluorescence mode. (ii) Line plots along the red line is shown in (i) for the confocal image, image subtraction microscopy (Im_sub) image and the proposed intensity subtraction microscopy (Int_sub) image.

detector array has size 40×40 pixels and 1 AU=25 pixels. The value of b_z is estimated to be 0.87. Figure 5.13 (ii) shows the final reconstructed image using the novel intensity subtraction microscopy technique. Figure 5.13 (iii) shows line plots of the normalized intensity along the line shown in Fig. 5.13 (ii) for the confocal image using a pinhole of size 1 AU and the respective image subtraction and novel intensity subtraction microscopy images. It is noticed that the novel scheme provides similar image contrast as the image subtraction microscopy. However, the image subtraction microscopy uses the entire detector array to obtain I_2, and any variation in the background light for different scan positions may introduce artifacts. In order to demonstrate this effect, we deliberately introduce a bright pixel at a corner in the detector array corresponding to a scan position (row index 56, column index 20) lying along the line shown in Fig. 5.13 (ii). Using the modified detector arrays, we again construct the confocal, image subtraction, and intensity subtraction microscopy images and repeat the same line plot. As seen in Fig. 5.13 (iii), there is a dip at the center of the middle line in the case of image subtraction microscopy, which is not present in confocal or intensity subtraction microscopy.

We also imaged the 200nm fluorescence bead and obtained the 4D data using the holographic scanning based system working in the florescence mode. The imaging conditions are kept the same as in the reflected mode. We then implement the novel intensity subtraction microscopy technique to the 4D data. The value of b_z is estimated to be 0.85. Figure 5.14 (i) shows the final reconstructed image using the novel intensity subtraction microscopy technique. Figure 5.14 (ii) shows line plots of the normalized intensity along the line shown in Fig. 5.14 (i) for the confocal, image subtraction and novel intensity subtraction microscopy images. We then calculate the FWHM of the bead for confocal, image subtraction microscopy, and

our proposed intensity subtraction microscopy images. The FWHM is found to be 750nm for the confocal image, 712nm for the image subtraction microscopy image, and 648nm for the proposed intensity subtraction microscopy image. Using the expression for the lateral resolution $\frac{0.51\lambda_{exc}}{NA}$ for NA=1.4 and λ_{exc}=633nm is found to be 230nm. However, the FWHM of the bead is much larger than the theoretical value. The primary reason behind the difference depends on the nonuniform amplitude distribution of the beam at the back focal plane of the objective, and the effective numerical aperture of the microscope is less than 1.4. Nevertheless, it is noticed that the resolution of the proposed intensity subtraction microscopy technique is more than the existing techniques, and 16% enhances the resolution than that of a confocal microscope.

5.7 Assessment of lateral resolution enhancement using the PSF estimation scheme

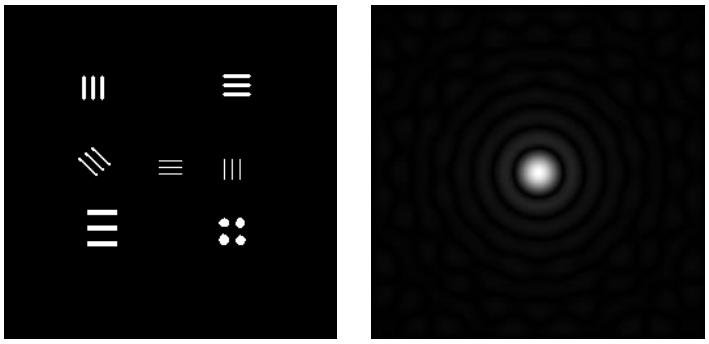

(i) (ii)

Figure 5.15: (i) The numerically constructed 2D target and (ii) the illumination PSF for the numerical simulation.

In the previous sections, we have employed our array detection microscope to implement the confocal microscope with variable pinhole size, image scanning microscopy, image subtraction microscopy, and novel intensity subtraction microscopy. The experimental results indicate that there is a clear enhancement in lateral resolution in the case of the image scanning microscope. In this section, we perform a numerical investigation of the lateral resolution enhancement by the various imaging schemes. Here we simulate various imaging schemes using a certain numerical target and obtain the effective imaging PSFs of the various imaging systems using our PSF estimation scheme introduced in chapter 4. The effective PSFs of the various imaging

systems are used to get a quantitative estimation of the lateral resolution enhancements in the respective imaging schemes in the ideal case.

A 2D numerical target as shown in Fig. 5.15 (i) is described over 256 ×256 pixels. The detector array data are computed by numerically scanning the illumination PSF, as shown in Fig. 5.15(ii), over the target. The 4D numerically obtained data is then used to implement various microscopy techniques.

5.7.1 Confocal microscopy with different pinhole sizes

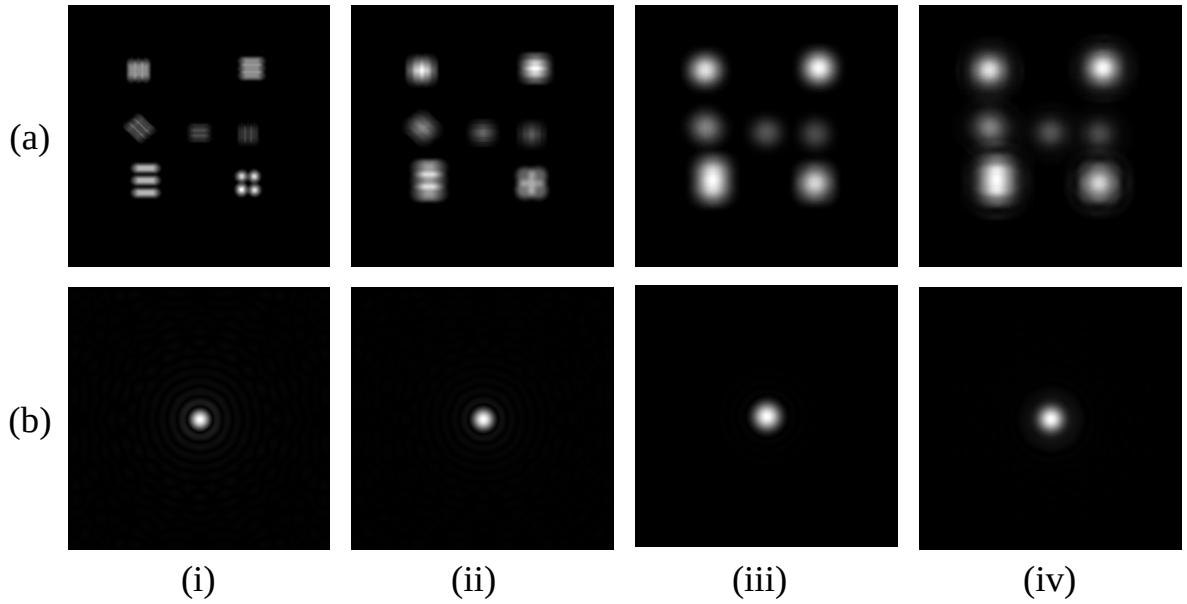

Figure 5.16: Confocal image constructed from the detector array data using pinhole dimension of (a)(i) 0.25AU, (ii) 0.5AU, (iii) 1AU and (iv) 1.5AU. (b) The corresponding effective imaging PSFs as obtained using the PSF estimation scheme.

We first construct the confocal image of the target by using pinhole diameter equal to 0.05 AU, 0.5 AU, 1 AU, and 1.5 AU, and the images are seen in Figs. 5.16 (a)(i)→(iv), respectively. The corresponding effective imaging PSFs, as estimated by our scheme, are shown in Fig. 5.15 (b)(i)→(iv) respectively. It is evident from this result that as the pinhole size of the confocal microscope decreases, the effective imaging PSF becomes narrower, thereby enhancing the lateral resolution.

5.7.2 Image scanning microscopy

We then use the numerically obtained 4D data to construct the ISM image which is shown in Fig.5.17 (i). This image is then used to obtain the imaging PSF using our estimation scheme,

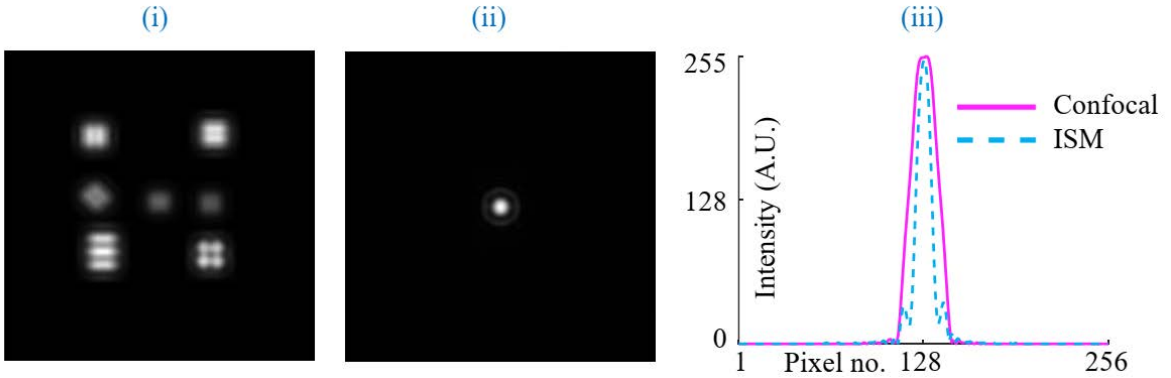

Figure 5.17: (i) ISM image constructed from the detector array data and (ii) the corresponding estimated imaging PSF.

and the PSF thus obtained is seen in Fig.5.17 (ii). Figure 5.17(iii) shows the line plots of the imaging PSFs for the confocal and the image scanning microscopy, respectively. The line plot clearly shows the enhancement in lateral resolution in the case of the image scanning microscope relative to the confocal microscope in the ideal case.

5.7.3 Image subtraction microscopy

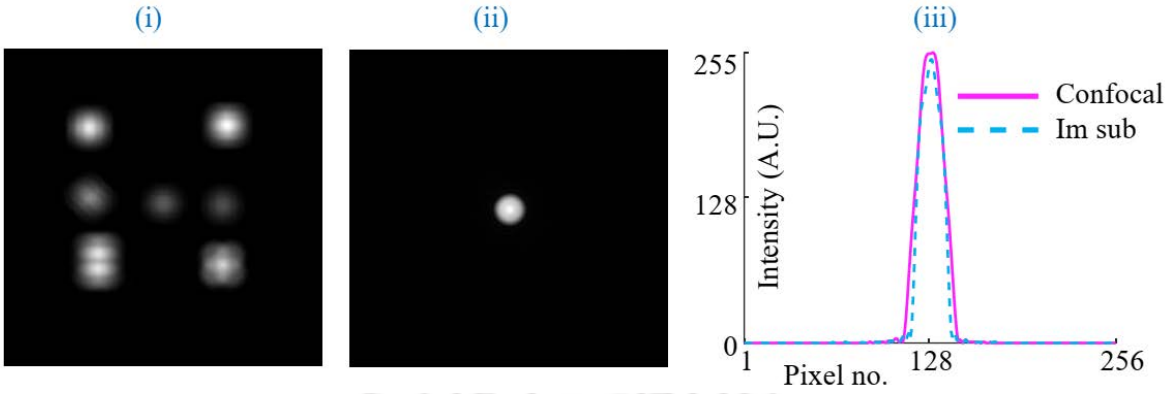

Figure 5.18: (i) Image subtraction microscopy image constructed from the detector array data and(ii) the corresponding estimated imaging PSF.

The numerically obtained 4D data is then employed to construct image subtraction microscopy images where we use α=0.00005. Figure 5.18 (i) shows the image subtraction microscopy image, which is then used to obtain the effective imaging PSF of the respective system. Figure 5.18 (ii) shows the imaging PSF as provided by our PSF estimation scheme. In order to highlight if there is an enhancement in the lateral resolution in the case of the image subtraction microscopy techniques, we do a line plot along the imaging PSF and compare the

same with the confocal system. The line plots are seen in Fig. 5.18 (iii), which indicates that there is no noticeable or significant enhancement in the lateral resolution in the case of the image subtraction microscopy technique.

5.8 Summary

In this chapter, we have developed two types of scanning optical microscope using the array detector, one using galvo mirror scanning and the other using holographic scanning. In the array detection microscope using scan mirrors, we have addressed the jittering issue of the scan mirrors by designing the command scheme of the scanners and synchronizing their movement with the camera. In the other system, we have performed the beam scanning without using any mechanical scanner by utilizing the fast response liquid crystal spatial light modulator. Our system can scan the entire sample plane at a reasonable time, even with an ordinary camera. We have employed our array detection microscopes to implement various imaging schemes such as confocal microscopy with variable pinhole size, image scanning microscopy, and image subtraction microscopy. Implementation of variable pinhole size in a confocal microscope, facilitates confocal imaging with an appropriate balance of lateral resolution and signal to noise ratio. Our proof-of-principle experiments using the image scanning microscope technique has demonstrated an enhancement in lateral resolution in both the reflection and fluorescence modes. We have also introduced a novel intensity subtraction microscopic technique. Both the image subtraction microscopy and the novel intensity subtraction microscopy technique enhance the axial resolution by reducing the amount of background light. In contrast to the image subtraction microscopy technique, in our novel intensity subtraction microscopy technique, some of the artifacts in the imaging process can be avoided. We have performed a numerical Investigation on the lateral resolution enhancement as achieved by the various imaging techniques implemented using our PSF estimation scheme.

CHAPTER 6

Implementation of STORM and integrating it with the array detection microscope

6.1 Introduction

In this chapter, we first describe the implementation of a STORM microscope to obtain super-resolution images of fluorescent samples. We then combine the STORM with our array detection beam scanning microscope to get the reflected light image of the same part of the sample without any modification of the optical setup. We present proof-of-principle experimental results that demonstrate the working of both the STORM setup and the array detection microscope when they are part of the same microscope stage.

6.2 EasySTORM as a lowcost yet robust way to realise STORM

EasySTORM is a super-resolution microscopy (SRM) technique proposed by Kwakwa et al. [113] based on the principle of single molecule localization of individual fluorescent molecule by switching them stochastically. It uses the direct stochastic optical reconstruction microscopy (dSTORM) technique [114] in a cost effective manner by incorporating low cost industry-grade lasers, open source software for image capture and ordinary scientific camera with decent imaging speed, sensitivity, and dynamic range. The blinking of fluorophores decides the quality of the super-resolution image. In the dSTORM, the switching/ blinking of the fluorophore

molecules is achieved by exciting the molecules rapidly and repeatedly to an excited singlet state. The molecules then come back to the ground state by emitting fluorescence photons after a few nanoseconds detected by the camera. However, a small fraction of molecules enter a relatively long lifetime (μs to ms) non-fluorescent triplet state. The molecules present in the triplet states do not emit fluorescence light but eventually return to the ground state and again participate in the normal fluorescence cycle. Afterward, the single fluorescent molecules are imaged in a temporal manner over thousands of image frames. From each image frame, the intensity distributions of the single molecules are approximated to 2D Gaussian functions, and the exact locations of the molecules are determined. Such single molecule locations from different image frames are then combined to produce the super-resolved image of the sample [115].

As we have discussed already, the STORM setups usually are implemented on a widefield microscope, and hence it will be difficult to capture a confocal image of the same part of the sample on which the super-resolved imaging scheme is applied. However, we have seen that the array detection microscope can provide much better lateral resolution compared to a confocal microscope without compromising on the signal level. Therefore it will be really useful from the application point of view if the STORM microscope is combined with the array detection microscope

6.3 Basic requirements of the STORM setup

Localization based SRM setup is usually operated on an inverted microscope working in widefield epi-fluorescence mode. Single molecule localization microscopy technique, on the other hand, requires high power lasers, high NA objective lens, dichroic filters, and a camera. High power laser with a very good beam quality such as narrow bandwidth output will be expensive. However, the industry-grade low-cost laser can also be used in combination with a narrow band excitation filter to produce an illumination beam with a narrow band excitation. Multi wavelength illumination can also be realized by combining a number of laser beams by a beam combiner to give rise to a single beam path [116].

STORM usually requires electron-multiplying charge-coupled device (EMCCD) cameras with 90% QE, but it can be replaced by a CCD or a CMOS camera with 30%-40% QE. There is of course, a performance difference between two cameras, particularly with respect to noise and QE in a specific spectral range. Even though the localization precision is affected by a few nanometers in the case of the industry-grade camera, such a small amount of inaccuracy does not play a crucial role for many biologists or users of SRM [117].

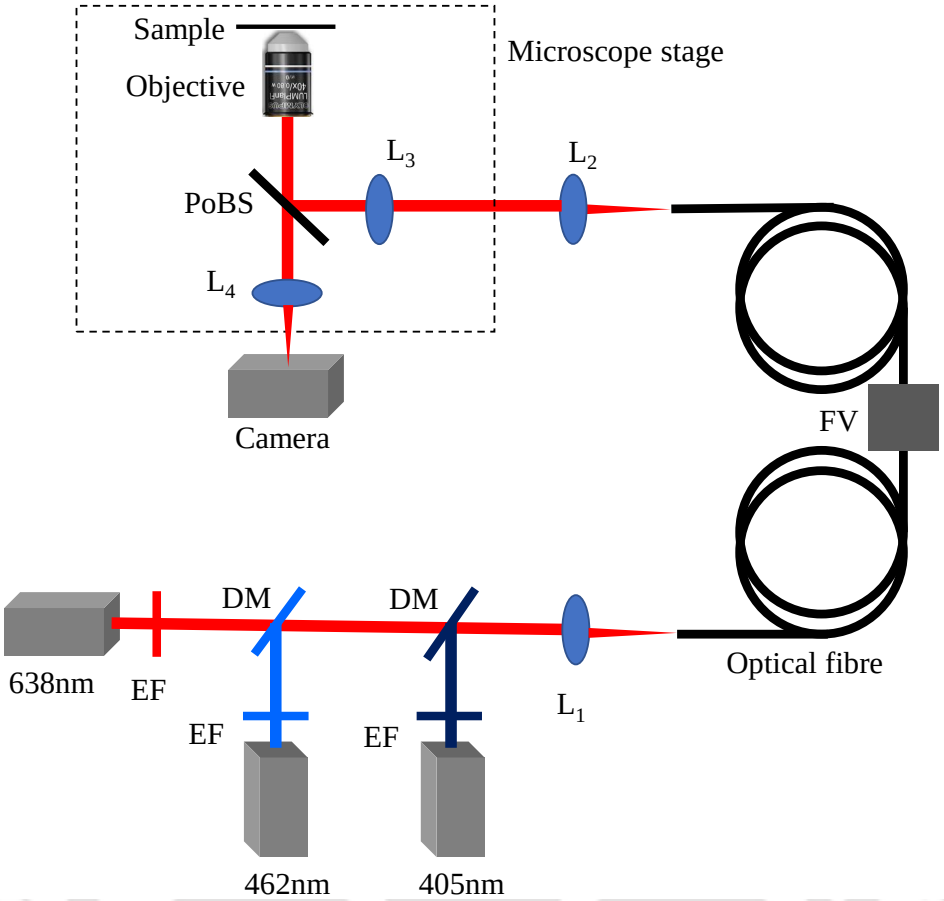

Figure 6.1: Schematic diagram of the STORM setup comprising three excitation lasers.

The preparation of samples remains the most important part of localization microscopy. The ability to localize single molecules depends on the choice of fluorophore that exhibits a photophysical behavior, often referred to as blinking. An oxygen-scavenging buffer made up of several chemicals and enzymes is used in combination with reducing agents to enable the blinking of the fluorescent molecules [118].

6.4 Implementation of STORM setup

We develop a STORM setup in our laboratory as a part of a collaborative work with Imperial college London, United Kingdom [1]. We have already discussed in the previous section that

[1]Project : Open Scope of Imperial College London. Instrumentation part was helped by Dr. Frederik Gorlitz, and the sample preparation part was helped by Dr. Edwin Garcia, both from the Photonics group of Imperial College London.

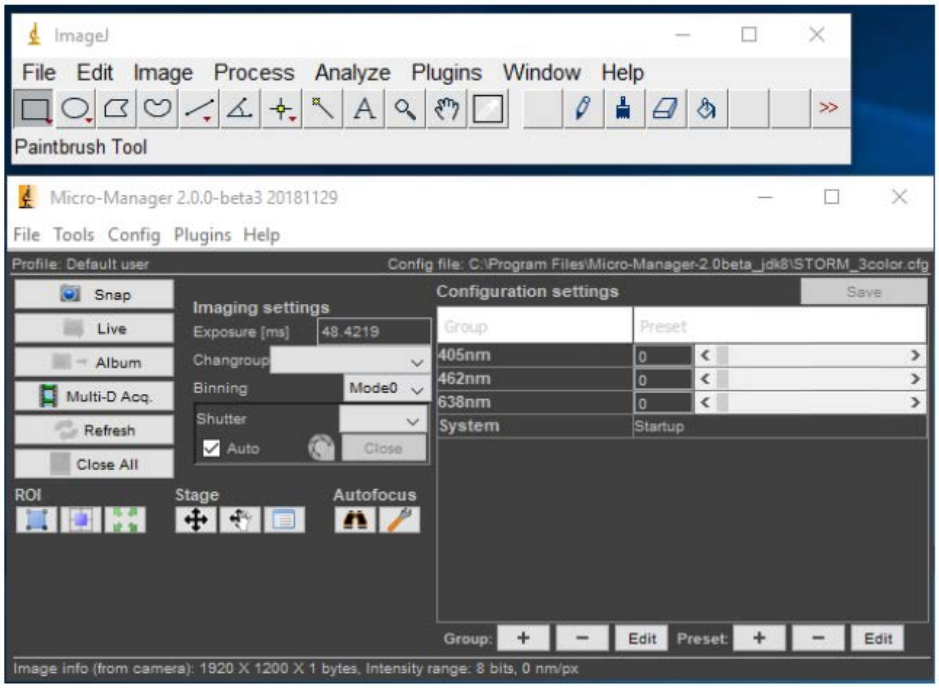

Figure 6.2: Screen shot of ImageJ with the μManager program.

for implementing low-cost STORM, we need industry grade lasers and cameras along with suitable software for capturing images and localization of fluorophores. Figure 6.1 illustrates the schematic diagram of the STORM setup with three excitation wavelengths. The three lasers having wavelengths 405 nm, 462 nm, and 638 nm are combined by appropriate dichroic mirrors after passing through the respective narrowband excitation filters. Then the combined excitation beam is delivered via a multimode optical fiber (MMF) to the inverted microscope (Olympus IX51) through the lenses L_2 and L_3 and reflected by a dichroic beam splitter (DBS) to provide a Köhler illumination at the sample plane. The fluorescence light from the sample is then collected by the same objective lens and transmitted by the dichroic beam splitter to be focused on the camera through the lens L_4. Powering on and off of the three lasers and their individual intensity levels are controlled via a java language based software μManager installed in the PC. The same software program also controls the acquisition of the camera. The detailed descriptions of the instrumentation of the STORM setup are provided in the following sections.

6.4.1 The μManager package

The μManager is an open source software package that comes together with ImageJ, which can be used for controlling automated microscopes. The μManager has a wide range of hardware support, and it can work with major microscope manufacturers such as Leica, Nikon, Olympus,

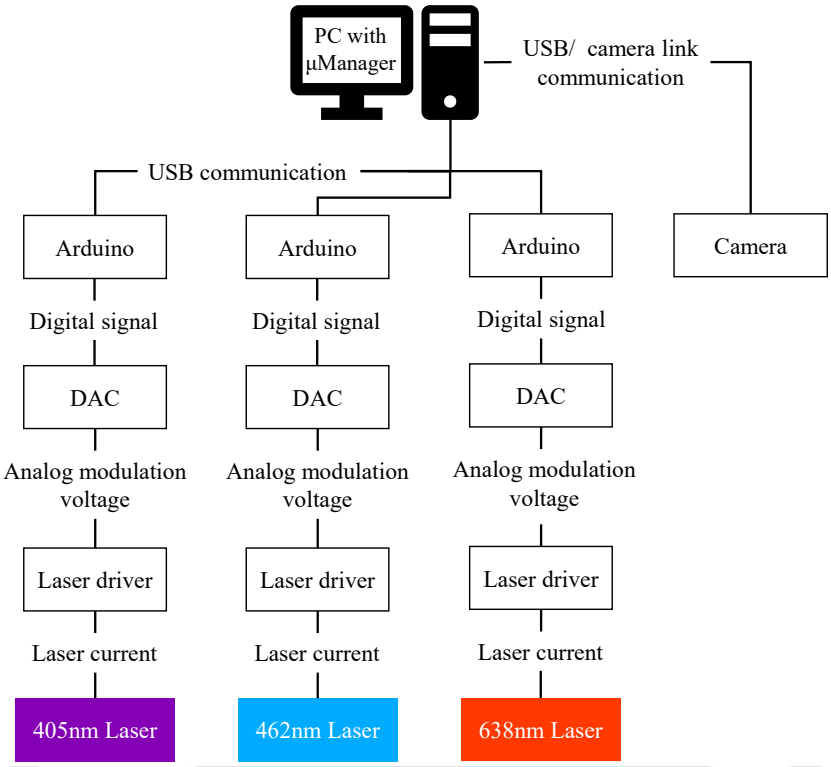

Figure 6.3: Hardware integration of lasers and cameras with μManager.

and Zeiss. It also supports most scientific-grade cameras and peripherals (such as stages, filter wheels, shutters, etc.) used in microscope based imaging. Being an open source software working in a java programming environment, we can custom build device adapters and user defined plugins for integration of hardware to μManager. In our setup we use the μManager package to execute common microscope image acquisition tasks [119, 120] such as time-lapses, multi-channel imaging, z-stacks, etc. We also integrate all the three lasers, the camera, and the microscope stage using a μManager program. Figure 6.2 shows a μManager program that is used to control both the lasers and a camera.

6.4.2 Integration of the lasers

We use diode lasers of make Lasertrack, having wavelengths 638 nm, 462 nm, and 405 nm with power equal to 700mW, 1.4W, and 350mW, respectively. Each diode laser is based on a linear regulator control unit operating as an analog driver, which provides a reliable laser current control with a temperature and interlock monitoring. The temperature monitoring system consists of a negative temperature coefficient (NTC) thermistors and a thermoelectric cooler (TEC) controller. The NTC is attached to the laser diode for temperature measurement of the

laser diode, while the TEC controller provides the temperature monitoring by thermoelectric cooling using a Peltier element. The interlock module triggers a safety shutdown of the laser output and can be used in an external interlock system for laser safety. The laser output will turn off within milliseconds if there is any temperature increase or interlock failure arises.

As the laser driver needs analog voltage for modulation of the laser output, so to generate such modulation voltage, we employ an Arduino board attached with a digital to analog converter (DAC) chip. The Arduino board is a programmable circuit I/O unit comprising digital inputs and digital outputs. The board communicates with the PC through a serial interface connection. It can be programmed with a simplified version of C++ language based code using Arduino IDE, which can be used to write and upload programs to the board. In order to connect the Arduino board to the μManager, a specific firmware needs to be uploaded to the board through the IDE. The firmware code facilitates the μManager to have control over the output of the DAC chip via the Arduino board. Here we use TLV5618, a 12-bit DAC chip (Make: Texas Instrument), which communicates with the Arduino board using a serial peripheral interface (SPI) protocol. After the hardware is connected to the Arduino, one needs to configure the device property of the Arduino board in the μManager, details of which are found in the “Hardware Configuration Wizard" section of the reference [121].

As we want to have independent control over the three lasers, we have to use three Arduino boards along with the DAC and three laser drivers each connected to the respective laser diode, as shown in Fig. 6.3.

Illumination beam path

The lasers we incorporate are multimode laser diodes, each with wide spectrum width. Thus to decrease the width of the spectrum, we employ narrow bandpass excitation filters along the path of laser output. In order to direct the three laser beams to the microscope along a single beam path, we need to arrange the three lasers in such a way that we can switch between lasers from μManager panel without requiring any mechanical movement of components. This is accomplished by employing a combination of mirrors and two dichroic beam combiners (DBC) in the path of the laser beams, as shown in Fig. 6.4. After the alignment of the three lasers, the beam is then focused onto a multimode fiber of 0.22 NA and 100 μm core diameter, using a fiber coupler adapter (FCA). Since the lasers used in the setup are class 4 lasers, so we enclose all the laser related components in a homemade laserbank, for safety. The output of the fiber from the laserbank is then collimated using a lens and focused onto the back focal plane of the objective lens, resulting in a collimated beam to illuminate the sample plane.

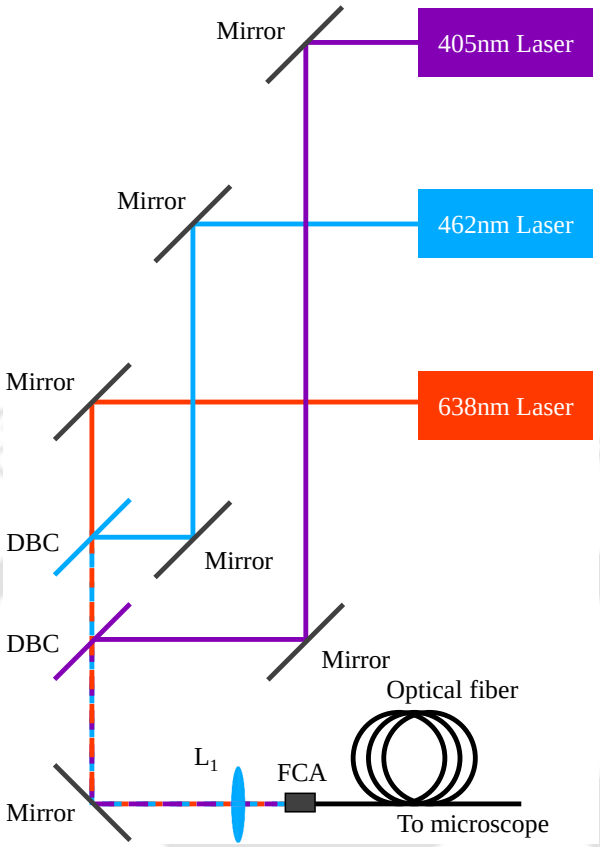

Figure 6.4: Schematic diagram of optics alignment inside the laserbank.

6.4.3 Single dichroic mirror for all the three excitation wavelengths

To differentiate the longer wavelength fluorescent light coming from the sample from the excitation light, we employ a dichroic filter cube containing a custom-made polychromatic beam splitter (PoBS) in conjunction with a suitable polychromatic emission filter. A PoBS is a specialized beam splitter designed to reflect multiple bands of wavelengths for fluorescence excitation while transmitting the corresponding fluorescence emissions from the sample. The transmission spectrum of the PoBS filter is shown in Fig. 6.5.

Cutoff wavelengths	Reflections	Transmission
405 *nm*, 462 *nm*, 635 *nm* and 830 *nm*	Below the cutoff	Above the cutoff

Table 6.1: Specification of polychromatic filters.

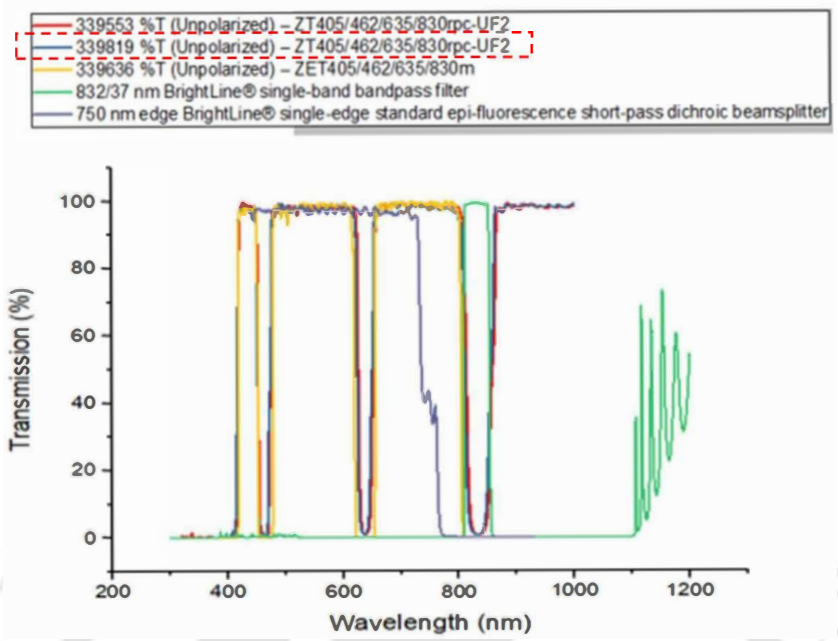

Figure 6.5: Spectral graph of the polychromatic filter (Image source: Chroma).

The table 6.1 shows the cutoff wavelengths of the single filter cube and the wavelength of the transmitted and reflected light.

6.4.4 Integration of the camera

Here we use FLIR GS3-U3-23S6M or Hamamatsu C11440-22C camera for capturing the widefield images. The technical specifications of the cameras are listed in table 3.3. The camera needs to be integrated into the μManager so that it can be configurable via the user program. It is to be noted that the μManager program cannot alone drive the camera, and for this, the PC must have the manufacturer's driver so that the camera is recognized by the PC. As seen in Fig. 6.3, the same μManager program controls both the three laser and the camera. In the first run of the μManager program, we need to integrate all the associated hardware using the configuration wizard utility (Tools $\rightarrow$ Hardware Configuration Wizard). The configuration wizard utility provides a workflow for creating and managing the configuration, and one can save the hardware configuration in a configuration file. The same configuration file can be loaded for the subsequent uses and also be modified for any changes in hardware configuration later. To view the properties of the device integrated with the μManager, we need to open the device property browser, which comes under the device menu. Figure 6.6 (i) shows the hardware configuration wizard linked to a specific configuration file which integrates the lasers and the camera whose properties are seen in Fig. 6.6 (ii).

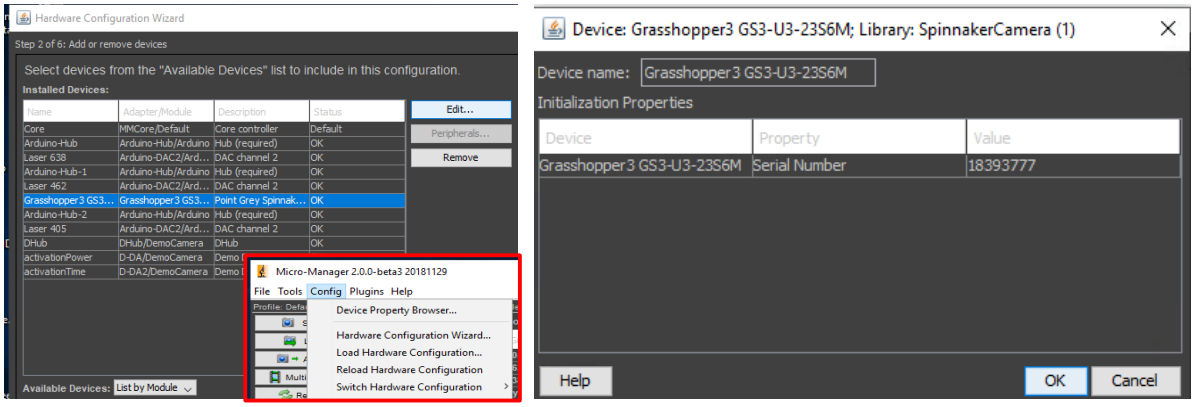

(i) (ii)

Figure 6.6: Screenshots of (i) Hardware configuration wizard of the μManager and (ii) the associated camera properties window.

Figure 6.7 (i), on the other hand, shows the control window of the μManager, which contains the basic operations like setting up camera exposure time, camera shutter, region of interest (ROI) selection tool, and so on which are the part of image settings. The same control window also has the laser settings. Another important feature of the μManager control panel is the multi-dimensional acquisition, in which we can acquire multi-channel (wavelength coordinate), multi-frame (time coordinate), multi-slice (Z coordinate), multi-position (XY coordinate) image stacks. In STORM, we generally use multi-frame and multi-channel image stacks. Figure 6.7 (ii) shows the snap/live window that can be opened by clicking the snap/live button in the control panel. It provides the live view of the camera corresponding to a specific configuration as provided in the control panel of the μManager. When we go to the live view of the sample, an image inspector tool, as shown in Fig. 6.7 (iii), automatically opens up along with the live view that can be used for adjusting and examining the image data. The image inspector tool is a versatile tool that can also provide image histogram and intensity scaling, dataset summary metadata information, and image plane information.

For capturing multi-channel image stacks for STORM, the device property and the working environment of the camera are chosen in such a way that it enables capturing all possible blinking events of the fluorophores with low thermal noise, high dynamical range, and fastest readout rate.

6.4.5 Sample preparation

Usually, the biological sample to be imaged by STORM is tagged with organic dye or genetically encoded fluorescent proteins. The occurrence of the blinking event through the acquisition period is made possible by employing reducing agents in the buffer. Organic dyes

(i)

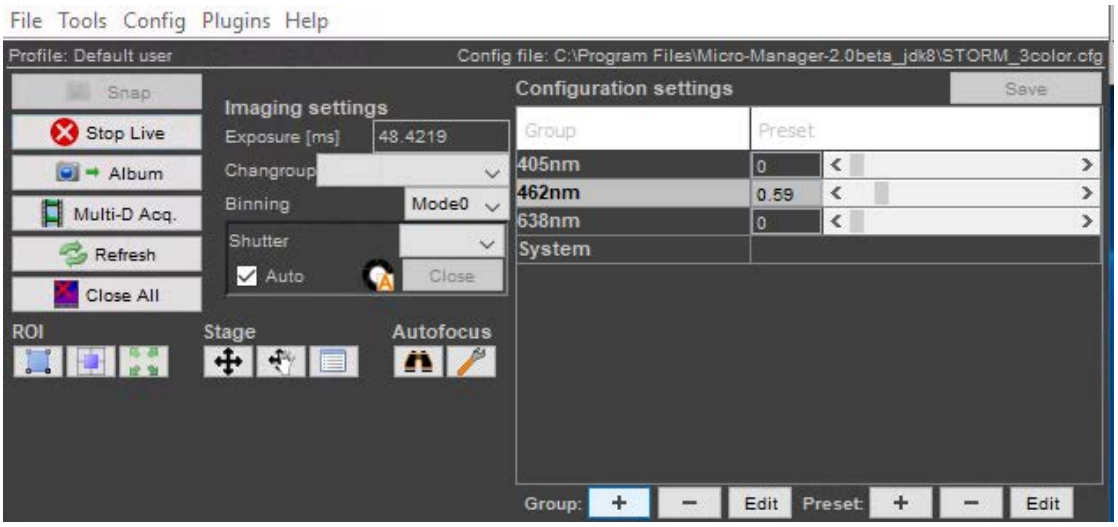

(ii)

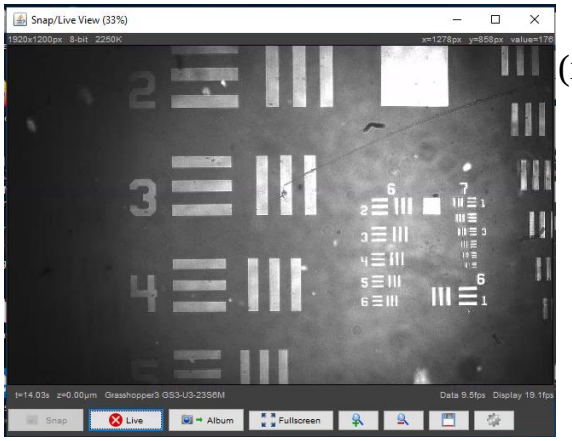

(iii)

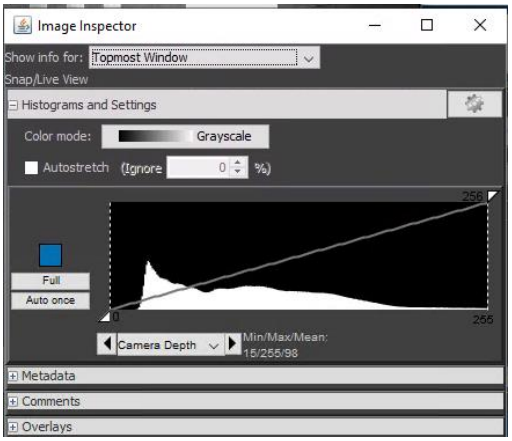

Figure 6.7: Screenshots of (i) image settings for the camera and configuration settings for the lasers, (ii) live view window for the camera, and (iii) the image inspector tool to adjust the displayed image.

are generally preferred for STORM imaging over the fluorescent proteins as the former emit more photons. The sample preparations for STORM include cell culture, cell seeding, STORM buffer preparation, cell fixation, immunostaining, and mounting. The details are given below in step wise

1. For STORM imaging, flat and large cells are nice as the actins and microtubules are prominent in a thin layer of cytoplasm.

2. A cover glass is placed in a well and pour 200μL of Poly-L-Lysine diluted in PBS to favor cell attachment and incubate at room temperature for 5 minutes.

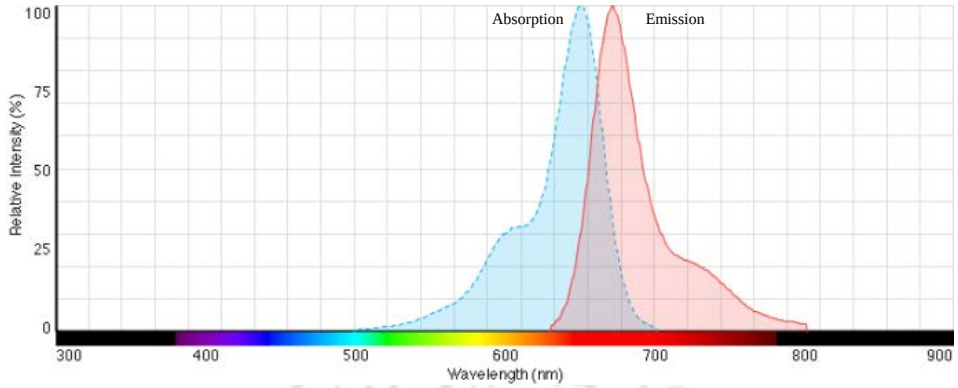

Figure 6.8: Absorption and emission spectra of Alexa Fluoro 647 phalloidin (Image source: Thermofisher).

3. Wash the coverslip three times with 500μL of PBS, and about 10,000 of Human embryonic kidney (HEK-293) cells are seeded in a complete culture medium.
4. The well containing the coverslip is incubated for 24 or 48 hours at 37°C with humidified atmosphere and 5% CO^2 for cell growth.
5. The media is removed from the well and wash it with 500μL of PBS.
6. 500μL of 4% paraformaldehyde is added in PBS to fix the cells at room temperature for 10 minutes.
7. The cells are washed with PBS-Triton 0.05% to remove paraformaldehyde.
8. Primary antibodies are added to the well after diluting with blocking solution and incubate at room temperature for 20 minutes.
9. The primary antibodies are incubated for one hour and then washed by PBS-Triton 0.05%.
10. Fluorescent labeled secondary antibodies (Alexa Fluoro 647 phalloidin) are added to the well after diluting with blocking solution by a factor of 1:2000 and incubate at room temperature for 20 minutes.
11. The secondary antibodies are removed and then washed by PBS-Triton 0.05%.
12. 100μL of the STORM buffer is placed on the top of the coverslip, and then the microscope slide is placed on the coverslip.
13. A slide is placed on the coverslip and sealed with silicone gel or nail polish so as to be able to preserve the sample for several days if required.

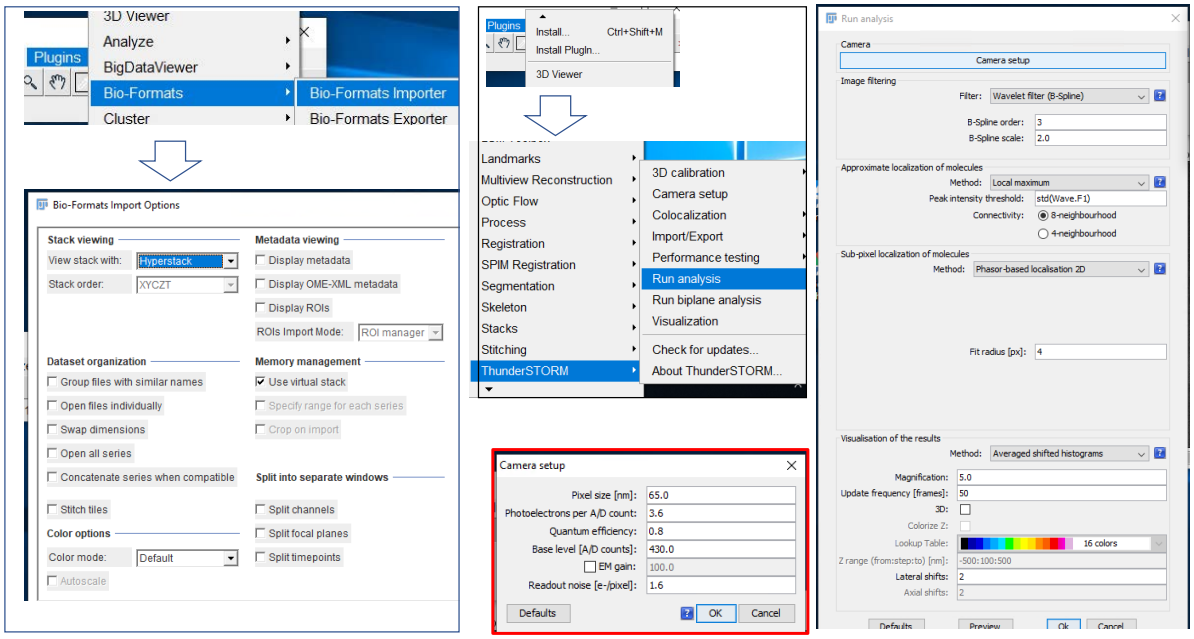

(i) (ii) (iii)

Figure 6.9: i) Importing the image stack to ImageJ using Bio-Formats importer. (ii) Run analysis tool of ThunderSTORM, and (iii) configuration of the tool including the camera setup (shown in the inset)

6.4.6 Reconstruction of super-resolved images

After the sample is placed in the microscope stage and brought into focus, the excitation laser power is increased until the stochastic blinking of molecules is observed. Afterward, the laser power is decreased, and a stack of images is captured at regular intervals. As described previously, in the localization microscopy technique, typically, a stack of 1000-50000 frames is acquired to determine the fluorophore positions. Each blinking event of a molecule is emitted about 10^6 number of photons, which is captured by the camera in presence of the background noise. The localization of the blinking events, namely locating the centers of the single molecule images, is done by fitting each image of the molecule with a 2D Gaussian function. The precision of the localization can be expressed as $\frac{\sigma}{\sqrt{N}}$, where σ is the standard deviation of the spatial response function of the imaging system to a point object and N is the total number of photons collected during a blinking event of a molecule [122].

After the acquisition, each frame of the stack undergoes a rigorous computation for localization of each blinking event. This task is carried out with the help of a complex mathematical code or by employing a suitable software. Several localization software packages are available, out of which we choose ThunderSTORM [123, 124]. The thunderSTORM software is an open source localization package written in java and distributed as a plugin of ImageJ. Since the

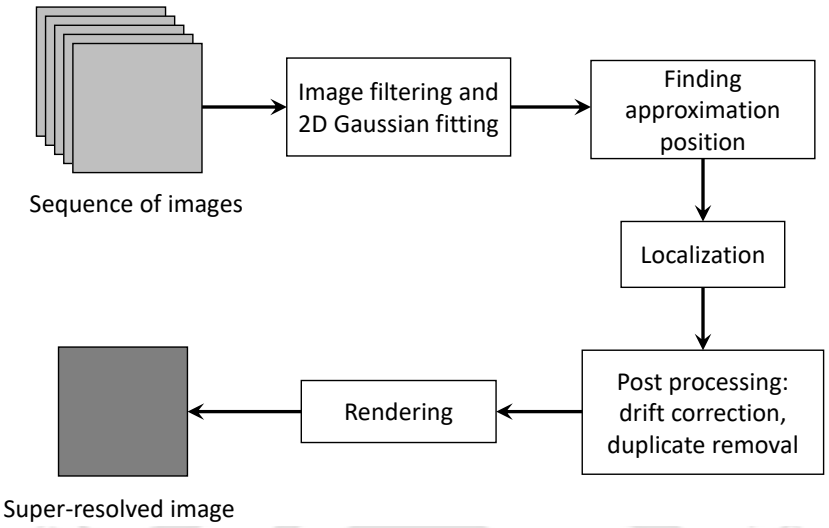

Figure 6.10: Flowchart diagram of the data processing for single molecule super-resolution imaging in ThunderSTORM.

image stack contains thousands of frames (having a net size of several gigabytes), so it is recommended to keep a decent memory size and a good processor to fulfill the computation demand. We employ a PC with an Intel i7 core processor with 16GB of RAM to run the ThunderSTORM to localize the blinking events. We can import the image stack for processing by ThunderSTORM using the Bio-Formats importer option, as shown in Fig. 6.9 (i). After the import, the Run analysis tool of ThunderSTORM, as shown in Fig. 6.9 (ii), is invoked. This is preceded by the setting of various localization parameters and the camera setup, as seen in Fig. 6.9 (iii) and in the inset.

The flowchart depicting the localization and reconstruction processes in the ThunderSTORM software is shown in Fig. 6.10. For the processing by ThunderSTORM, we first need to import the image stack in ImageJ software. After importing the image stack, we setup a number of parameters such as camera pixel size in the sample plane, the conversion factor between photons and digital units in the captured image, base level offset of the camera digitizer, and EM gain in the ThunderSTORM. Then one has to setup the image filtering parameter for band-pass filtering (Lowered Gaussian, Difference-of-Gaussians, Difference of averaging filters, or Wavelet B-Spline filter) of the images to achieve the best detection performance. On the other hand setting the 'approximate localization of molecules' helps to localize the blinking events in approximately 8 or 4 connected neighborhoods. The most important parameter to set is the 'Sub-pixel localization of molecules,' which helps to fit the blinking event to a 2D PSF model. In ThunderSTORM, several PSF models, namely, integrated Gaussian PSF, Gaussian PSF, Elliptical Gaussian PSF, Phasor based localization, and local maxima based localization, are available to fit the blinking events. The most recommended

method for sub-pixel localization is the integrated Gaussian, in which the blinking event is fitted with a 2D Gaussian function. Multiple emitter fitting analysis is used, in the case of high density data, to calculate the number of molecules fitted in a single Gaussian function.

Molecules having more than one blinking events, microscope instability, or longer image acquisition time can cause lateral drift, which significantly interferes with the localization of the molecules. Besides, in the process of capturing the stack of the image, sometimes a particular point on the sample remains bright throughout the acquisition process, which may lead to producing duplicates or artifacts in the super-resolved image. However, after completion of the processing by ThunderSTORM, the results are arranged in a tabular form, as shown in Fig. 6.11. The data comprises the number of total localizations, coordinates of each localization, intensities of the localized molecules, and uncertainty in the position of localized molecules. This data can be used for post processing and visualization of the super-resolved image. During the post processing, other corrections such as removal of the duplicates, filtering, and drift correction, arising out of the issues mentioned above, can also be carried out.

6.4.7 Proof-of-principle experimental results

In our proof-of-principle experiment, we acquire 20,000 frames of the sample. Figure 6.14 (i) shows the widefield image of the region of interest (ROI) of the sample. During the image acquisition process, one fluorescence-activated molecule can exhibit more than one blinking event, and it can stay in the ON state for a few milliseconds. Figure 6.12 shows a molecule which comes to ON state in the frame no. 1427 and stays in the ON state up to frame no. 1432. Thus it remains in the ON state for about 150 milliseconds before it goes to the OFF state. However, in a blinking event, a molecule can stay in the ON state for even a longer duration, such as the case shown in Fig. 6.13. In this case, the molecule remains in the ON state for about 500 ms.

We then import the stack of 20,000 images for processing by ThunderSTORM. The blinking events over the entire acquisition period have given rise to 386696 localizations. The final super-resolved image after drift correction and duplicate removal is shown in Fig. 6.14 (ii). A comparison of the widefield image with the super-resolved image clearly shows the significant resolution enhancement in the latter image. Nevertheless, to highlight the amount of lateral resolution enhancement, we extract a portion of each image at the same location and draw a line plot as shown in Fig. 6.14 (iii)(c).

This clearly shows that in the super-resolved image the finer details of the fluorophore distribution can be observed which cannot be observed in the widefield image due to the diffraction phenomenon.

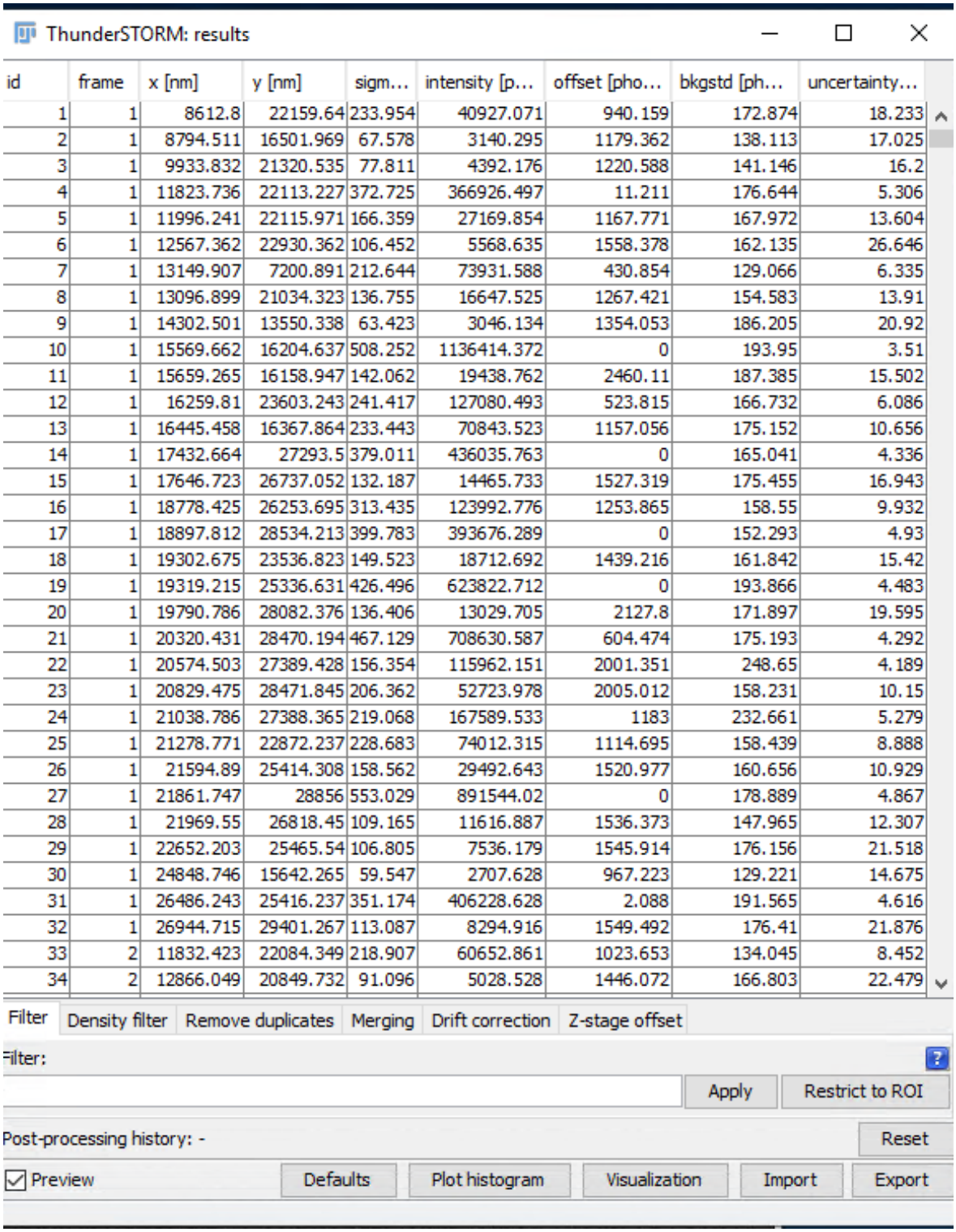

id	frame	x [nm]	y [nm]	sigm...	intensity [p...	offset [pho...	bkgstd [ph...	uncertainty...
1	1	8612.8	22159.64	233.954	40927.071	940.159	172.874	18.233
2	1	8794.511	16501.969	67.578	3140.295	1179.362	138.113	17.025
3	1	9933.832	21320.535	77.811	4392.176	1220.588	141.146	16.2
4	1	11823.736	22113.227	372.725	366926.497	11.211	176.644	5.306
5	1	11996.241	22115.971	166.359	27169.854	1167.771	167.972	13.604
6	1	12567.362	22930.362	106.452	5568.635	1558.378	162.135	26.646
7	1	13149.907	7200.891	212.644	73931.588	430.854	129.066	6.335
8	1	13096.899	21034.323	136.755	16647.525	1267.421	154.583	13.91
9	1	14302.501	13550.338	63.423	3046.134	1354.053	186.205	20.92
10	1	15569.662	16204.637	508.252	1136414.372	0	193.95	3.51
11	1	15659.265	16158.947	142.062	19438.762	2460.11	187.385	15.502
12	1	16259.81	23603.243	241.417	127080.493	523.815	166.732	6.086
13	1	16445.458	16367.864	233.443	70843.523	1157.056	175.152	10.656
14	1	17432.664	27293.5	379.011	436035.763	0	165.041	4.336
15	1	17646.723	26737.052	132.187	14465.733	1527.319	175.455	16.943
16	1	18778.425	26253.695	313.435	123992.776	1253.865	158.55	9.932
17	1	18897.812	28534.213	399.783	393676.289	0	152.293	4.93
18	1	19302.675	23536.823	149.523	18712.692	1439.216	161.842	15.42
19	1	19319.215	25336.631	426.496	623822.712	0	193.866	4.483
20	1	19790.786	28082.376	136.406	13029.705	2127.8	171.897	19.595
21	1	20320.431	28470.194	467.129	708630.587	604.474	175.193	4.292
22	1	20574.503	27389.428	156.354	115962.151	2001.351	248.65	4.189
23	1	20829.475	28471.845	206.362	52723.978	2005.012	158.231	10.15
24	1	21038.786	27388.365	219.068	167589.533	1183	232.661	5.279
25	1	21278.771	22872.237	228.683	74012.315	1114.695	158.439	8.888
26	1	21594.89	25414.308	158.562	29492.643	1520.977	160.656	10.929
27	1	21861.747	28856	553.029	891544.02	0	178.889	4.867
28	1	21969.55	26818.45	109.165	11616.887	1536.373	147.965	12.307
29	1	22652.203	25465.54	106.805	7536.179	1545.914	176.156	21.518
30	1	24848.746	15642.265	59.547	2707.628	967.223	129.221	14.675
31	1	26486.243	25416.237	351.174	406228.628	2.088	191.565	4.616
32	1	26944.715	29401.267	113.087	8294.916	1549.492	176.41	21.876
33	2	11832.423	22084.349	218.907	60652.861	1023.653	134.045	8.452
34	2	12866.049	20849.732	91.096	5028.528	1446.072	166.803	22.479

Figure 6.11: ThunderSTORM results in tabular form.

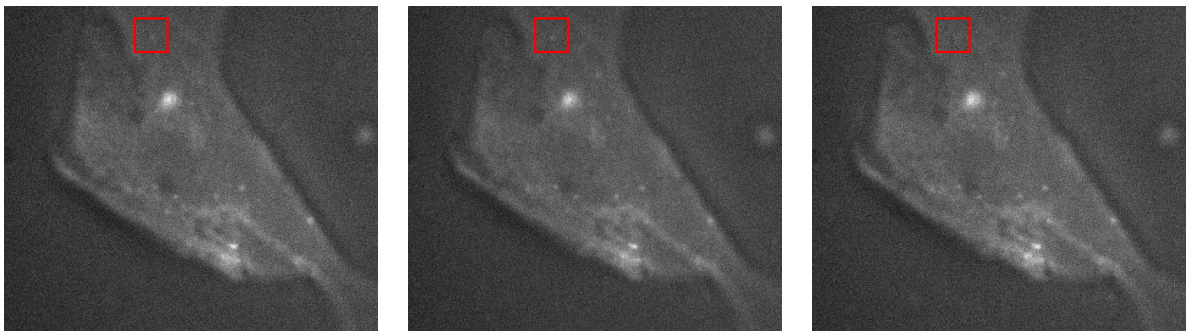

(i) (ii) (iii)

Figure 6.12: Image frames (i), (ii) and (iii) showing a blinking event of a molecule lasting up to 150 ms second. The blinking molecule is marked by a red solid box as shown in figure.

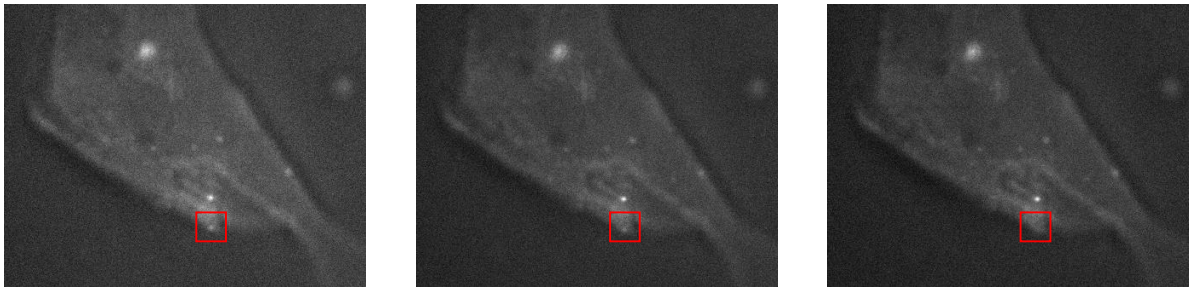

(i) (ii) (iii)

Figure 6.13: Image frames (i), (ii) and (iii) showing a blinking event of a molecule lasting up to 0.5 second. The blinking molecule is marked by a red solid box as shown in figure.

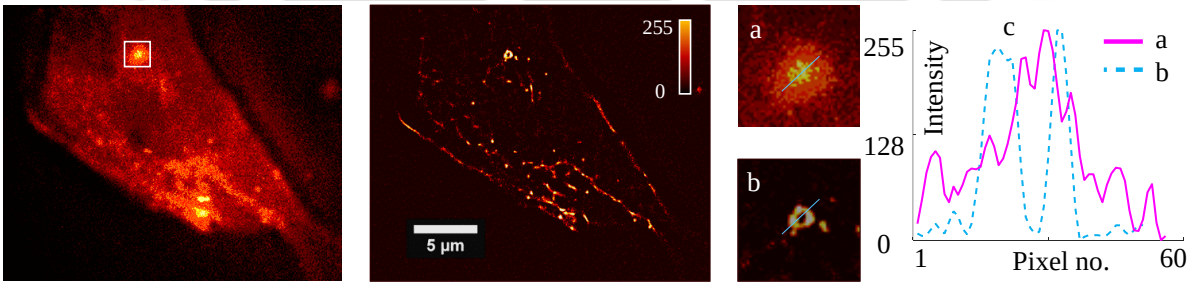

(i) (ii) (iii)

Figure 6.14: (i) Widefield, (ii) STORM image of human embryonic kidney (HEK293) cells and (iii) (a) magnified view of a portion of the widefield image, and the corresponding (b) STORM image, and (c) line plots along the solid line as shown in (a) and (b).

6.5 Integration of the array detection microscope with the STORM

In the array detection microscopy, the resolution of the image can be improved by digital post-processing, as there is extra information about the focal point recorded by the array. For

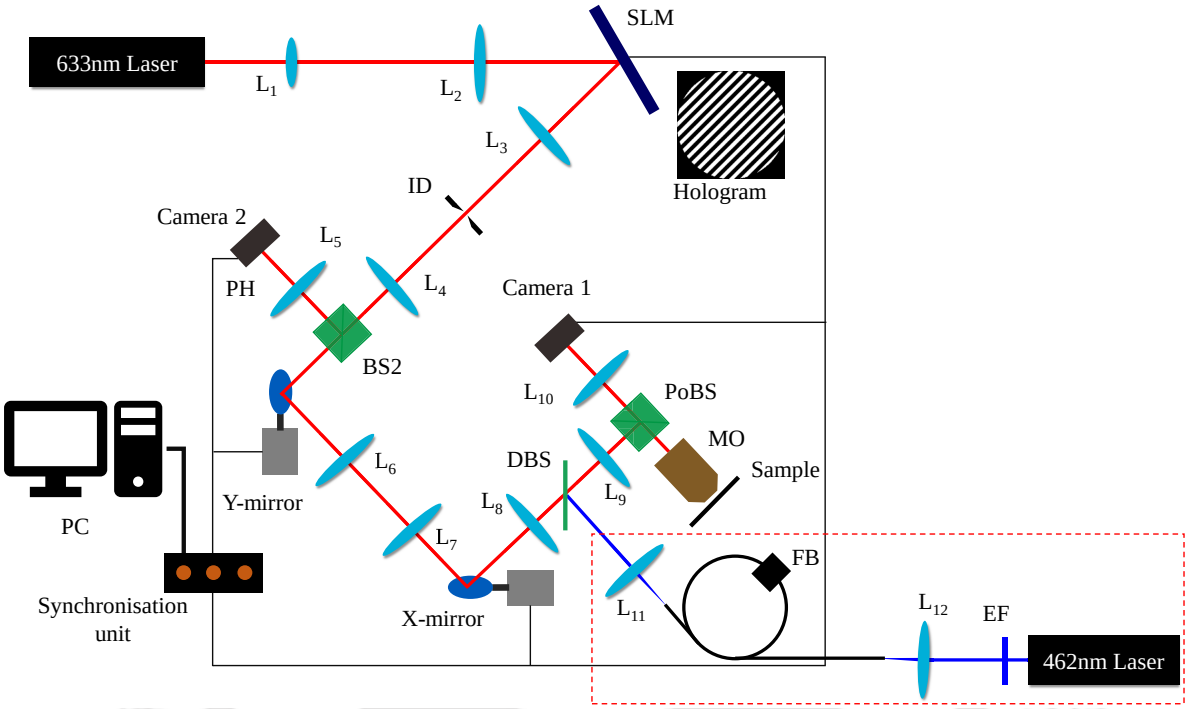

Figure 6.15: Schematic diagram of the proposed setup combining STORM with the galvanometer based array detection microscope.

samples with weak signal levels, shot noise is the fundamental problem in the conventional scanning microscope with a detector pinhole. However, using the array detector, the effect of shot noise in the image can be discarded as it is deficient compared to the signal captured by the array detector. On the other hand, STORM provides high spatial resolution, which can identify the protein movement inside the cell in nanometer scale. Here we propose a single experimental arrangement where a single sample can be imaged by both the STORM system and the array detection microscope. As we have already developed these two systems separately, we only need to combine both the system with appropriate illumination and detection beam paths using the same microscope stage. Here we take the 633 nm laser for our galvanometer based array detection microscope and the 462 nm laser for the STORM. However, we can use other than these two particular wavelengths provided suitable filter sets are available. Figure 6.15 shows the schematic diagram of the proposed experimental setup.

We employ one DBS and one PoBS for combining the two illumination wavelengths into a single beam to enter the microscope stage. The arrangement of the two beam splitters is shown in Fig. 6.16. The DBS with a cutoff wavelength $\lambda_c = 540nm$ reflects the 462 nm wavelength laser and transmits the laser with 633 nm wavelength. The beams then travel along the same path towards the filter cube mounted inside the microscope, in which the PoBS, along

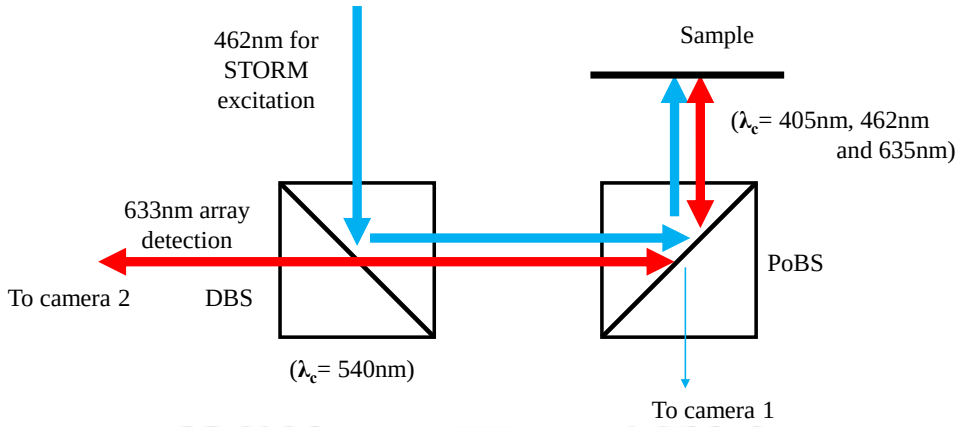

Figure 6.16: Illumination and detection beam paths for array detection microscopy and STORM.

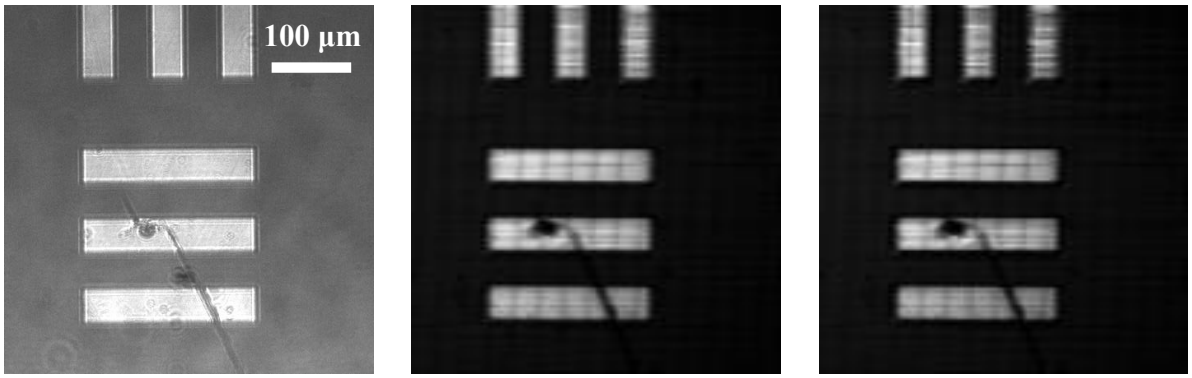

(i) (ii) (iii)

Figure 6.17: (i) Widefield image obtained using the STORM setup with 462 nm illumination, and respective (ii) confocal image and (iii) Image subtraction microscopy image using the array detection microscope with 633 nm illumination.

with a polychromatic emission filter is mounted. As mentioned already, the PoBS has cutoff wavelengths $\lambda_c = 405nm, 462nm, and 635nm$. Therefore both the lasers get reflected by the filter cube to illuminate the sample at the microscope stage. For reflected light microscopy, the 633 nm laser is collected by the objective lens and reflected by the PoBS towards the DBS. After getting transmitted by the DBS, this beam then enters the camera 2. For the STORM imaging, the fluorescent light from the sample gets transmitted by the PoBS and detected by the camera 1 mounted on the microscope stage.

6.5.1 Proof-of-principle experiment

Insofar as the accuracy of the experimental setup is concerned, we in fact, need to show that the same sample can be imaged by both the widefield microscope, which is used for STORM, and the array detection microscope. Therefore we decided to take the USAF 1951 test target as the common sample and use a 10 $\times$ objective lens. We employ our array detection microscope to acquire the 4D image data of a portion of the USAF 1951 test target using reflected light and 633 nm illumination. The portion of the target being imaged has a physical dimension of about 460 μm $\times$ 460 μm. We also acquire the widefield image the same portion of the USAF 1951 test target using the 462 nm illumination. To be noted that the filter tube with the PoBS is designed for imaging using fluorescence light only. Where the wavelength from the sample plane is greater than the cutoff wavelength of the PoBS, nevertheless, a very small amount (about 0.1 %) of the reflected light from the sample plane can still be transmitted and thus reach the detector to construct the widefield image of the sample. Figure 6.15 (i) shows the widefield image of the target. We employ the 4D image data from our array detection microscope to implement both confocal microscopy and image subtraction microscopy. Figures 6.17 (ii) and (iii) show the confocal image and their respective image subtraction microscopy image of the target.

6.6 Summary

In this chapter, we have implemented a cost effective yet a robust version of the STORM system. The implementation includes the installation of the lasers and the camera and integrating them using a single μManage program. We have demonstrated the performance of our STORM system in a proof-of-principle experiment. We have then integrated our galvo mirror based array detection microscope with the STORM system to enable reflected light imaging using the array detection microscope and widefield imaging of the same sample. We have demonstrated the accuracy of our combined system by imaging a test target in the reflection mode. Even though in our combined system we have used our array detection microscope in the reflection mode, with the availability of the proper dichroic beam splitters it will be possible to use the array detection microscope also in the fluorescence mode.

CHAPTER 7

Conclusion and future prospects

7.1 Conclusion

In conclusion, optical microscopy provides the far-field imaging capability which becomes particularly useful for biological applications, in contrast to other microscopy techniques. An optical microscope can be primarily of two types, namely, the widefield microscope and the point scanning microscope. The point scanning microscope facilitates the use of lasers as the illumination beam to implement various user-defined beam profiles. The parameter that decides the amount of finer details that can be available in an image captured by an optical microscope is the resolution. The resolution of an optical microscope on the other hand has an upper limit owing to the diffraction phenomenon. Use of confocal pinhole in a point scanning microscope enables capturing of images with significantly higher axial resolution. Such a point scanning microscope is called confocal microscope. Resolution performance of the confocal microscope improves more and more as one decreases the diameter of the pinhole in front of the detector. However reducing the diameter of the pinhole decreases the signal-to-noise ratio in the image. Use of an array detector in a beam scanning microscope facilitates implementation of novel imaging schemes such as image scanning microscopy technique. Image scanning microscopy is shown to provide superior lateral resolution compared to a confocal microscope without compromising the signal-to-noise ratio. However to set up an array detection microscope there are certain crucial requirements. For instance during the acquisition by the array detector the illumination beam is supposed to be steady with respect to the detector plane. Moreover there should be an appropriate synchronisation between the movement of the beam and the image capturing process of the camera, which acts as the array detector. These requirements often slow down the scanning speed of the array detection microscope.

In this thesis we have implemented an array detection microscope that uses either a galvanometer based beam scanning scheme or a holographic beam scanning scheme. We have configured the galvanometer based beam scanner in conjunction with a high speed camera in such a way that the array detection microscope can image without compromising on the other performance parameters. We have also implemented another version of an array detection microscope where we have exploited holographic beam scanning and a low speed camera to image without compromising significantly on the imaging speed. We have employed the four dimensional image data that is obtained from the array detection microscope to implement various resolution enhancement scheme such as image scanning microscopy for lateral resolution enhancement and image subtraction microscopy for axial resolution enhancement. We have also implemented confocal imaging with variable pinhole size so that one can establish a balance the resolution and the signal level requirements. Besides we have employed our array detection microscope to implement a novel intensity subtraction microscopy technique where the axial resolution can be enhanced without introducing artifacts that can be present in the image subtraction microscopic technique. We have introduced a point spread function estimation scheme using which we can quantify the resolution enhancements in our various imaging systems in terms of the corresponding imaging point spread functions. We have built a stochastic optical reconstruction microscope (STORM) comprising three excitation lasers which can provide super-resolved images of biological samples. We have then integrated the STORM setup with our array detection microscope so that the same sample can be imaged by the widefield microscope for super-resolved imaging and the array detection microscope.

Below we provide a chapter wise summary of the entire thesis work.

- Chapter 1: This chapter has provided a general introduction to the research problem and an overview of the thesis.
- Chapter 2: In this chapter we have introduced the optical microscope and various important optical microscopy techniques. We have discussed the theory of image formation and developed the same to define the resolution limit in an optical microscopes. We have done a review of the recent developments related to the enhancements of the resolution in an optical microscope. We have ended the chapter with a discussion on some of the existing issues connected with the various resolution enhancement techniques and how this thesis proposes to address some of these issues.
- Chapter 3: In this chapter we have discussed the basic principle of classical holography and computer-generated holography. We have discussed how binary holograms can generate a beam with user defined phase profile. We have elaborated the properties of liquid crystal spatial light modulator and how they can implement binary hologram.

We have showed that such binary holograms can be used as the illumination beam in scanning optical microscopes. We have then discussed the implementation of a proof of principle scanning optical microscope that uses the galvanometer based or holographic beam scanning scheme.

- Chapter 4: In this chapter, we have introduced a PSF estimation scheme based on minimizing the least square error between the image of a target, whose geometrical-optics predicted image, I_{gop}, can be constructed, and the image obtained by convolving the I_{gop} with a stochastically constructed PSF. We have demonstrated the working of the proposed scheme first on numerically constructed targets. We have then experimentally demonstrated the working of the proposed scheme in widefield and confocal microscopes.

- Chapter 5: In this chapter we have developed two types of scanning optical microscope using array detector, one using galvo scan mirrors and the other using holographic scanning. In the array detection microscope using scan mirrors we have addressed the stability issue of the scan mirrors by configuring the scanners and synchronising their movement with the camera. In the other system we have performed the beam scanning without using any mechanical scanner by utilising the fast response liquid crystal spatial light modulator and an ordinary camera. We have employed our array detection microscopes to implement various imaging schemes such as confocal microscopy with variable pinhole size, image scanning microscopy and image subtraction microscopy. Implementation of variable pinhole size in a confocal microscope facilitates confocal imaging with appropriate balance of lateral resolution and signal-to-noise ratio. Our proof-of-principle experiments using the image scanning microscope technique has demonstrated enhancement in lateral resolution in both the reflection and fluorescence modes. We have also introduced a novel intensity subtraction microscopic technique. Both the image subtraction microscopy and the novel intensity subtraction microscopy techniques enhance the axial resolution by reducing the amount of background light. In contrast to the image subtraction microscopy technique, in our novel intensity subtraction microscopy technique some of the artifacts in the reconstructed image can be avoided. We have performed a numerical investigation on the lateral resolution enhancement as achieved by the various imaging techniques implemented, using our PSF estimation scheme.

- Chapter 6: In this chapter we have implemented a cost effective yet a robust version of the STORM system. We have demonstrated the performance of our STORM system in a proof-of-principle experiment. We have then integrated our galvanometer based array detection microscope with the STORM system to enable reflected light imaging

using array detection microscope and widefield imaging of the same sample. We have demonstrated the accuracy of our combined system by imaging a test target in the reflection mode.

- Chapter 7: In this chapter, we have provided a summary of the research work carried out. We have also provided a discussion on the future works in connection with the imaging systems developed in this thesis.

7.2 Future prospects

The research work presented in this thesis can be further extended by incorporating a number of tasks. Below we briefly explain some of such tasks.

- In this thesis we have designed and configured the mechanism of the galvanometer based scanner in conjunction with the high speed camera for array detection microscopy. At present our configuration parameters are not optimised. However the high speed camera that we have used can provide much higher frame rate. One can easily modify or tune the configuration parameters to achieve the optimised imaging speed using our proposed scheme.

- In our holographic scanning based system we have used a camera frame rate of only 15 frames per second. This system can be upgraded by using an ordinary yet a higher frame camera such as a commonly available scientific camera providing a frame rate upto 60 fps.

- We have employed our array detection microscopes to implement image scanning microscope and image subtraction microscope which provide lateral resolution enhancement and axial resolution enhancement, respectively. It will be there for interesting to investigate how these two schemes can be integrated so that both lateral and axial resolutions can be enhanced in the same reconstructed image.

- We have integrated our STORM setup with the array detection microscope working in the reflection mode. However using an appropriate dichroic beam splitter it will be possible to combine the STORM with an array detection microscope working both in the reflection as well as in the fluorescence mode.

APPENDIX A

Zernike polynomials

The Zernike polynomials are well known for expressing classical aberration of optical systems. Here we use single indexed Zernike polynomial over a unit circle for describing different classical aberrations [67]. The detailed mathematical expression in Cartesian coordinates along with the aberration names are given in table A.1.

j	$Z_j(x,y)$	Aberration Name
4	$2\sqrt{3}(2(x^2+y^2)-1)$	Defocus
5	$2\sqrt{6}xy$	Primary Astigmatism at $\pm$ 45°
6	$\sqrt{6}(x^2-y^2)$	Primary Astigmatism at $\pm$ 0°
7	$\sqrt{8}(3(x^2+y^2)-2)y$	Primary x- coma
8	$\sqrt{8}(3(x^2+y^2)-2)x$	Primary y- coma
9	$\sqrt{8}(3x^2y-y^3)$	Primary x- trefoil
10	$\sqrt{8}(x^3-3xy^2)$	Primary y- trefoil
11	$\sqrt{5}(6(x^2+y^2)^2-6(x^2+y^2)^2+1)x$	Primary spherical aberration

Table A.1: Single indexed Zernike polynomials for some monochromatic aberrations.

APPENDIX B

Employment of microprocessor circuit board for trigger signal generation

We have employed a PIC18F2550 microcontroller manufactured from Microchip, which has 28 pins with a 10-bit ADC resolution. To program a PIC microcontroller, we need several programming software and hardware components such as an in-circuit debugger/programmer, an integrated development environment (IDE), a compiler and an integrated programming environment (IPE). We have used an MPLAB ICD2 in-circuit debugger/programmer for transferring the application program to the microcontroller. An IDE is used to converts the code written in C language for the application into program commands, and the compiler converts the program commands into microcontroller assembly language called HEX files. After the generation of the HEX file, the IPE transfers the file into the PIC microcontroller [125]. By using the programming environment, we used to generate different trigger signal for camera, scanner and data acquisition system. The Fig. B.1 shows the schematic circuit diagram of microchip board.

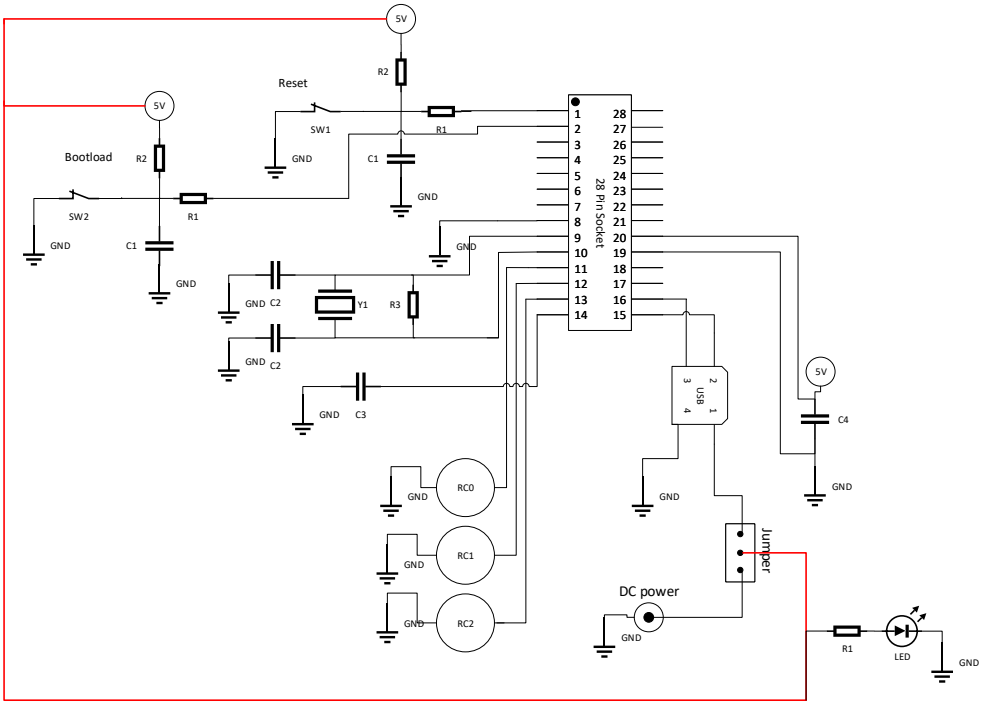

28-Pin PDIP, SOIC

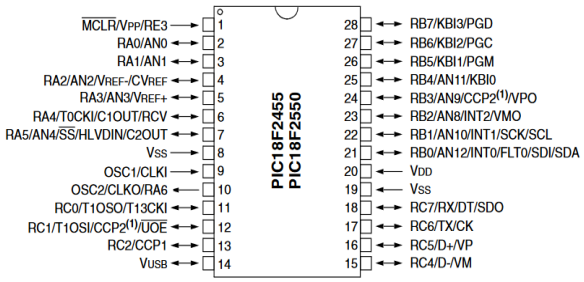

R1: 470Ω (RS Part No: RK73B1HTTC471J)
R2: 10KΩ (RS Part No: RK73B1HTTC103J)
R3: 1MΩ (RS Part No: RK73B1HTTC105J)
C1: 100nF (RS Part No: C1206X104K3GECAUTO)
C2: 22pF (RS Part No: 06033J220GBSTR)
C3: 470nF (RS Part No: GRM21BB11E474KA01L)
C4: 10uF (RS Part No: GRM21BR61E106MA73L)
Y1: 20MHz Crystal Oscillator
(RS Part No: 20.000MHZ MJ2/30/30/-40+85/12PF)
USB: USB type B female (RS Part No: 09455411900)
RB0,RB1,RB2,RB3,RB4,RB5,RB6,RB7,RC0,RC1,RC2,RA4,RA5: BNC female connector (RS Part No: B6251C1-NT3G-75)
SW1,SW2: Push Button (RS Part No: TSSL 3 W RG)
Molex Pin: Molex Header (RS Part No: B3P-VH(LF)(SN))
28 pin socket: Microchip socket (RS Part No: AR 28 HZL/7-TT)
8 pin socket: Microchip socket (RS Part No: AR 08 HZL-TT)
Jumper: 3 pin 1 row jumper header (RS Part No: M20-9990346)
DC Power: DC Power Socket female (RS Stock No: 448-382)

E-commerce site: https://in.rsdelivers.com

Figure B.1: Microprocessor circuit board.

References

[1] Jerome Mertz. *Introduction to optical microscopy*. Cambridge University Press, 2019. 1, 7

[2] Michael W Davidson and Mortimer Abramowitz. Optical microscopy. *Encyclopedia of imaging science and technology*, 2002.

[3] Min Gu. *Advanced optical imaging theory*, volume 75. Springer Science & Business Media, 2000. 1

[4] Tony Wilson, Colin Sheppard, and Harcourt Brace Jovanovich. *Theory and practice of scanning optical microscopy*, volume 180. Academic Press London, 1984. 1, 11, 14

[5] RC Reddick, RJ Warmack, and TL Ferrell. New form of scanning optical microscopy. *Physical Review B*, 39(1):767, 1989.

[6] Gordon S Kino and Timothy R Corle. *Confocal scanning optical microscopy and related imaging systems*. Academic Press, 1996. 2

[7] David M Shotton. Confocal scanning optical microscopy and its applications for biological specimens. *Journal of Cell Science*, 94(2):175–206, 1989.

[8] Robert H Webb. Confocal optical microscopy. *Reports on Progress in Physics*, 59(3):427, 1996. 1

[9] Brian Matsumoto. *Cell biological applications of confocal microscopy*. Elsevier, 2003. 1

[10] Nan Yao and Zhong Lin Wang. *Handbook of microscopy for nanotechnology*. Springer, 2005. 1

[11] Karl-Jürgen Halbhuber and Karsten König. Modern laser scanning microscopy in biology, biotechnology and medicine. *Annals of Anatomy-Anatomischer Anzeiger*, 185(1):1–20, 2003. 1

[12] Robert Allen Carlton. *Pharmaceutical microscopy*. Springer Science & Business Media, 2011. 1

[13] Joseph W Goodman. *Introduction to Fourier optics*. Roberts and Company Publishers, 2005. 1, 11, 12, 45

[14] Max Born and Emil Wolf. *Principles of optics: electromagnetic theory of propagation, interference and diffraction of light*. CUP Archive, 2000. 1, 15

[15] Wes Wallace, Lutz H Schaefer, and Jason R Swedlow. A workingperson's guide to deconvolution in light microscopy. *Biotechniques*, 31(5):1076–1097, 2001. 2

[16] Yoshimasa Kawata and Wataru Inami. *High-Resolution Optical Microscopy for Biological Applications*, pages 407–427. Springer Netherlands, Dordrecht, 2017. 2

[17] Jeroen Vangindertael, R Camacho, W Sempels, H Mizuno, P Dedecker, and KPF Janssen. An introduction to optical super-resolution microscopy for the adventurous biologist. *Methods and applications in fluorescence*, 6(2):022003, 2018. 21

[18] Yuval Garini, Bart J Vermolen, and Ian T Young. From micro to nano: recent advances in high-resolution microscopy. *Current opinion in biotechnology*, 16(1):3–12, 2005. 2

[19] James Pawley. *Handbook of biological confocal microscopy*, volume 236. Springer Science & Business Media, 2006. 2

[20] C Sheppard. Super-resolution in confocal microscopy. *Optik*, 80:53–54, 1988. 2, 17, 66

[21] Claus B Müller and Jörg Enderlein. Image scanning microscopy. *Physical review letters*, 104(19):198101, 2010. 2, 18, 22, 66

[22] Colin JR Sheppard, Shalin B Mehta, and Rainer Heintzmann. Superresolution by image scanning microscopy using pixel reassignment. *Optics letters*, 38(15):2889–2892, 2013. 2, 18, 22

[23] Mark AA Neil, Rimas Juškaitis, and Tony Wilson. Method of obtaining optical sectioning by using structured light in a conventional microscope. *Optics letters*, 22(24):1905–1907, 1997. 3

[24] Mats GL Gustafsson. Surpassing the lateral resolution limit by a factor of two using structured illumination microscopy. *Journal of microscopy*, 198(2):82–87, 2000. 3, 19, 20

[25] Stefan W Hell and Jan Wichmann. Breaking the diffraction resolution limit by stimulated emission: stimulated-emission-depletion fluorescence microscopy. *Optics letters*, 19(11):780–782, 1994. 3, 18

[26] Michael J Rust, Mark Bates, and Xiaowei Zhuang. Sub-diffraction-limit imaging by stochastic optical reconstruction microscopy (storm). *Nature methods*, 3(10):793–796, 2006. 3

[27] Edward N Ward and Robert Pal. Image scanning microscopy: an overview. *Journal of microscopy*, 266(2):221–228, 2017. 3, 18

[28] Ingo Gregor and Jörg Enderlein. Image scanning microscopy. *Current opinion in chemical biology*, 51:74–83, 2019. 3, 22

[29] Johnny Tam and David Merino. Stochastic optical reconstruction microscopy (storm) in comparison with stimulated emission depletion (sted) and other imaging methods. *Journal of neurochemistry*, 135(4):643–658, 2015. 4

[30] DB Murphy and MW Davidson. *Fundamentals of light microscopy and electronic imaging*. Oxford [et.]: Wiley-Blackwell, 2013. 7

[31] Minsky Marvin. Microscopy apparatus, December 19 1961. US Patent 3,013,467. 9

[32] Tony Wilson. The role of the pinhole in confocal imaging system. In *Handbook of biological confocal microscopy*, pages 167–182. Springer, 1995. 9

[33] Enrico Gratton et al. Laser sources for confocal microscopy. In *Handbook of biological confocal microscopy*, pages 69–97. Springer, 1995. 9

[34] Joseph R Lakowicz. *Principles of fluorescence spectroscopy*. Springer science & business media, 2013. 13

[35] C. J. R. Sheppard and T. Wilson. Depth of field in the scanning microscope. *Opt. Lett.*, 3(3):115–117, Sep 1978. 15

[36] O Scherzer. The theoretical resolution limit of the electron microscope. *Journal of Applied Physics*, 20(1):20–29, 1949. 16

[37] Stanley L Flegler and Stanley L Flegler. *Scanning & Transmission Electron Microscopy*. Oxford University Press, 1997. 16

[38] Erik Meijering, Oleh Dzyubachyk, Ihor Smal, and Wiggert A van Cappellen. Tracking in cell and developmental biology. In *Seminars in cell & developmental biology*, volume 20, pages 894–902. Elsevier, 2009. 16

[39] Juan R Perilla, Boon Chong Goh, C Keith Cassidy, Bo Liu, Rafael C Bernardi, Till Rudack, Hang Yu, Zhe Wu, and Klaus Schulten. Molecular dynamics simulations of large macromolecular complexes. *Current opinion in structural biology*, 31:64–74, 2015.

[40] Utpalendu Kuila and Manika Prasad. Specific surface area and pore-size distribution in clays and shales. *Geophysical Prospecting*, 61(Rock Physics for Reservoir Exploration, Characterisation and Monitoring):341–362, 2013.

[41] Filippo Benetti, M Fedel, Luca Minati, Giorgio Speranza, and C Migliaresi. Gold nanoparticles: role of size and surface chemistry on blood protein adsorption. *Journal of nanoparticle research*, 15(6):1694, 2013. 16

[42] Colin JR Sheppard and CJ Cogswell. Confocal microscopy with detector arrays. *Journal of Modern Optics*, 37(2):267–279, 1990. 17

[43] Olaf Schulz, Christoph Pieper, Michaela Clever, Janine Pfaff, Aike Ruhlandt, Ralph H Kehlenbach, Fred S Wouters, Jörg Großhans, Gertrude Bunt, and Jörg Enderlein. Resolution doubling in fluorescence microscopy with confocal spinning-disk image scanning microscopy. *Proceedings of the National Academy of Sciences*, 110(52):21000–21005, 2013. 18

[44] Ingo Gregor, Martin Spiecker, Roman Petrovsky, Jörg Großhans, Robert Ros, and Jörg Enderlein. Rapid nonlinear image scanning microscopy. *Nature methods*, 14(11):1087, 2017. 18

[45] Uri Rossman, Ron Tenne, Oren Solomon, Ifat Kaplan-Ashiri, Tali Dadosh, Yonina C Eldar, and Dan Oron. Rapid quantum image scanning microscopy by joint sparse reconstruction. *Optica*, 6(10):1290–1296, 2019.

[46] Marco Castello, Giorgio Tortarolo, Mauro Buttafava, Takahiro Deguchi, Federica Villa, Sami Koho, Luca Pesce, Michele Oneto, Simone Pelicci, Luca Lanzanó, et al. A robust and versatile platform for image scanning microscopy enabling super-resolution flim. *Nature methods*, 16(2):175–178, 2019. 18, 22

[47] Katrin I Willig, Silvio O Rizzoli, Volker Westphal, Reinhard Jahn, and Stefan W Hell. Sted microscopy reveals that synaptotagmin remains clustered after synaptic vesicle exocytosis. *Nature*, 440(7086):935–939, 2006. 19

[48] Rainer Heintzmann and Gabriella Ficz. Breaking the resolution limit in light microscopy. *Briefings in Functional Genomics*, 5(4):289–301, 2006. 19

[49] Fabian Göttfert, Christian A Wurm, Veronika Mueller, Sebastian Berning, Volker C Cordes, Alf Honigmann, and Stefan W Hell. Coaligned dual-channel sted nanoscopy and molecular diffusion analysis at 20 nm resolution. *Biophysical journal*, 105(1):L01–L03, 2013.

[50] KI Willig, J Keller, M Bossi, and SW Hell. Sted microscopy resolves nanoparticle assemblies. *New Journal of Physics*, 8(6):106, 2006. 19

[51] M. A. A. Neil, R. Juškaitis, and T. Wilson. Method of obtaining optical sectioning by using structured light in a conventional microscope. *Opt. Lett.*, 22(24):1905–1907, Dec 1997. 19

[52] Lothar Schermelleh, Rainer Heintzmann, and Heinrich Leonhardt. A guide to super-resolution fluorescence microscopy. *The Journal of cell biology*, 190(2):165–175, 2010. 19

[53] Travis J Gould, Vladislav V Verkhusha, and Samuel T Hess. Imaging biological structures with fluorescence photoactivation localization microscopy. *Nature protocols*, 4(3):291–308, 2009. 20

[54] Alexander Egner, Claudia Geisler, Claas Von Middendorff, Hannes Bock, Dirk Wenzel, Rebecca Medda, Martin Andresen, Andre C Stiel, Stefan Jakobs, Christian Eggeling, et al. Fluorescence nanoscopy in whole cells by asynchronous localization of photoswitching emitters. *Biophysical journal*, 93(9):3285–3290, 2007. 21

[55] BR Boruah. Lateral resolution enhancement in confocal microscopy by vectorial aperture engineering. *Applied optics*, 49(4):701–707, 2010. 22

[56] Peter TC So, Hyuk-Sang Kwon, and Chen Y Dong. Resolution enhancement in standing-wave total internal reflection microscopy: a point-spread-function engineering approach. *JOSA A*, 18(11):2833–2845, 2001.

[57] BR Boruah. Dynamic manipulation of a laser beam using a liquid crystal spatial light modulator. *American Journal of Physics*, 77(4):331–336, 2009. 22, 27

[58] Peiwen Meng, Silvania Pereira, and Paul Urbach. Confocal microscopy with a radially polarized focused beam. *Optics express*, 26(23):29600–29613, 2018. 22

[59] Yuichi Kozawa, Terumasa Hibi, Aya Sato, Hibiki Horanai, Makoto Kurihara, Nobuyuki Hashimoto, Hiroyuki Yokoyama, Tomomi Nemoto, and Shunichi Sato. Lateral resolution enhancement of laser scanning microscopy by a higher-order radially polarized mode beam. *Optics express*, 19(17):15947–15954, 2011. 22

[60] T Wilson and AR Carlini. Three-dimensional imaging in confocal imaging systems with finite sized detectors. *Journal of microscopy*, 149(1):51–66, 1988. 22

[61] Colin JR Sheppard, Min Gu, and Maitreyee Roy. Signal-to-noise ratio in confocal microscope systems. *Journal of Microscopy*, 168(3):209–218, 1992.

[62] Colin JR Sheppard, Xiaosong Gan, Min Gu, and Maitreyee Roy. Signal-to-noise in confocal microscopes. In *Handbook of biological confocal microscopy*, pages 363–371. Springer, 1995. 22

[63] Siwei Li, Jingjing Wu, Heng Li, Danying Lin, Bin Yu, and Junle Qu. Rapid 3d image scanning microscopy with multi-spot excitation and double-helix point spread function detection. *Optics express*, 26(18):23585–23593, 2018. 22

[64] Wei Zhang, Bin Yu, Danying Lin, Huanhuan Yu, Siwei Li, and Junle Qu. Optimized approach for optical sectioning enhancement in multifocal structured illumination microscopy. *Optics Express*, 28(8):10919–10927, 2020. 22

[65] Omer Tzang, Dan Feldkhun, Anurag Agrawal, Alexander Jesacher, and Rafael Piestun. Two-photon psf-engineered image scanning microscopy. *Optics Letters*, 44(4):895–898, 2019. 22

[66] BR Brown and AW Lohmann. Computer-generated binary holograms. *IBM Journal of research and Development*, 13(2):160–168, 1969. 27

[67] Robert J Noll. Zernike polynomials and atmospheric turbulence. *JOsA*, 66(3):207–211, 1976. 29, 56, 103

[68] Virendra N Mahajan. Zernike circle polynomials and optical aberrations of systems with circular pupils. *Applied optics*, 33(34):8121–8124, 1994. 29

[69] Yasunori Igasaki, Fanghong Li, Narihiro Yoshida, Haruyoshi Toyoda, Takashi Inoue, Naohisa Mukohzaka, Yuji Kobayashi, and Tsutomu Hara. High efficiency electrically-addressable phase-only spatial light modulator. *Optical Review*, 6(4):339–344, 1999. 30

[70] Rodney L Clark. Optically addressed spatial light modulator and method, November 25 1997. US Patent 5,691,836. 30

[71] John A Neff, Ravinda A Athale, and Sing H Lee. Two-dimensional spatial light modulators: a tutorial. *Proceedings of the IEEE*, 78(5):826–855, 1990. 30

[72] Jae-Hyuk Park, H Takagi, K Nishimura, H Uchida, M Inoue, Jae-Hak Park, and Jae-Kyeong Cho. Magneto-optic spatial light modulators driven by an electric field. *Journal of applied physics*, 93(10):8525–8527, 2003. 30

[73] Larry J Hornbeck. Deformable-mirror spatial light modulators. In *Spatial Light Modulators and Applications III*, volume 1150, pages 86–103. International Society for Optics and Photonics, 1990. 30

[74] TSUNG-YUAN Hsu, Uzi Efron, WY Wu, JN Schulman, IJ D'Haenens, and Yia-Chung Chang. Multiple quantum well spatial light modulators for optical processing applications. *Optical Engineering*, 27(5):275372, 1988. 30

[75] B Senyuk. Liquid crystals: a simple view on a complex matter. *Liquid Crystal Institute, Kent State Univeristy*, 2011. 30

[76] Michael Bass, Casimer DeCusatis, Jay Enoch, Vasudevan Lakshminarayanan, Guifang Li, Carolyn Macdonald, Virendra Mahajan, and Eric Van Stryland. *Handbook of optics, Volume II: Design, fabrication and testing, sources and detectors, radiometry and photometry*. McGraw-Hill, Inc., 2009. 30

[77] Uzi Efron. *Spatial light modulator technology: materials, devices, and applications*, volume 47. CRC press, 1994. 31

[78] HOLOEYE Photonics AG. *LC-R 720 Spatial Light Modulator- Operating instruction and application software manual*, Oct 2005. 31

[79] HOLOEYE Photonics AG. *LC-R 1080 Spatial Light Modulator- Device operating instruction and application software instruction manual*, Nov 2012. 31

[80] FORTH DIMENSION DISPLAY. *Quick start guide to SXGA-R2D-H1-H2 microdisplay systems*, Dec 2011. 33

[81] FORTH DIMENSION DISPLAY. *SXprog software user guide for SXGA-R2 systems*, Mar 2010. 33

[82] James Pawley. *Handbook of biological confocal microscopy*. Springer Science & Business Media, 2010. 33

[83] Aaron Lewis and Klony Lieberman. Flat scanning stage for scanned probe microscopy, January 6 1998. US Patent 5,705,878. 33

[84] Hiroshi Miyajima, Kenzi Murakami, and Masahiro Katashiro. Mems optical scanners for microscopes. *IEEE Journal of Selected Topics in Quantum Electronics*, 10(3):514–527, 2004. 33

[85] Sven TS Holmström, Utku Baran, and Hakan Urey. Mems laser scanners: a review. *Journal of Microelectromechanical Systems*, 23(2):259–275, 2014. 33

[86] Gaddum D Reddy and Peter Saggau. Fast three-dimensional laser scanning scheme using acousto-optic deflectors. *Journal of biomedical optics*, 10(6):064038, 2005. 33

[87] GRBE Römera and P Bechtoldb. Electro-optic and acousto-optic laser beam scanners-invited paper. *Physics procedia*, 56:29–39, 2014. 33

[88] DP Resler, DS Hobbs, RC Sharp, LJ Friedman, and TA Dorschner. High-efficiency liquid-crystal optical phased-array beam steering. *Optics letters*, 21(9):689–691, 1996. 33

[89] Sanghoon Choi, Pilhan Kim, R Boutilier, Min Young Kim, YJ Lee, and Ho Lee. Development of a high speed laser scanning confocal microscope with an acquisition rate up to 200 frames per second. *Optics express*, 21(20):23611–23618, 2013. 34

[90] Jihwan Kim, Chulwoo Oh, Michael J Escuti, and Steve Serati. Wide-angle nonmechanical beam steering using thin liquid crystal polarization gratings. In *Advanced Wavefront Control: Methods, Devices, and Applications VI*, volume 7093, page 709302. International Society for Optics and Photonics, 2008. 34

[91] Redmond P Aylward. Advanced galvanometer-based optical scanner design. *Sensor review*, 2003. 35

[92] Cambridge Technology Inc. *MicroMax 671 Series board level single axis driver electronics*, July 2008. 35

[93] Cambridge Technology Inc. *Model 6231H Galvanometer Optical Scanner Instruction Manual*, Sep 2004. 35

[94] Olof Bryngdahl and Wai-Hon Lee. Laser beam scanning using computer-generated holograms. *Applied optics*, 15(1):183–194, 1976. 37

[95] Xinghua Wang, Bin Wang, John Pouch, Felix Miranda, Michael Fisch, James E Anderson, Vassili Sergan, and Philip J Bos. Liquid crystal on silicon (lcos) wavefront corrector and beam steerer. In *Advanced Wavefront Control: Methods, Devices, and Applications*, volume 5162, pages 139–146. International Society for Optics and Photonics, 2003. 37

[96] Ranjan Kalita, S S Goutam Buddha, and Bosanta R Boruah. Suitability of holographic beam scanning in high resolution applications. In *Three-Dimensional and Multidimensional Microscopy: Image Acquisition and Processing XXV*, volume 10499, page 104991P. International Society for Optics and Photonics, 2018. 37

[97] Abhijit Das and Bosanta R Boruah. Optical sectioning microscope with a binary hologram based beam scanning. *Review of Scientific Instruments*, 82(4):043702, 2011. 37, 56

[98] R Rottenfusser, E. E. Wilson, and W. Davidson M. Microscope objectives- http://zeiss-campus.magnet.fsu.edu/articles/basics/objectives.html. 40

[99] Basler AG. *Basler A630f User Manual*, Dec 2010. 40

[100] Basler AG. *Basler A500k Series User Manual*, Aug 2003.

[101] Hamamatsu Photonics K.K. *FLIR Grasshopper USB 3 Vision Technical Reference*, Jan 2017.

[102] Hamamatsu Photonics K.K. *Hamamatsu DIgital Camera C11440-22C Instruction Manual*, July 2012. 40

[103] Satya S Goutam Buddha and Bosanta R Boruah. Estimation of point spread function of an optical microscope using stochastic minimization of least square errors. *Journal of Optics*, 22(5):055603, 2020. 46

[104] S S Goutam Buddha, Ranjan Kalita, and Bosanta R Boruah. Estimation of point spread function of an imaging system using a programmable target. In *Three-Dimensional and Multidimensional Microscopy: Image Acquisition and Processing XXV*, volume 10499, page 104991O. International Society for Optics and Photonics, 2018.

[105] S S Goutam Buddha and Bosanta R Boruah. A system and method for determining point spread function of an imaging system, March 2020. Application No.: 202031014419. 46

[106] Ioannis Pitas. *Digital image processing algorithms and applications*. John Wiley & Sons, 2000. 53

[107] Ranjan Kalita, Anindita Saikia, AC Bhuyan, and Bosanta R Boruah. Holographic scanning confocal microscopy for both reflected light and fluorescence light imaging. *Review of Scientific Instruments*, 90(10):106103, 2019. 56

[108] Satya S Goutam Buddha, Ranjan Kalita, and Bosanta R Boruah. Array detection in a holographic scanning microscope. *Optics Communications*, 462:125339, 2020. 61

[109] SS Goutam Buddha, Ranjan Kalita, and Bosanta R Boruah. Optical sectioning microscopy with both mechanical and non-mechanical beam scanning mechanisms. In *2019 Workshop on Recent Advances in Photonics (WRAP)*, pages 1–3. IEEE, 2019. 63

[110] SS Goutam Buddha and Bosanta R Boruah. Signal to noise ratio enhancement in confocal microscope with an array detector. In *2019 Workshop on Recent Advances in Photonics (WRAP)*, pages 1–3. IEEE, 2019. 63

[111] Rafael C Gonzalez, Richard Eugene Woods, and Steven L Eddins. *Digital image processing using MATLAB*. Pearson Education India, 2004. 64

[112] Yifan Wang, Cuifang Kuang, Zhaotai Gu, and Xu Liu. Image subtraction method for improving lateral resolution and snr in confocal microscopy. *Optics & Laser Technology*, 48:489–494, 2013. 70

[113] Kwasi Kwakwa, Alexander Savell, Timothy Davies, Ian Munro, Simona Parrinello, Marco A Purbhoo, Chris Dunsby, Mark AA Neil, and Paul MW French. easystorm: a robust, lower-cost approach to localisation and tirf microscopy. *Journal of Biophotonics*, 9(9):948–957, 2016. 79

[114] Jonas Fölling, Mariano Bossi, Hannes Bock, Rebecca Medda, Christian A Wurm, Birka Hein, Stefan Jakobs, Christian Eggeling, and Stefan W Hell. Fluorescence nanoscopy by ground-state depletion and single-molecule return. *Nature methods*, 5(11):943–945, 2008. 79

[115] Ellen Jensen and David J Crossman. Technical review: Types of imaging—direct storm. *The Anatomical Record*, 297(12):2227–2231, 2014. 80

[116] Thorge Holm, Teresa Klein, Anna Löschberger, Tobias Klamp, Gerd Wiebusch, Sebastian van de Linde, and Markus Sauer. A blueprint for cost-efficient localization microscopy. *ChemPhysChem*, 15(4):651–654, 2014. 80

[117] Robin Diekmann, Katharina Till, Marcel Müller, Matthias Simonis, Mark Schüttpelz, and Thomas Huser. Characterization of an industry-grade cmos camera well suited for single molecule localization microscopy–high performance super-resolution at low cost. *Scientific reports*, 7(1):1–10, 2017. 80

[118] John R Allen, Stephen T Ross, and Michael W Davidson. Sample preparation for single molecule localization microscopy. *Physical Chemistry Chemical Physics*, 15(43):18771–18783, 2013. 81

[119] Arthur Edelstein, Nenad Amodaj, Karl Hoover, Ron Vale, and Nico Stuurman. Computer control of microscopes using μmanager. *Current protocols in molecular biology*, 92(1):14–20, 2010. 83

[120] Arthur D Edelstein, Mark A Tsuchida, Nenad Amodaj, Henry Pinkard, Ronald D Vale, and Nico Stuurman. Advanced methods of microscope control using μmanager software. *Journal of biological methods*, 1(2), 2014. 83

[121] Nico Stuurman. Adapter for the arduino electronics prototyping platform. 84

[122] Russell E Thompson, Daniel R Larson, and Watt W Webb. Precise nanometer localization analysis for individual fluorescent probes. *Biophysical journal*, 82(5):2775–2783, 2002. 90

[123] Daniel Sage, Hagai Kirshner, Thomas Pengo, Nico Stuurman, Junhong Min, Suliana Manley, and Michael Unser. Quantitative evaluation of software packages for single-molecule localization microscopy. *Nature methods*, 12(8):717–724, 2015. 90

[124] Martin Ovesnỳ, Pavel Křížek, Josef Borkovec, Zdeněk Švindrych, and Guy M Hagen. Thunderstorm: a comprehensive imagej plug-in for palm and storm data analysis and super-resolution imaging. *Bioinformatics*, 30(16):2389–2390, 2014. 90

[125] Microchip. *Microchip PIC18F2455/2550/4455/4550 Data Sheet*, 2006. 105

List of publications and scientific activities

Patents

1. **S S Goutam Buddha** and B R Boruah, "A system and method for determining Point Spread Function of an imaging system" , Indian Patent Application No.: 202031014419, 31 March 2020. [1]

2. Ranjan Kalita, **S S Goutam Buddha** and B R Boruah, "A system and method for laser beam scanning with periodic switching of polarization of the beam", Indian Patent Application No.: 201831006652, 21 Feb 2018.

Journals

1. **S S Goutam Buddha** et al., "Integrating the EasySTORM with the image scanning microscope", manuscript under preparation. [1]

2. **S S Goutam Buddha**, and Bosanta R. Boruah, "Enhancement of axial resolution in a scanning optical microscope using an optimized pinhole radius", manuscript under preparation. [1]

3. **S S Goutam Buddha** and Bosanta R. Boruah, "Estimation of point spread function of an optical microscope using stochastic minimization of least square errors", Journal of Optics (IOP): 22(5) 055603 (2020).[1]

4. **S S Goutam Buddha**, Ranjan Kalita and Bosanta R. Boruah, "Array detection in a holographic scanning microscope", Optics Communications: 462, 125339 (2020).[1]

[1] N.B. Publications are included in the thesis

5. Ranjan Kalita, **S S Goutam Buddha** and Bosanta R. Boruah, "A laser scanning microscope executing intraframe polarization switching of the illumination beam ", Review of Scientific Instruments: 89(9), 093705 (2018).

Conference proceedings

1. Karuna Sindhu Malik, **S S Goutam Buddha**, Ranjan Kalita, Bosanta R Boruah, " Estimation of maximum translation speed of a trapped particle in holographic optical tweezers " Proceedings of SPIE : 11297 112970Z, 2020

2. **S S Goutam Buddha** and Bosanta R. Boruah, "Signal to noise ratio enhancement in confocal microscope with an array detector", IEEE Xplore, Advances in Photonics (WRAP) : 1-3, 2019 [1]

3. **S S Goutam Buddha**, Ranjan Kalita and Bosanta R. Boruah, "Optical sectioning microscopy with both mechanical and non-mechanical beam scanning mechanisms", IEEE Xplore, Advances in Photonics (WRAP) : 1-3, 2019. [1]

4. Ranjan Kalita, **S S Goutam Buddha**, Bosanta R Boruah, "Laser scanning confocal microscopy using illumination beams with different polarizations in quick succession " Proceedings of SPIE : 104772 107720I, 2018.

5. **S S Goutam Buddha**, Ranjan Kalita, and Bosanta R. Boruah, "Estimation of point spread function of an imaging system using a programmable target", Proc. SPIE, 10499, 104991O (2018). [1]

6. Ranjan Kalita, **S S Goutam Buddha**, and Bosanta R. Boruah, "Suitability of holographic beam scanning in high resolution applications ", Proc. SPIE, 10499, 104991P (2018).

Conference attended

1. "Implementation of a low-cost localization microscope", in the "FCS 2020, A National Workshop on Fluorescence And Raman Spectroscopy ", organised by IIT Bombay, Mumbai in virtual mode, during Dec 7-12, 2020.

2. "Signal to noise ratio enhancement in confocal microscope with an array detector", in the "IEEE Workshop on Recent Advances in Photonics (WRAP) 2019", organised by Department of Physics, IIT Guwahati at IIT Guwahati, Guwahati, during Dec 13 - 14, 2019.

3. “Optical sectioning microscopy with both mechanical and non-mechanical beam scanning mechanisms”, in the “IEEE Workshop on Recent Advances in Photonics (WRAP) 2019”, organised by Department of Physics, IIT Guwahati at IIT Guwahati, Guwahati, during Dec 13 - 14, 2019.

4. “Effect of Aberration on Resolution in an Optical Scanning Microscope”, in the “Photonics 2018, The International Conference on Fiber Optics and Photonics”, organized by Indian Institute of Technology Delhi, New Delhi at IIT Delhi, during December 12 - 15 2018.

5. “Development of a standalone confocal imaging system with CGH based as well as galvanometer scanner based beam scanning mechanism”, in the “Research Conclave - 2018”, organized by Students’ Academic Board (SAB), Indian Institute of Technology Guwahati at IIT Guwahati, during March 08 - 11, 2018.

6. “Suitability of holographic beam scanning in high resolution applications”, in the “SPIE Photonics West 2018”, organised by SPIE at San Francisco, California, USA, during Jan 27 - Feb 01, 2018,

7. “Estimation of point spread function of an imaging system using a programmable target”, in the “SPIE Photonics West 2018”, organised by SPIE at San Francisco, California, USA, during Jan 27 - Feb 01, 2018,

8. “Development of a Scanning Optical Microscope with a Holographically Designed Illumination Beam ” in the “International conference on advances in optics and photonics (ICAOP - 2017)”, organized jointly by Guru Jambheshwar University of Science & Technology and Optical Society of India at Guru Jambheshwar University of Science & Technology, Hisar, during November 23 - 26, 2017.

9. “Confocal microscopy and its applications” in the “Research Conclave - 2017”, organized by Students’ Academic Board (SAB), Indian Institute of Technology Guwahati at IIT Guwahati, Guwahati, during March 17 - 19, 2017.

10. “Confocal microscopy and its applications” in the “Department Day - 2017”, organized by Department of Physics, Indian Institute of Technology Guwahati at IIT Guwahati, Guwahati, on January 28, 2017.

11. “Imaging linear dichroism in a laser scanning confocal microscope” in the “Research Conclave - 2016”, organized by Students’ Academic Board (SAB), Indian Institute of Technology Guwahati at IIT Guwahati, Guwahati, during, March 18 - 20, 2016)

12. "Investigation of Beam Stability in a Galvanometer Based Scanning Mirror System" in the "International conference on light and light based technologies (ICLLT - 2016)", organized jointly by Tezpur University and Optical Society of India at Tezpur University, Tezpur, during November 26 - 28, 2016.

Workshops/ Schools attended

1. "One-Day workshop on Introduction to MATLAB", organized by SPIE IIT Guwahati Student Chapter at IIT Guwahati, Guwahati, on August 10, 2019.
2. "Patent writing and copyright workshop", at the Research Conclave 2018, held on 8-11 March 2018 organised by Students' Academic Board in association with IIT Guwahati.
3. "One-Day workshop on vacuum technology and its application in optical Science", jointly organized by SPIE IIT Guwahati Student Chapter and Pfeiffer Vacuum in association with Dept. of Physics, IIT Guwahati at IIT Guwahati, Guwahati, on August 19, 2017.
4. "Advanced microscopy and imaging techniques", jointly organized by DSS imagetech Pvt. Ltd., Olympus medical systems India Pvt. Ltd. and supported by Indian Institute of Technology Guwahati at IIT Guwahati, Guwahati, during, April 18 - 20, 2017.
5. "Intra IIT Latex Workshop", jointly organized by Research Scholar Forum Mathematics, and Student Academic Board, IIT Guwahati at IIT Guwahati on February 18 2017.
6. "3rd IEEE workshop on Advanced MATLAB Applications – ADMAT 2016" , organized by IEEE Student Branch, IIT Guwahati at IIT Guwahati, Guwahati, during, October 01 - 02, 2016.
7. DST-SERB School on "Modern Optics & Its Applications", organized by Indian Institute of Technology Patna (IITP), Bihar at IIT Patna, Patna, during, November 30 - December 18, 2015.
8. "South Asian Workshop on Optics & Photonics (SAWOP – 2015)", organized by Department of Physics, IIT Guwahati at IIT Guwahati, Guwahati, on November 17 - 18, 2015.
9. "IEEE Workshop on Power, Mechatronics, Robotics and Control" (PMRC 2015), organized by IEEE student branch IIT Guwahati and National Instruments at IIT Guwahati, Guwahati, during August 29 - 30, 2015.

Awards & Achievements

1. Received a grant of GBP 2000 for visiting Imperial College, London as a part of the open Scope project funded by the Imperial College Global Challenge Research Fund for implementing a low-cost super resolution microscope.

2. Received second best poster for the paper entitled *"Development of a standalone confocal imaging system with CGH based as well as galvanometer scanner based beam scanning Mechanism"*, at the Research Conclave 2018, held on 8-11 March 2018 organised by Students' Academic Board in association with IIT Guwahati.

3. Received "SPIE Student Officer Travel Grant" (USD 2910) to attend "SPIE Photonics West -2018" at San Francisco, California, USA from 27 January-01 February, 2018, organized by SPIE.

4. Received second best poster award for the paper entitled *"Development of a Scanning Optical Microscope with a Holographically Designed Illumination Beam"*, at the International Conference on Advances in Optics and Photonics (ICAOP-17), held on 23-26 November, 2017, organized by Guru Jambheshwar University of Science and Technology, Hisar (Haryana), India in association with OSI (Optical Society of India).

* * *